2000

SURFO Technical Report No. 99-4

SURFO

Papers from
the

SUMMER UNDERGRADUATE RESEARCH FELLOWSHIP PROGRAM IN OCEANOGRAPHY

at

THE UNIVERSITY OF RHODE ISLAND
Graduate School of Oceanography
and
Department of Ocean Engineering

NARRAGANSETT, RHODE ISLAND

June - August 2000

This program was funded by Grant OCE-9912236 from the National Science Foundation.

GSO Technical Report No. 99-4

PARTICIPANTS IN THE 2000 SUMMER UNDERGRADUATE RESEARCH FELLOWSHIP PROGRAM IN OCEANOGRAPHY

FELLOWS

Scott Armstrong	Texas A & M, College Station, TX
Amanda Baldauf	University of Rochester, Rochester, NY
Leah Bandstra	Beloit College, Beloit, WI
Teresa Dennison	Maine Maritime Academy, Castine, ME
Jason Jarrell	Marshall University, Huntington, WV
Jennifer Szlosek	Massachusetts Institute of Technology, Cambridge, MA
Casey Twanow	Illinois Wesleyan University, Bloomington, IL
Hillary Welch	University of Rhode Island, Kingston RI
Lauren Wilkinson	Brown University, Providence, RI

ADVISORS

Peter Cornillon
Margaret McManus Dekshenieks
Percy Donaghay
Brian Heikes
Dana Kester
John King
Elizabeth Lacey-Laliberte
Jim Miller
Brad Moran
Robert Pockalny
Tom Rossby
Barbara Sullivan-Watts
David Ullman

MENTORS

Paula Perez-Brunius
Clifford Heil
Roger Patrick Kelly
Kurt Rosenberger
Jim Sullivan
Julie Snow
Sarah Weinstein

PROGRAM ASSISTANTS

Diana Stram, Kim Carey & Rhonda Kenny

PREFACE

This report presents the papers written by the nine participants in the 2000 Summer Undergraduate Research Fellowships in Oceanography (SURFO) program at the Graduate School of Oceanography (GSO), University of Rhode Island (URI). This past summer represented the 15th year in which the program has been coordinated and extended through the several disciplines in oceanography and ocean engineering at URI's Narragansett Bay Campus.

The 2000 program was once again a strong success. During the fall of 1999 advertisements were sent to physics, chemistry, biology and geology departments, including faculty advisors at a number of minority colleges. Letters announcing the program were also sent to all Society of Physics Students, college advisors and to individual student members of ΣΠΣ Physics Honor Society. The SURFO web site was completely redesigned to include updated material and more useful links describing possible research programs at GSO/URI. We updated and improved our electronic on-line application form. We received 80+ applications for the program, and over half of these applicants used the new electronic application form. This trend of increasing electronic applications has continued since the SURFO web site was initially established in 1997. Nine students were selected for the program with a breakdown by oceanographic discipline as follows: 2 Geological, 2 Physical, 2 Chemical, 2 Biological, and 1 Ocean Engineering. Seven of the fellows who participated in the program were women.

The program started off with an orientation session and a tour of the GSO campus and facilities. For the 11 weeks of the summer program, each fellow worked on a research project under the supervision of a faculty mentor and a graduate student mentor. The range of research included: measuring acoustical properties of impregnated gill net material designed to reduce by-catch, mapping surface currents in the Mid-Atlantic Bight with a newly installed CODAR system, and measuring the particulate organic carbon flux contribution in the Arctic of a previously unused size fraction. The results of this latter project will be presented at the Winter ASLO meeting in February2001.

Fellows attended a total of 18 biweekly seminars (1-1.5 hour-long) during which faculty members and local environmental consultants gave informal presentations on a range of oceanographic disciplines. These presentations ranged from basic oceanographic topics to topics related to potential academic, governmental and industry-related career possibilities. We also offered lectures on scientific writing and how to create effective oral and poster presentations. Our exit questionnaires revealed that students found these seminars interesting and very useful, and the exposure to a wide range of disciplines/research topics helped students identify additional areas of interest. Other undergraduates (NOT affiliated with the SURFO program) working at EPA or NOAA labs on the Bay Campus and even graduate students at GSO also attend many of these seminars.

Finally, in addition to preparing their written reports, each SURFO gave a 30-minute presentation at the end of the program to summarize her/his results. Included in the summer events was our annual day of kayaking on the Narrow River, lead by Bob Sand, to investigate the flora and fauna of an estuary. A subset of SURFOs also participated in a series of field days funded by a Rhode Island Sea Grant study where water sampling, plankton tows, and ADCP current measurements were made at several locations in Narragansett Bay and Rhode Island Sound. We also continued with our second year of having an informal noon-time barbecue for the SURFOs on the veranda at the Horn Lab. This provided the SURFOs with a taste of graduate-student life in an informal setting where they were able to meet with GSO faculty, graduate students and staff.

One measure of success of our program is if fellows continue on with graduate studies in science and, specifically, in oceanography or ocean engineering. The exit questionnaire indicates that all 9 students plan to continue on with graduate studies in science/engineering. Of these, 6 will likely continue in oceanography. The participants in the 2000 SURFO program are grateful to the National Science Foundation for its support of the program through grant OCE-9912236. The SURFO participants and I would like to thank all of those individuals at URI who contributed to the program's success including those who advised the students and who gave SURFO seminar presentations. In addition, our thanks to Rhonda Kenny and Kim Carey for their assistance in the preparation of this report as well as the administrative, financial and recruitment tasks. Finally, we would like to thank Diana Stram who served as a coordinator for the program and made sure things ran smoothly, Bob Sand for running the kayak trip, and Paul Hall for coordinating the Friday barbecues.

Robert A. Pockalny
SURFO Site Director

TABLE OF CONTENTS

Page Number

Participants in the 2000 Fellowship Program i

Site Director's Preface ii

1. Surface Currents Over the Southern New England Shelf East of Long Island Sound Revealed by HF Radar 1
Scott Armstrong

2. In Search of the Source of Longshore Flow in Rhode Island Sound 15
Amanda Baldauf

3. Determination of Henry's Law Constants for Hydrogen Peroxide in Synthetic Seawater and Sodium Chloride Solutions of Varying Activities 37
Leah Bandstra

4. Distribution of Anthropogenic Contaminants in Sediments and Suspended Particles in Narragansett Bay, Rhode Island 51
Teresa Dennison

5. Current Switching Within a Rotating Framework: A Gulf Stream Simulation 81
Jason Jarrell

6. ^{234}Th-Derived Particle Organic Carbon Flux in the Labrador Sea: Significance of Carbon-Thorium Relationship with Size 91
Jennifer Szlosek

7. A Seasonal Invasion: Changing Population Dynamics of the Ctenophore *Mnemiopsis leidyi* in Narragansett Bay 115
Casey Twanow

8. The Effect of Barium Sulfate, Iron Oxide and Lead on Acoustic Reflectivity 129
Hillary Welch

9. Temporal Occurrence of Thin Phytoplankton Layers in Relation to Physical Processes 143
Lauren Wilkinson

Surface currents over the southern New England shelf east of Long Island Sound revealed by HF radar

Scott Armstrong

Graduate School of Oceanography

University of Rhode Island

Narragansett, RI

September 25, 2000

Abstract

Surface current patterns near Long Island Sound are studied by means of high-frequency (HF) radar from June 2, 2000 to July 31, 2000, in an area of high thermal front probability. Harmonic analysis is used to extract the tidal components of the flow, using the primary semidiurnal (M_2, S_2, N_2) and diurnal (K_1, O_1) constituents. M_2 is the dominant tidal constituent in the region, with maximum amplitudes of 70 cm s^{-1} near the mouth of Long Island Sound. The mean current flow over the two month period exhibits strong flow to the south and west of Block Island. Time series for wind and surface currents are passed through a low-pass filter and then correlated, with correlations showing significant influence of wind on residual surface current patterns.

1 Introduction

Ocean surface currents are influenced by a variety of forcing mechanisms such as tides, wind, and buoyancy flux. These currents are of great importance to the marine environment in many ways, particularly in the coastal zone. Currents are responsible for the dispersion of plankton, which reside in the upper portion of the water column and are the basis for all life in the earth's oceans. Knowledge and accurate prediction of surface currents could help contain potential disasters such as oil spills and the release of other floating pollutants, as well as aid ship navigation and search and rescue missions.

The problem of applying conventional measurement techniques to surface currents has proven to be formidable despite its great importance. It is extremely difficult to obtain reliable time-series data for surface currents using drifters since their movement on the surface is uncontrolled. Moored instruments and acoustic Doppler current profilers (ADCPs) cannot reliably measure currents closer than a few meters from the surface, which limits their usefulness. High-resolution current data over a large area is virtually impossible to obtain with any conventional method due to the high costs associated with the purchase and maintenance of large numbers of instruments. Thus a relatively inexpensive method for producing high-resolution time-series data of ocean surface currents over a large area is of great interest.

A technique for remotely sensing surface currents has been developed based on the resonant backscattering of high-frequency (HF) radio signals, first noticed by Crombie (1955). While it does not measure surface currents directly, the HF radar technique presents several advantages over conventional techniques used in coastal waters. Current vectors can be measured over several thousand square kilometers, to a resolution of 1 km, in real-time. Unfortunately, interference with the ionosphere acts to distort the backscattered signal and currently limits the practical range of the HF radar system to 100 km, restricting this technique to coastal waters.

The key concept behind HF radar systems is the Bragg scattering effect. Electromagnetic pulses are transmitted from shore in the HF part of the spectrum (3 to 30 MHz), corresponding to wavelengths similar to those of ocean waves. Two very large spectral peaks in the backscattered signal occur as a result of the transmitted signal reflecting off of Bragg waves, which in this case are ocean waves moving radially with respect to the receiving antenna with wavelength of exactly one-half the wavelength of the transmitted signal. The Doppler shift in the backscattered signal relative to the transmitted signal is due to the velocity of the surface waves moving directly toward or away from the receiving antenna (Stewart and Joy 1974). The velocity associated with this shift is the sum of the surface wave and the surface current velocities. The speed of deep water gravity waves relative to the water surface is known to be c, where $c^2 = g\lambda/2\pi$, g is the gravitational acceleration and λ is the wavelength. Thus the surface current's contribution to the Doppler shift can be determined. Since each station can only determine radial current velocities, multiple HF radar stations spaced 15-35 km apart are often made to broadcast across overlapping areas, thus extracting true current vectors.

There are currently at least two commercially available HF radar systems, the Coastal Ocean Dynamics Application Radar (CODAR) and the Ocean Surface Current Radar (OSCR). The two systems are very similar, differing significantly only in their method of direction finding. Direct comparisons of the two systems can be found in Fernandez and Paduan (1996).

The CODAR system has two antenna loops placed in orthogonal directions with a monopole running through the center. The ratio of signal strengths through the antenna loops is a known function of the angle of the source to the antenna. By comparing the measured signal strengths through the loops and statistically removing random noise by averaging over several minutes, this angle can be determined. The distance d of the Bragg waves to the CODAR station is a function of the time delay, ΔT, the time required

for the transmitted pulse to be backscattered to the receiving antenna. That is, $d = c\Delta T/2$ where c is the speed of light. Thus radial vectors from every location can be determined from a single spectrum, without the need for a beam-forming receiving antenna like the one employed by the OSCR system (Lipa and Barrick 1983).

Extensive validation tests on HF radar systems have been performed, with encouraging results (Barrick et al. 1977; Essen et al. 1981; Frisch and Weber 1980; Prandle 1991). More recent tests comparing HF radar to current meters and ADCPs have shown rms differences of 9-16 cm s^{-1} and mean differences of 2-4 cm s^{-1} (Shay et al. 1995; Chapman et al. 1997; Graber et al. 1997). Chapman et al. (1997) concluded that HF radar errors were no larger than 7-8 cm s^{-1}, the remaining errors being attributed to errors in current meter and ADCP measurements and differences in methodology between HF radar and conventional systems.

In this study we have used three SeaSonde model CODAR systems to analyze the surface current structure of an approximately 60 km by 60 km area east of Long Island Sound, at a resolution of 1.5 km (Figure 1). We intended to identify the surface current structure in this area, with particular attention to the low-frequency residual current flow in an area of high thermal front probability, revealed by Ullman and Cornillon (1999). Correlations between low-frequency surface currents and low-frequency wind flow were also examined.

2 Observations

Continous measurements were made at the three sites indicated in Figure 1, from June 2 through July 31, 2000. Each CODAR station compiles radial data every 10 minutes, potentially from every grid point. Every hour, 7 radial files are merged into an hourly radial file by taking the median at each grid point. The hourly radials at each station are then combined, resulting in hourly total vector files. While there was missing data from each grid point

over the two-month period of observation, the return rate was generally very high (over 95 percent) for grid points near the center of the study area, dropping off to 10 percent near the edges. The mean return rate over all the grid points was 71 percent. Along the axis connecting the Montauk Point and Misquamicut stations, no data was recorded since the radials could not be combined to give a true current vector because radial vectors obtained there are colinear. The wind data used in this paper was measured by the National Oceanic and Atmospheric Administration (NOAA).

3 Tidal Analysis

Tidal analysis was performed separately for each CODAR grid point. The M_2, S_2, N_2, K_1 and O_1 tidal constituents were extracted by harmonic analysis, similar to the method discussed in Emery and Thompson (1997). Higher

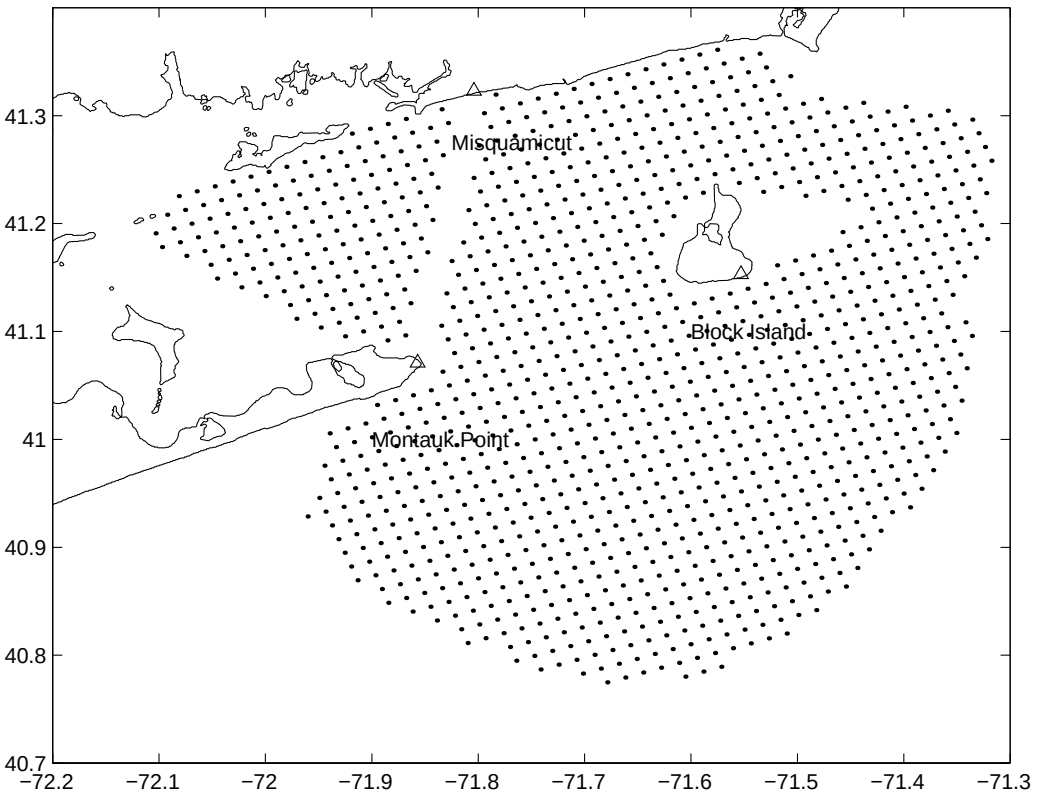

Figure 1: Map showing the location of the CODAR gridpoints. The triangles denote the CODAR stations.

harmonics (M_4, MS_4 and M_6) were not taken into account due to their small amplitudes and the relatively small data set with which to distinguish them.

3.1 Semidiurnal Constituents: M_2, S_2, and N_2

M_2 was the dominant tidal constituent, having particularly large amplitudes for grid points at the mouth of Long Island Sound, and between the Montauk Point and Block Island stations. The M_2 tidal ellipse properties vary smoothly over the water surface, as can be seen in Figure 2. Amplitudes for M_2 range from 5 cm s^{-1} south of Block Island to 70 cm s^{-1} in Long Island Sound. The mean amplitude for the M_2 component (averaged over all the

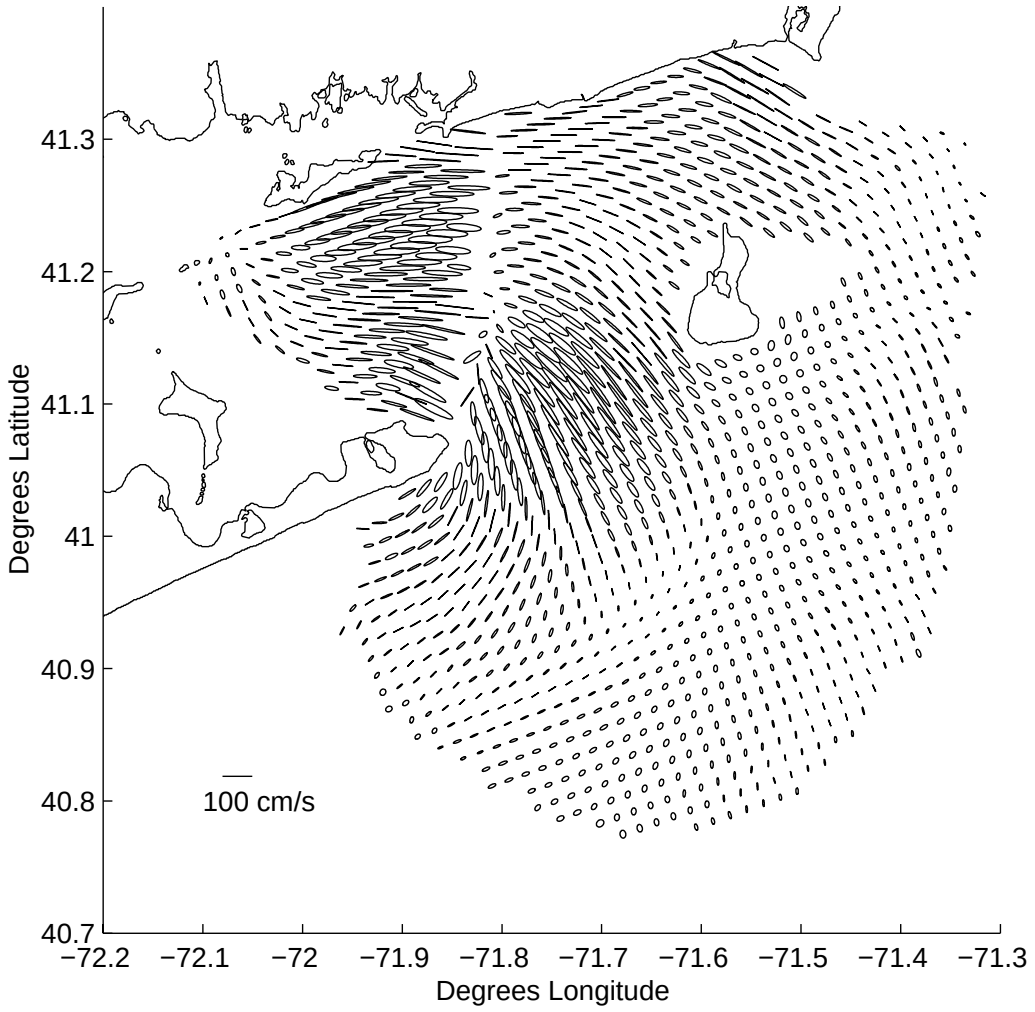

Figure 2: M_2 Tidal Ellipses

gridpoints) was 24.7 cm s^{-1}. S_2 (Figure 3) and N_2 (not shown) have similar spacial variablility as that of M_2, with much smaller amplitudes. The amplitudes for S_2 typically fell in the range of 1 to 11 cm s^{-1}, and for N_2 they ranged from 1 to 19 cm s^{-1}, with a mean of 6.67 cm s^{-1}. The suprisingly small amplitude for S_2 suggests that the two month time period was not sufficient for disguishing S_2 from the other two semidiurnal constituents.

3.2 Diurnal Constituents: K_1 and O_1

The diurnal tidal constituents were significantly smaller than the semidiurnal constituents. K_1 was the most significant diurnal constituent, with a mean

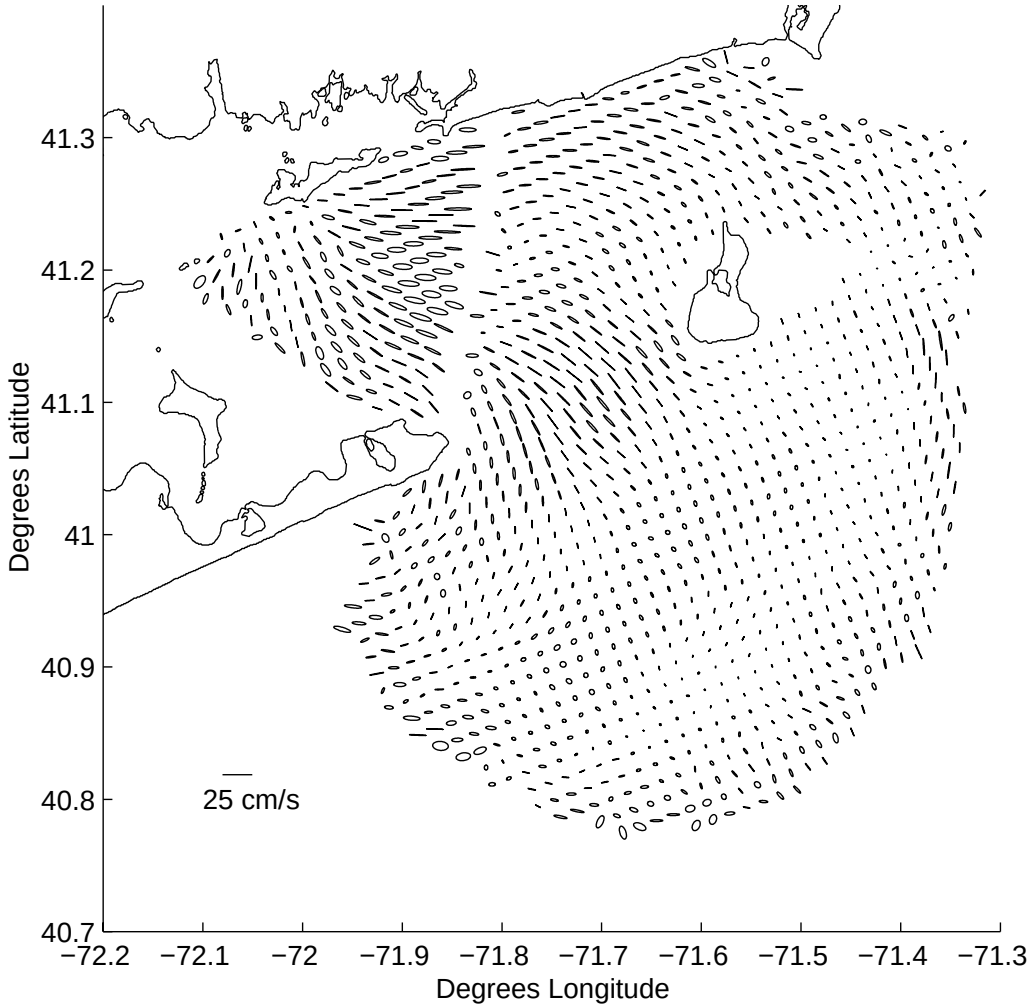

Figure 3: S_2 Tidal Ellipses

amplitude of 7 cm s^{-1} averaged across all the grid points. It ranged from 1 cm s^{-1} to 14 cm s^{-1}, reaching a maximum southwest of Block Island (Figure 4). Amplitudes for O_1 were very small, falling from 1 to 10 cm s^{-1} with a mean of 3 cm s^{-1}.

4 Low-Frequency and Mean Flow

Figure 5 shows the average current flow for the two month period. Several features become immediately apparent, including a fairly strong flow out of Long Island Sound, and a strong flow along a region to the southwest of Block Island.

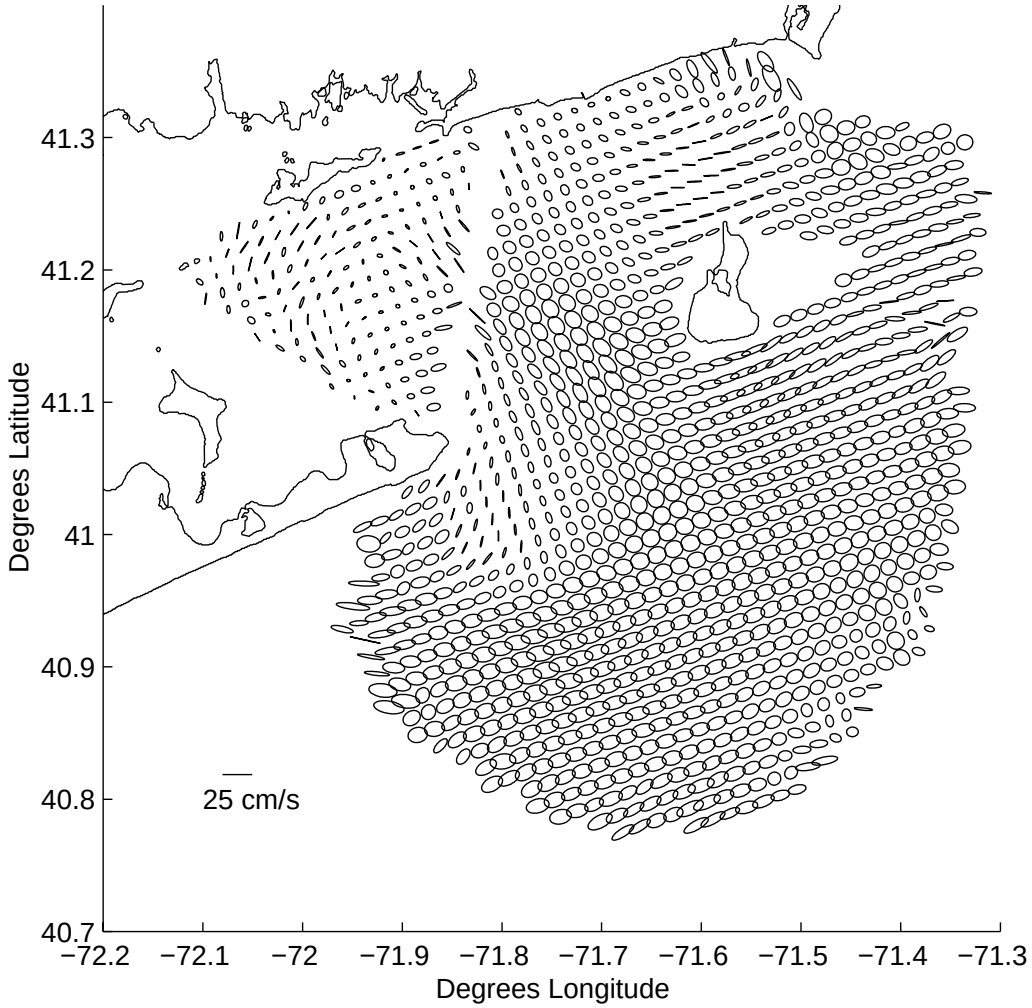

Figure 4: K_1 Tidal Ellipses

The surface current time series data was passed through a 36-hour low-pass filter, and the strength of the residual signal was correlated to areas of high temperature gradients, or thermal fronts, detected by satellite (Ullman and Cornillon 1999). While no statistically significant correlation was found, there were several occurrences of strong low-frequency current flow that seemed to flow along thermal fronts (see Figure 6).

Upon inspection of the low-pass filtered current data, it became apparent that the flow exhibited surprisingly high variation on the scale of several days. To find the source of the variation, the surface current data was compared

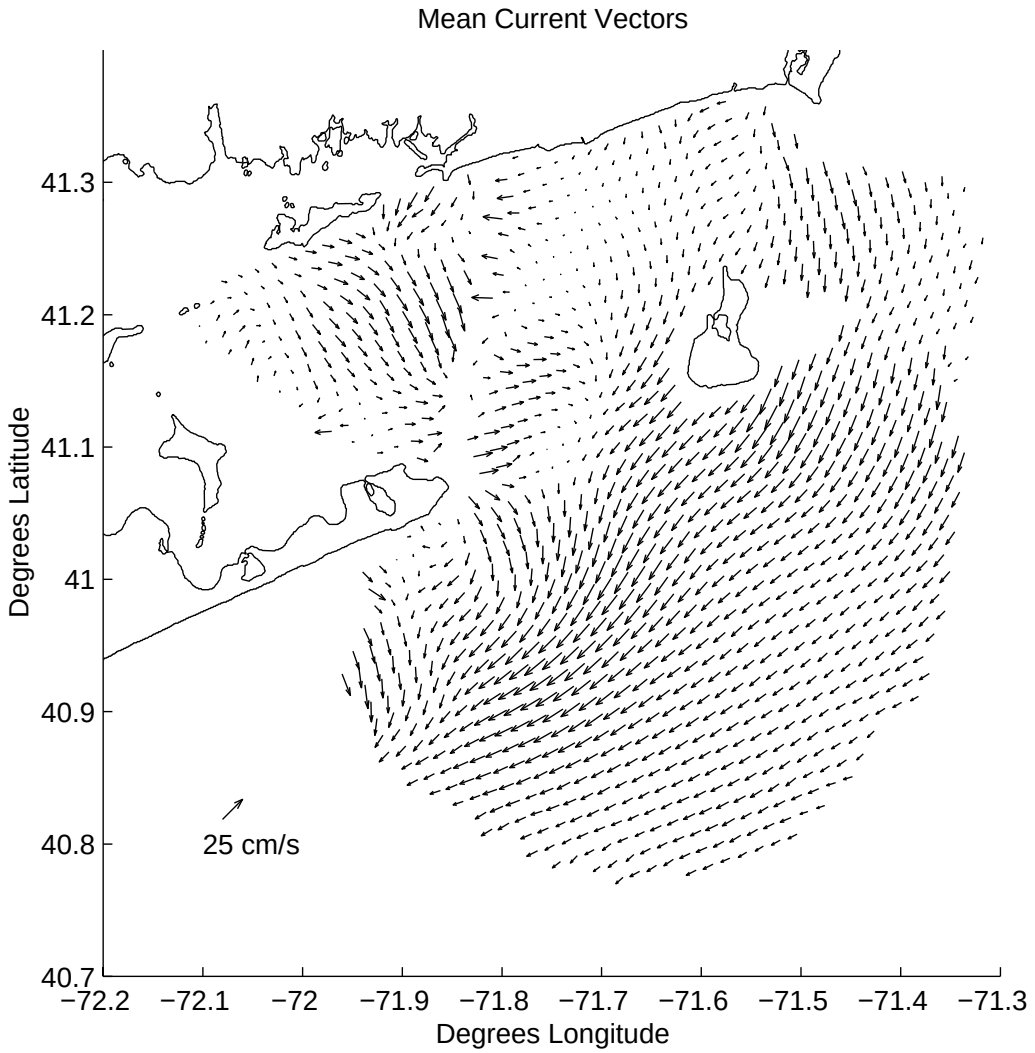

Figure 5: Mean Surface Current Flow

to wind data measured at the same time as the CODAR observations, which demonstrated a surprisingly good correlation between the data sets.

The wind data used in the comparison was measured hourly at Montauk Point by the National Oceanic and Atmospheric Administration (NOAA), over the same time period and to an accuracy of approximately 0.5 m/ s in speed and 10^o in direction. Typical wind speeds over the two month observational period were normally mild, ranging from 1 to 5 m/ s. The

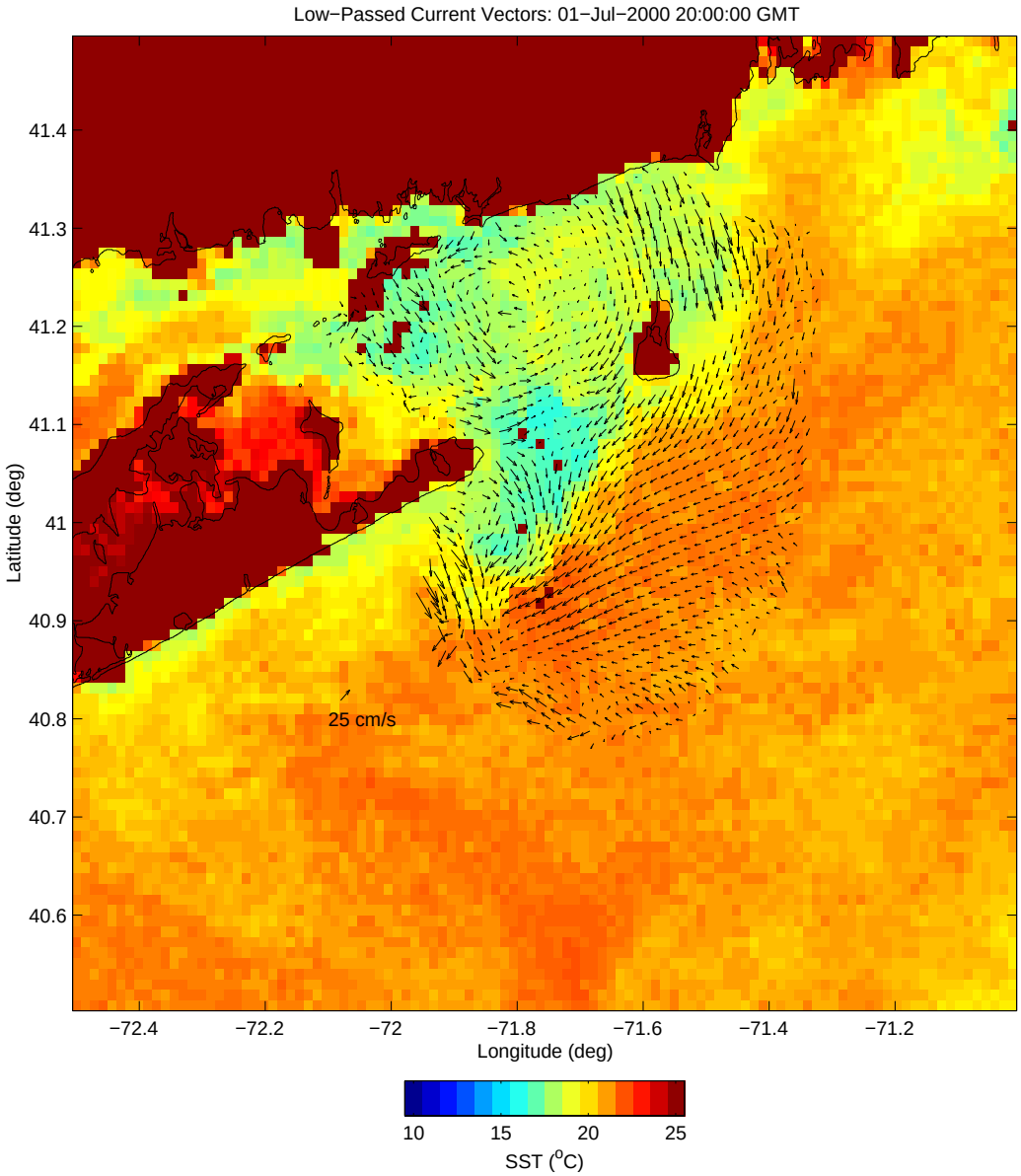

Figure 6: An SST Image with Low-Passed Current Vectors

wind time series data was low-pass filtered by the same method that was used to filter the current data.

To statistically measure the relationship between the wind (u_w, v_w) and current (u_c, v_c) vector times series, the method of complex correlation coefficients was used. The complex correlation coefficient γ and phase coefficient ϕ are given by

$$\gamma = \frac{< u_w u_c + v_w v_c > + i < u_w v_c + v_w u_c >}{< u_w^2 + v_w^2 >^{\frac{1}{2}} + < u_c^2 + v_c^2 >^{\frac{1}{2}}} \tag{1}$$

and

$$\phi = \arctan(\frac{< u_w v_c + v_w u_c >}{< u_w u_s + v_w v_s >}), \tag{2}$$

where the angle brackets denote an average over time (Shay et al. 1995). We can think of the phase angle as representing a counterclockwise rotation of the wind vector with respect to the current vector. The magnitude $|\gamma|$ of the complex correlation coefficient is the strength of the correlation between the wind and the current data.

The wind data from Montauk Point was correlated with every CODAR gridpoint individually, with $|\gamma|$ normally ranging from 0.4 to 0.7. The phase angle of the correlation was typically small but varied widely among values of $|\gamma|$ close to 0. For greater values of $|\gamma|$ the phase angle ϕ was normally slightly positive, typically 20^o, which suggests that Ekman veering may be responsible for this effect.

5 Summary

The CODAR system was used to study surface current patterns in an area of high thermal front probability, near the eastern boundary of Long Island Sound. While no correlation between current flow and the presence of thermal fronts was demonstrated, the high resolution of the CODAR system allowed many interesting features of the surface current structure to be revealed. The primary tidal influences on the surface current patterns were identified. The dominant tidal constituent, M_2, has large amplitudes near the

mouth of Long Island Sound, which has the effect of mixing large amounts of salt and freshwater. The tidal analysis revealed a significant domination of the high-frequency surface current patterns by tidal influences.

Low-passed residual current flow was compared to wind data to determine to what extent the weather conditions affected the surface current flow. High correlations between the wind and current data, along with the rather rough accuracy of both data sets, suggests that the non-tidal surface current flow is primarily influenced by wind conditions. Even stronger correlations should be expected if a more accurately measured wind data set could be obtained.

Although the observational period of this experiment was relatively short (2 months), the high resolution and near continuity of the CODAR measurements yielded unique insights on the current structure of the study area. Observations over a longer time or a broader area could provide even more exciting results.

References

Barrick, D., M. Evans, and B. Weber (1977). Ocean surface currents mapped by radar. *Science 198*, 138–144.

Chapman, R., L. Shay, H. Graber, J. Edson, A. Karachintsev, C. Trump, and D. Ross (1997). On the accuracy of HF radar surface current measurements: Intercomparisons with ship-based sensors. *J. Geophys. Res. 102*, 18737–18748.

Crombie, D. (1955). Doppler spectrum of sea echo at 13.56 Mc./s. *Nature 175*, 681–682.

Emery, W. J. and R. E. Thompson (1997). *Atmosphere-Ocean Dynamics*. New York: Pergamon.

Essen, H. H., E. Mittelstaedt, and F. Schirmer (1981). On near-shore surface current measurements by means of radar. *Dtsch. Hydrogr. Z. 34(1)*, 1–14.

Fernandez, D. and J. Paduan (1996). Simultaneous CODAR and OSCR measurements of ocean surface currents in monterey bay. In *IEEE International Geoscience and Remote Sensing Symposium*, pp. 1749–1752. Piscataway, N.J.: IEEE Press.

Frisch, A. and B. Weber (1980). A new technique for measuring tidal currents by using a two-site HF Doppler radar system. *J. Geophys. Res. 85*, 485–493.

Graber, H., B. Haus, L. Shay, and R. Chapman (1997). HF radar comparisons with moored estimates of current speed and direction: Expected differences and implications. *J. Geophys. Res. 102*, 18749–18766.

Lipa, B. and D. Barrick (1983). Least-squares method for the extraction of surface currents from CODAR crossed-loop data: Application at ARSLOE. *IEEE J. Oceanic Eng. OE 8*, 226–253.

Prandle, D. (1991). A new view of near-shore dynamics based on observations from HF radar. *Prog. Oceanogr. 27*, 403–438.

Shay, L., H. Graber, D. Ross, and R. Chapman (1995). Mesoscale ocean surface current structure detected by high-frequency radar. *J. Atmos. Oceanic Technol. 12*, 881–900.

Stewart, R. and J. Joy (1974). HF radio measurements of surface currents. *Deep-Sea Res. 21*, 1039–1049.

Ullman, D. and P. Cornillon (1999). Satellite-derived sea surface temperature fronts on the continental shelf off the northeast U.S. coast. *J. Geophys. Res. 104*, 23459–23478.

In Search of the Source of Longshore Flow in Rhode Island Sound

Amanda C. Baldauf
University of Rochester

Prepared for:
The Summer Undergraduate Research Fellowship in Oceanography

Advisor:
Dr. Robert A. Pockalny

Graduate School of Oceanography
University of Rhode Island

August 2000

Abstract

Recent hydrographic studies in Rhode Island Sound have identified a significant longshore current flowing from east to west across the mouth of Narragansett Bay. This longshore flow is characterized by very strong flow during the spring and summer months and by much weaker flow during the winter months. The source of this change in flow pattern is not well constrained, but some models have been proposed, including strong E-W flow of freshwater from Buzzards Bay, wind setup in summer, and the intensification of a cyclonic eddy near the entrance to Narragansett Bay.

Circulation, environmental, and tidal data have been compiled to determine the source of the longshore flow in Rhode Island Sound and test the various proposed models. ADCP data from 14 different cruises from the *RV ENDEAVOR* and analyzed using CODAS software. Wind, density stratification, external flow and bathymetry were identified to have some possible effect on the circulation pattern. Freshwater plumes and seasonal tidal differences were rejected as the source of the longshore flow. The locations for tidal wave phase changes were discovered and are probably caused by seafloor basins in Rhode Island Sound.

Introduction

Thesis

High-resolution circulation studies at the mouth of Narragansett Bay have identified a strong east-to-west longshore flow that begins somewhere east of Brenton Reef and extends well past Narragansett Beach. According to data from SeaGrant studies (Kincaid et al, in progress), this flow is significantly stronger in the summer months than in the winter months. Typically flows of this nature are associated with freshwater plumes and longshore jets, however, these characteristics are not seen in Rhode Island Sound. This paper explores some other possible explanations for the cause of this flow pattern.

Regional Setting

Rhode Island Sound is a large, shallow body of water, surrounded by Narragansett Bay to the north, Buzzards Bay and Vineyard Sound to the east, the Atlantic Ocean to the south, and Block Island Sound to the west. Bathymetry of Rhode Island Sound (Figure 1) is characterized by three main basins with a maximum depth ranging from 30-50 meters. One basin is located immediately south of Narragansett Bay. Two more are located further offshore near Block Island and Martha's Vineyard. The southern terminus of Rhode Island Sound is identified by a shallow region associated with a glacial terminal moraine. Two deep (>50 m) channels cut through this moraine onto the continental shelf.

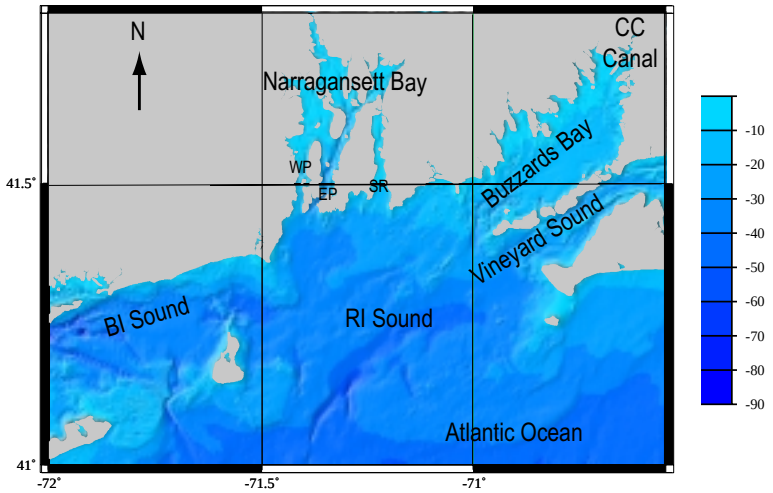

Figure 1: Bathymetry of Rhode Island Sound

Previous Work

A general northeast-southwest flow in Rhode Island Sound was first documented by Shonting (1969) and indicated that the surface layer (<15 m) was characterized by strong (~25 cm/s) flow to the southwest. The deeper regions were characterized by much slower (< 5 cm/s), more diffuse, cyclonic rotary flow.

A numerical model of tidal circulation in Rhode Island Sound has been developed using data from the tide gaging stations in the region (Spaulding and Gordon, 1982). This model suggests relatively weak tidal flux within Rhode Island Sound, however, bordering regions (i.e. Long Island Sound, Buzzards Bay, and Vineyard Sound) exhibit much greater tide-related flows during certain phases of the tide. Other models have suggested that tides enter Rhode Island Sound as a standing wave, but at some point become a progressive wave. This affects the time at which certain aspects of the tidal cycle reached any area of the Sound.

Recent high-resolution circulation studies at the entrance of Narragansett Bay (Kincaid et al, in progress) have observed a strong east-west longshore flow in the region during the spring and summer months (Figure 2). Hydrographic studies of the water column do not suggest a freshwater source for this longshore flow. During the winter months, the longshore flow is only observed near Narragansett Beach and the volume is proportional to the outflow from Narragansett Bay.

Important Forcing Factors

There are several environmental factors that influence the flow patterns observed in Rhode Island Sound. These factors include wind, precipitation and runoff, temperature, tides, and topography.

Wind and Ekman Effect. Surface water is strongly influenced by wind. The speed of surface currents induced by the wind is ~3% of the natural wind velocity (Knauss, 1978) and follows at roughly an 8 hour lapse. Deeper water (i.e. greater than 10 m), while influenced partially by surface wind currents, is dominated by more tidally induced flow patterns.

A well-defined seasonal difference in the wind patterns is observed in the Rhode Island Sound region. During the winter months, the wind comes from the northwest; during the summer months, the wind comes from the southwest. One would expect that with this pattern, flow out of Rhode Island Sound would be stronger during the winter, as the wind is pushing the water in a southern direction. However, this is not what is observed. Ekman circulation must be accounted for when considering the effects of wind on water.

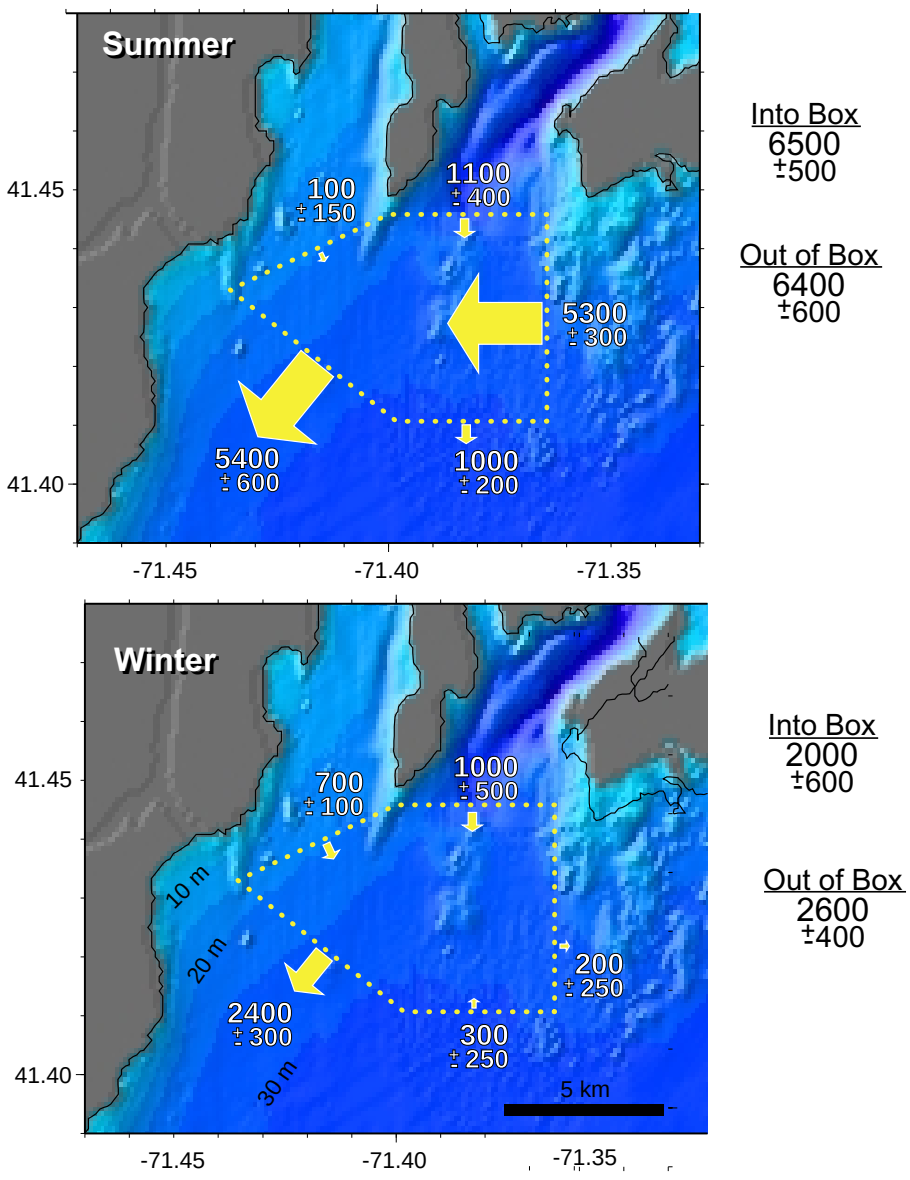

Figure 2: Seasonal longshore flow in Rhode Island Sound (Kincaid et al, in preparation)

Ekman circulation states that because of the Coriolis effect, each layer of water will have an effect on the water beneath it, causing each layer to turn 45 degrees to the right (in the Northern Hemisphere). The net effect is surface water flowing 45 degrees to the right of the wind direction. The net transport of water is 90 degrees to the right. Therefore, in Rhode Island Sound (Figure 3), during the winter, a northwest wind will cause surface water to flow to the south and during the summer, a southwest wind will cause water to flow toward the east.

According to the circulation studies at the mouth of Narragansett Bay (Kincaid et al, in preparation), the flow pattern past the mouth of Narragansett Bay is stronger during the summer than during the winter. The seasonal wind pattern offers a possible explanation. With the wind blowing from the southwest in the summer, Ekman circulation would cause the surface water to flow east. This could cause a pile-up of water in the eastern section of Rhode Island Sound and Buzzards Bay. Piling-up could cause a setup of water

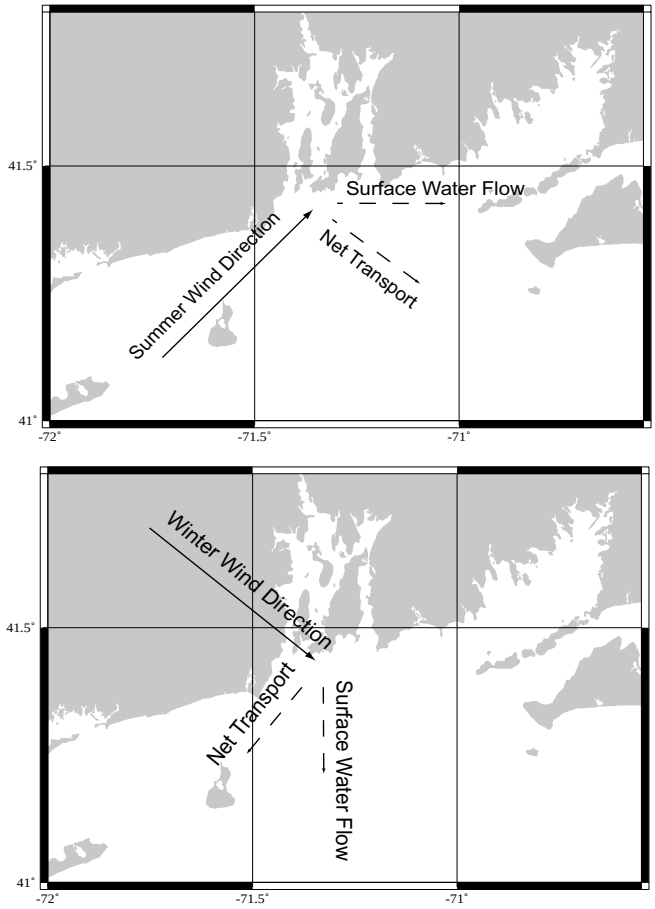

Figure 3: Ekman effect on wind in Rhode Island Sound

in Buzzards Bay, which would need to flow out along the northern edge of Buzzards Bay. The Coriolis effect would push water around to the right, and Kelvin waves would form as the water "bounced" along the shore.

Temperature stratification. During the winter months, Rhode Island Sound exhibits almost no temperature or salinity stratification (Figure 4). The temperature warms in the spring, and the surface water increases in temperature. This causes a thermal stratification, with warmer, less dense water on top and colder, more dense water on the bottom.

Previous hydrographic measurements in Rhode Island Sound have characterized this stratification and report that the pycnoclines slope back towards the entrance of Narragansett Bay (Shonting and Cook, 1970). This orientation at the pycnocline could lead to geostrophic flow of the deep water to the northeast. Therefore, more water may be pushed into the northeastern part of Rhode Island Sound and into Buzzards Bay. As was seen with the wind example, when more water is thrust into Buzzards Bay, it must flow out the north side of Buzzards Bay. This would cause the increase in flow seen in Rhode Island Sound.

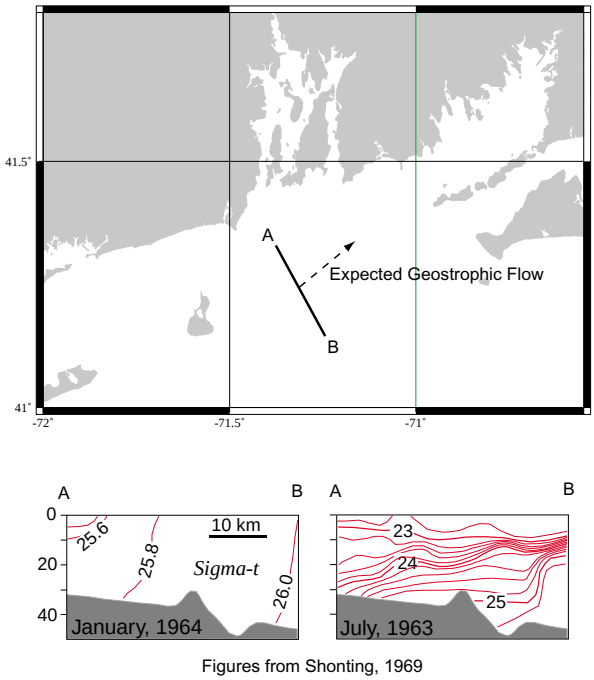

Figure 4: Density stratification

Freshwater input. During the winter months, a portion of the precipitation that falls to the surface in the region is frozen and stored as snow or ice within the watershed. As the air temperature heats up in the spring, the snow and ice melt, and a surge of freshwater from land flows into Narragansett Bay. Narragansett Bay has a 4708 km^2 drainage area (Pilson, 1985), and is the main source of freshwater for Rhode Island Sound. During the spring months, an increase in freshwater flow is observed in the western passage of Narragansett Bay. In some locales, a large flux of freshwater can lead to coastal jets that are similar to the longshore flow seen in Narragansett Bay (Kincaid et al, in progress). This may account for the longshore seen at Narragansett Beach, but no similar "upstream" freshwater source is present to explain the longshore flow generally observed during the spring and summer months.

As the freshwater input into Rhode Island Sound increases, a salinity stratification is observed. As with the thermal stratification, an inclined pycnocline will lead to geostrophic flow and cause a deep influx of more dense water into the northeast reaches of Rhode Island Sound and Buzzards Bay. This may happen in Rhode Island Sound and Buzzards Bay, and could be a precursor to the stronger summer thermal stratification.

Tides. Rhode Island Sound is characterized by a semidiurnal tide with a range of ~4 feet. Every day there are two high tides and two low tides, however these heights can differ greatly from each other, from day-to-day and week-to-week. Fortnightly there is a great change in tidal amplitudes, called spring and neap tides. The effects of the tide on water circulation patterns is unknown and needs to be further studied.

Bathymetry. The bathymetry of the ocean floor can have a great impact on the circulation in Rhode Island Sound. Water is greatly affected by constriction and friction. Constriction causes water to move faster through smaller spaces and friction opposes that motion by slowing the water down. These two forces counteract each other.

There are sections of seafloor in the Rhode Island Sound area that could cause any number of changes in flow. For instance, there is a deep channel that runs through Vineyard Sound, to the east of Rhode Island Sound. This water comes through at a high velocity, and could have an impact on the flow patterns of Rhode Island Sound.

Additionally, flow around the southern portion of Martha's Vineyard is quite strong. This could cause a change in flow, however, only if there was a change in flow outside of the Rhode Island Sound "box."

Another possibility is that the Cape Cod Canal increases its flow through Buzzards Bay during the summer months. Unfortunately, very little is known about this flow.

Remaining Viable Theories. Several working models have been described to explain possible seasonal flow patterns in Rhode Island Sound. Many have been discounted through the course of this introduction. Therefore, the researcher thought it necessary to review which theories remained viable. These theories include seasonal wind fluctuations, temperature and salinity stratification, and any type of excess flow from outside the Rhode Island Sound "box."

Data and Methods

In order to determine the seasonal flow patterns of Rhode Island Sound, several means and methods were utilized. Acoustic Doppler surveys of deep water areas are very effective in determining flow. Public domain software was used to analyze the velocities recorded by the ADCP. Each data set was broken down into its tidal component and comparisons to wind and tidal data identified any analogous patterns within the data sets.

Acoustic Doppler Current Profilers (ADCP) are effective means for studying the circulation patterns. The ADCP collects water velocity data by emitting a ping that is reflected off particles in the water column and listens for their echo. The difference between the outgoing and received waveform is determined and a corresponding phase shift or Doppler shift is determined. This Doppler shift is measured in three orthogonal directions to determine the horizontal and vertical velocity of a depth-specified water parcel. The assumption is made that free floaters in the water move at the same velocity as the water itself. Therefore, many layers of water are discernable, as their velocities could be different from water above or below them.

Early ADCP research focused on bottom-mounted equipment (Munchow et al, 1992; Sifling, 1997). This provided the researcher with multitudes of data on a single area of focus. More recent research has concentrated on ship-mounted equipment. This allows the researcher to study a more extensive area, with less precision and data for a single

area. The analysis of such data must correct for the velocity of the ship itself, as well as the ship's pitch and roll.

The Research Vessel ENDEAVOR is equipped with a 150-kHz narrowband Acoustic Doppler Current Profiler (ADCP). Since the home port for the RV ENDEAVOR is Narragansett, Rhode Island, ADCP data are routinely collected while transiting through Rhode Island Sound. Therefore, the ADCP data from the RV ENDEAVOR may be useful in determining flow patterns in Rhode Island Sound. It is very accurate for slow-moving water, and is especially accurate below ship velocities of 10 knots. The manufacturer has determined that the instrument loses accuracy as the speed of the vessel increases, especially for deeper depth bins.

ADCP data from the ENDEAVOR is accessible from two internet sources. The first source is the techserv website for the vessel (http://endata.gso.uri.edu). The data were downloaded in binary form, and "ascii-ed out" in order to be readable by LOGDAS (http://www.rdisntruments.com). The data were limited to the ensemble time, navigation information, depth profile, velocity average, and percent good. After the data were converted to ASCII, they were imported into Transect. Transect is a program that converts numerical current data into color-coded flow figures**.** It was apparent by viewing this output that the data was not calibrated correctly.

Original C-shell code was written to identify which cruises collected data from within Rhode Island Sound. By extracting the navigation information from the raw data, the data points could be overlaid onto a map of Rhode Island Sound and their relevance to the study determined. Computer algorithms were written to determine the direction and velocity of the water flow. However, while analyzing this data, it appeared that the ENDEAVOR ADCP had a noticeable starboard skew. All velocity vectors reported by the code showed the water flowing away from the vessel on the right side, no matter the position in the tidal cycle.

The University of Hawaii School of Ocean and Earth Science and Technology created a program called CODAS3 to calibrate narrow band ADCP data (http://moli.soest.hawaii.edu/software/codas3). It became apparent after using this program that the raw data from the techserv website may not have been calibrated correctly. Therefore, an additional source of raw data was necessary. The GLOBEC

website (http://www.oasd.bnl.gov/globec) archives previously-processed ENDEAVOR data with an approximate 10% error, which was permissible for this study.

After determining the accuracy of the data, the actual velocity of the ENDEAVOR was calculated. Within the raw data, the ship's position and time data were stored. By determining the time and spatial difference between two data points, a ship velocity could be determined. This velocity measurement was converted into knots.

It was necessary to determine the impact of the tidal cycle on the circulation patterns seen. Tidal information for Block Island was collected from a tide predictor site at the University of South Carolina (http://tbone.biol.sc.edu/tide). The tidal cycle was separated into four sections: slack low, flood, slack high, and ebb. Each section was roughly 3.1 hours long, as the usual M2 tidal cycle lasts 12.4 hours (Figure 5).

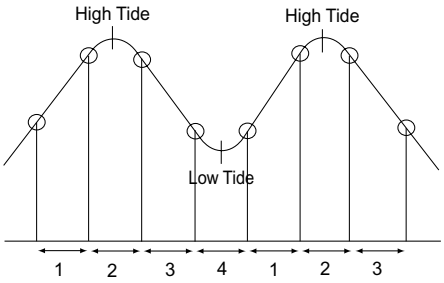

Figure 5: Tidal sections

Using a combination of CODAS3 and GMT scripts written by Dr. Robert Pockalny, magnitude vectors of water current were plotted on the Rhode Island Sound map. Each of these vectors was color coded, depending upon its point in the tidal cycle. Each section of the tidal cycle was plotted per season to determine any seasonal and tidal variability in Rhode Island Sound.

Daily average wind data was taken from two stationary buoys in Buzzards Bay, BUZM3 and 44028, from the website for the National Data Buoy Center (http://seaboard.ndbc.noaa.gov). A program was written to determine the direction and

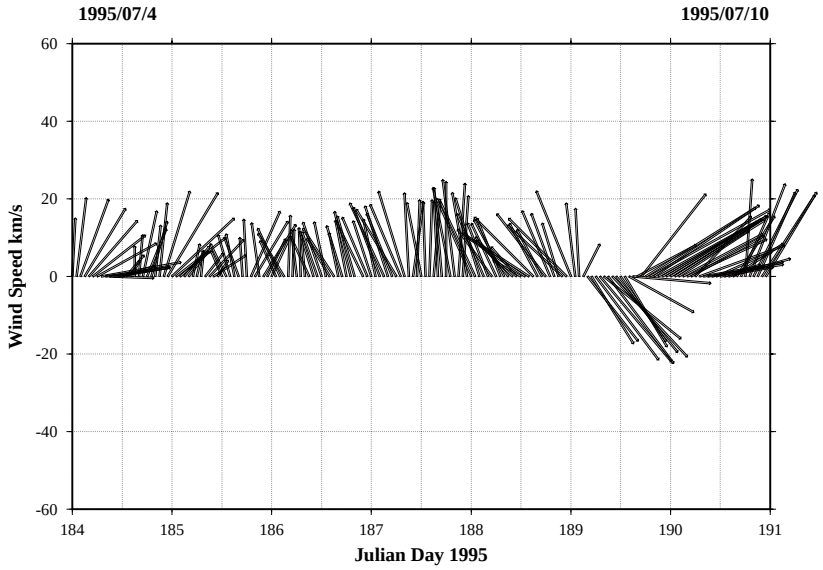

Figure 6: Example of wind plot

strength of the wind gusts for each day in the data set, as well as for a week beforehand (Figure 6). These wind data plots were compared to individual ADCP transects to identify strong correlation wind events.

Observations

The plots of current velocity vectors provided information for different directions and possible sources for the flow patterns observed in Rhode Island Sound. By separating the tidal cycle into four sections, differences were easier to identify. A slight velocity difference was observed in the slack high and slack low plots. A change in tidal flow pattern was observed, and is probably caused by the bathymetry of the area. strength of the wind gusts for each day in the data set, as well as for a week beforehand (Figure 6). These wind data plots were compared to individual ADCP transects to identify strong correlation wind events.

The primary objective of this study was to identify possible causes of the seasonal variations in flow observed at the entrance of Narragansett Bay (Kincaid et al, in progress). Within the ADCP data collected by the ENDEAVOR, there could be very few definitive variations noted because the seasonal flow patterns are quite similar, even

when compared by what section of the tidal cycle the data points appeared in. strength of the wind gusts for each day in the data set, as well as for a week beforehand (Figure 6). These wind data plots were compared to individual ADCP transects to identify strong correlation wind events.

In comparing the tidal cycle sections of the two different seasons (April through August was displayed as "summer" and September through March was displayed as "winter"), very few differences could be noted. Though the flow patterns shown in the winter ebb section (Figure 7) appear in a different area and are of a different magnitude than the summer ebb section, the difference appears to be caused by the bathymetry of Rhode Island Sound, not by an increase in flow. strength of the wind gusts for each day in the data set, as well as for a week beforehand (Figure 6). These wind data plots were compared to individual ADCP transects to identify strong correlation wind events.

The velocity vectors in the summer and winter sections of the slack low section of the tidal cycle (Figure 8) are at roughly the same latitude and longitude. Overall, the summer flow appears to be much stronger than the winter flow, although not nearly two times as fast. The cause of this flow difference could be any of the above-mentioned viable theories. There were no anomalous wind patterns on any of the days in the slack low section of the winter or summer and the tidal amplitudes appear normal. strength of the wind gusts for each day in the data set, as well as for a week beforehand (Figure 6). These wind data plots were compared to individual ADCP transects to identify strong correlation wind events.

The velocity vectors in the summer and winter sections of the flood section of the tidal cycle (Figure 9) are also along the same ship track. There is no discernable difference between the winter and summer flows. They appear to be in the same direction and of roughly the same magnitude for each day in the data set, as well as for a week beforehand (Figure 6). These wind data plots were compared to individual ADCP transects to identify strong correlation wind events.

The difference between the summer and winter slack high sections of the tidal cycle (Figure 10) shows some type of seasonal variation. Although the two tracks are in different locations in Rhode Island Sound, both transect the specific area of interest. The winter slack high section shows a very strong flow, directly northward. The summer

slack high section shows a general northward flow, with a strong westerly component nearer the mouth of Narragansett Bay. There were no anomalous wind or tidal amplitude events during the days in question. There is also possible evidence of a cyclonic flow, however this could not be confirmed. The cause of this flow pattern remains uncertain. strength of the wind gusts for each day in the data set, as well as for a week beforehand (Figure 6). These wind data plots were compared to individual ADCP transects to identify strong correlation wind events.

The cause of any variation seen in the data sets could not be determined unequivocally. Of the remaining viable theories, any could be the cause. Originally, the researchers thought that the tides in Rhode Island Sound were dominated by a standing wave, meaning that the period of fastest velocity would be during ebb and flood. However, upon looking at the ENDEAVOR data, it was determined that the periods of fastest water are during slack low and slack high, indicating that the tides in Rhode Island Sound are dominated by a progressive wave. This is the same conclusion reached by Spaulding & Gordon (1982). It is believed that the causes of this change are bathymetric in nature, as these wave phase changes are seen in the ADCP data from the RV ENDEAVOR. At the locations of the phase changes, prominent shoals are seen in the bathymetry of the Sound. strength of the wind gusts for each day in the data set, as well as for a week beforehand (Figure 6). These wind data plots were compared to individual ADCP transects to identify strong correlation wind events.

Information from Signell (1987) could have been useful for determining the seasonal flow patterns in Buzzards Bay, as a source for the flow patterns seen in Rhode Island Sound. However Signell's study includes only the winter months, and does not look into a seasonal flow patterns of the wind gusts for each day in the data set, as well as for a week beforehand (Figure 6). These wind data plots were compared to individual ADCP transects to identify strong correlation wind events.

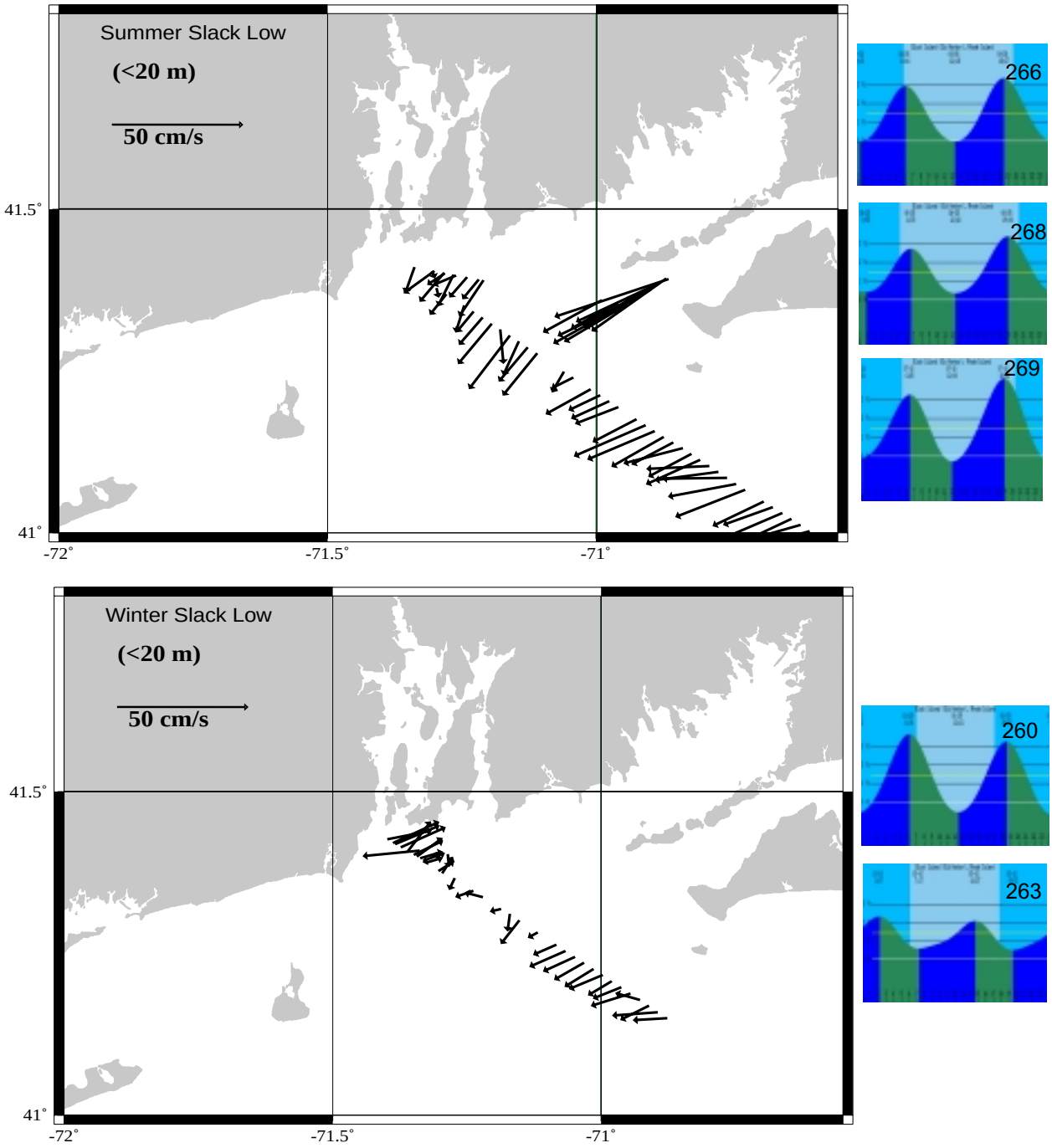

Figure 7: Comparison of seasonal slack low flow for Rhode Island Sound

The arrow vectors indicate the flow direction and speed at the time of ADCP data collection.

The small boxes to the right are the tidal amplitudes and times during the day of data collection.

Data points are from the middle of the slack low section of the tidal cycle.

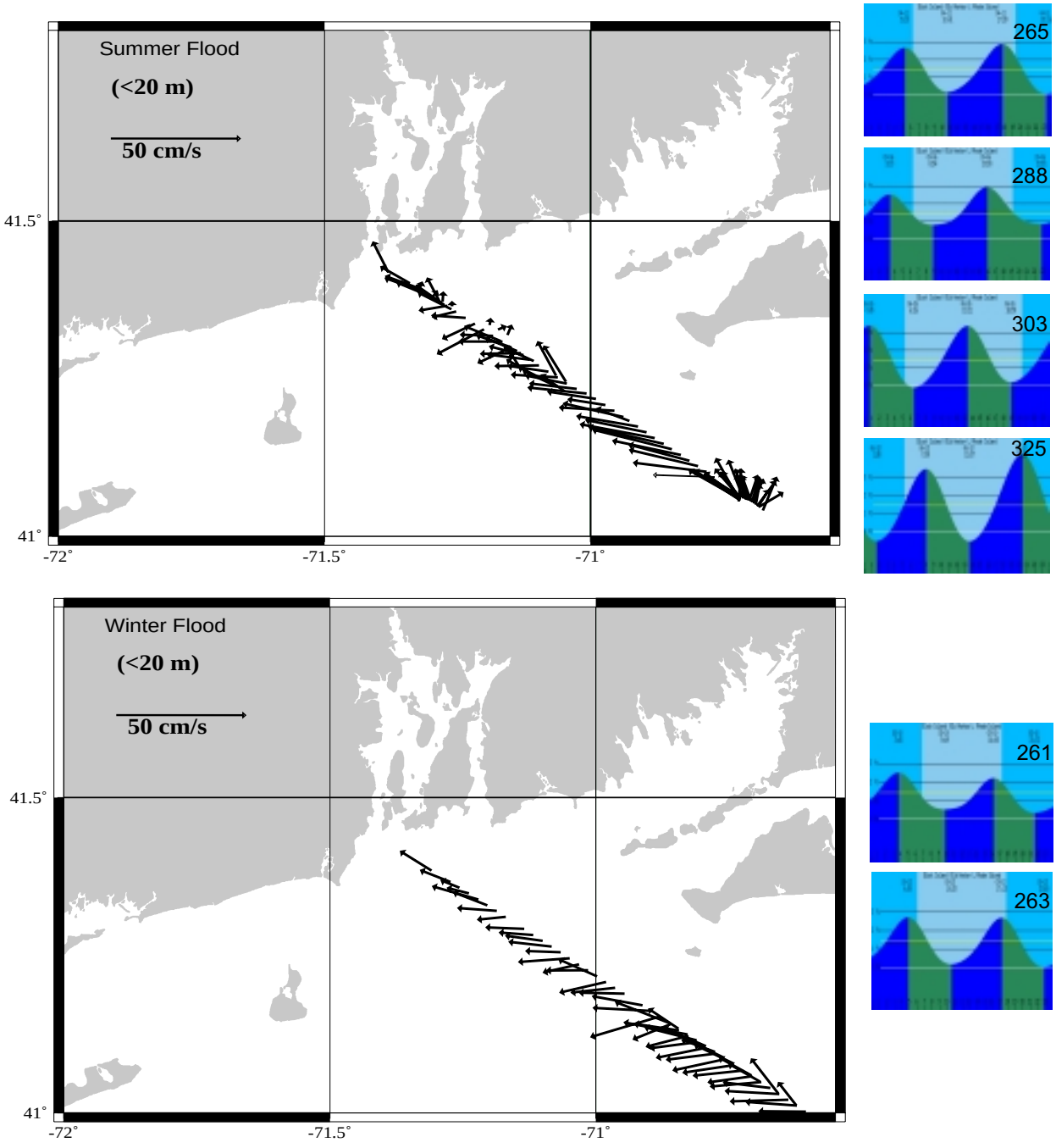

Figure 8: Comparison of seasonal flood flow in Rhode Island Sound.

The arrow vectors indicate the flow direction and speed at the time of ADCP data collection.

The small boxes to the right are the tidal amplitudes and times during the day of data collection.

Data points are from the middle of the flood section of the tidal cycle.

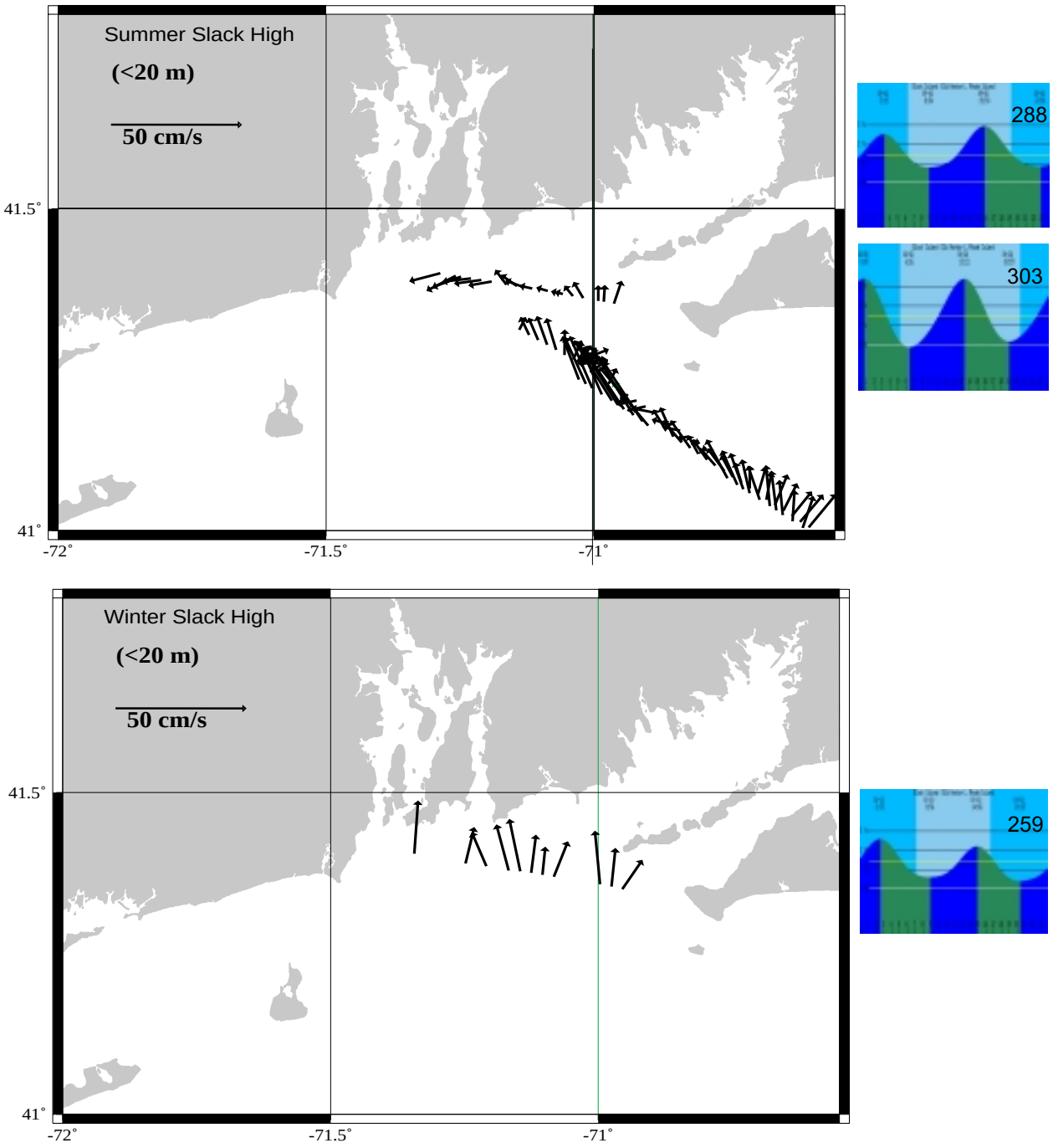

Figure 9: Comparison of seasonal slack high flow in Rhode Island Sound.
The arrow vectors indicate the flow direction and speed at the time of ADCP data collection.
The small boxes to the right are the tidal amplitudes and times during the day of data collection
Data points are from the middle of the slack high section of the tidal cycle..

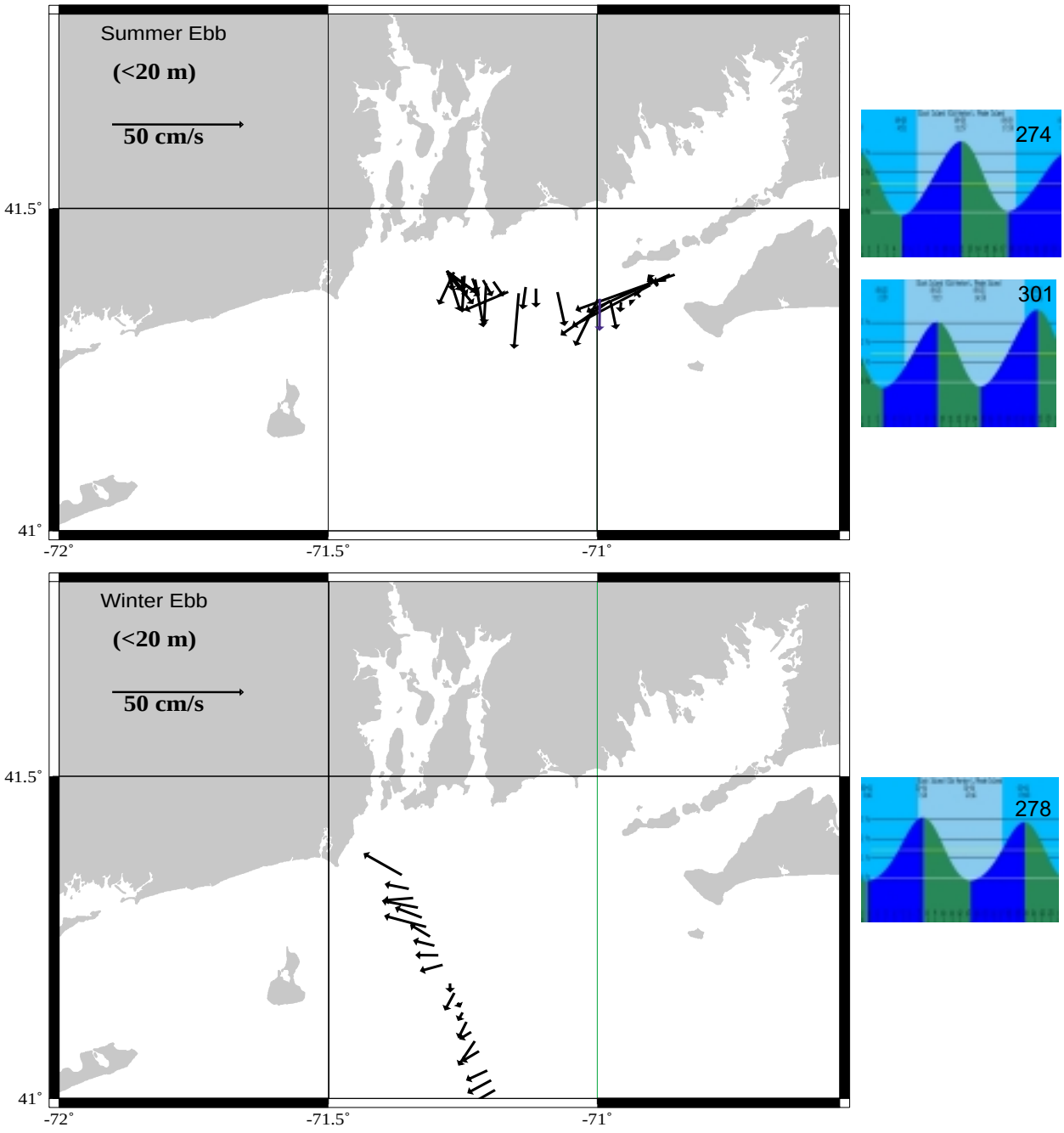

Figure 10: Comparison of seasonal ebb flow in Rhode Island Sound.

The arrow vectors indicate the flow direction and speed at the time of ADCP data collection.

The small boxes to the right are the tidal amplitudes and times during the day of data collection..

Data points are from the middle of the ebb section of the tidal cycle..

Conclusions

Though the cause of the seasonal longshore flow observed past Narragansett Bay is still unknown, some interesting points were raised with this study. There is a seasonal flow difference in a few sections of the tidal cycle. Also, the location of the tidal phase shift was noted, and the cause bathymetry of the area.

Future Work

There are several ways in which this project could be improved. The first suggestion is to mount several ADCPs at the bottom of Rhode Island Sound on the seafloor of the main areas in question. This would provide the researcher with a large amount of data at an important location, thereby eliminating the questions of data relevance and amount. The second suggestion is to have a longer time series in the data collection. The more lengthy the data set, the more information it contains, and the more useful it is to the researcher. The main problem with the data sets in this study is that the time that they cover is generally focused on one section of the tidal cycle. This gives the researcher a very limited window into the tidal cycle and its effects on the circulation patterns of Rhode Island Sound. The third suggestion is to use a higher frequency ADCP. The 150 kHz ADCP aboard the ENDEAVOR has very low resolution. If a higher frequency instrument were mounted on the vessel, more accurate data could be collected from the water column.

Additionally, a more in depth modeling study of the phase shift of the tidal wave in Rhode Island Sound from standing to progressive to standing wave could provide interesting information on the tides and their effects in those areas.

References

Chao, S. (1988). Wind-driven Motion of Estuarine Plumes, *Journal of Physical Oceanography*, 18, 1144-1166.

CODAS. University of Hawaii. http://www.soest.hawaii.edu

Garvine, R. W. (1995). A Dynamical System for Classifying Buoyant Coastal Waters, *Continental Shelf Research*, 15, 1585-1596.

Geyer, W. R., and R. Signell (1990). Measurements of Tidal Flow Around a Headland With a Shipboard Acoustic Doppler Current Profiler, *Journal of Geophysical Research*, 95, 3189-3197.

Hicks, S. D. (1963). Physical Oceanographic Studies of Narragansett Bay, *United States Fish and Wildlife Service Special Scientific Report – Fisheries No. 457*.

Kincaid, C. et al (in progress). SeaGrant study on hydrography of Rhode Island Sound.

Knauss, J. A. Introduction to Physical Oceanography. Prenctice-Hall. New Jersey, 1978.

Levine, E. R., and K. E. Kenyon (1975). The Tidal Energies of Narragansett Bay, *Journal of Geophysical Research*, 80, 1683-1688.

Munchow, A., R. W. Garvine, and T. F. Pfeiffer (1992). Subtidal Currents from a Shipboard Acoustic Doppler Current Profiler in Tidally Dominated Waters, *Continental Shelf Research*, 12, 499-515.

NATIONAL DATA BUOY CENTER. http://seaboard.ndbc.noaa.gov

Pilson, M. E. Q. (1985). On the Residence Time of Water in Narragansett Bay, *Estuaries*, 8, 2-14.

RDI (RD Instruments). Acoustic Doppler Current Profilers, Principles of Operation: A Practical Primer. RD Instruments, San Diego, CA, 1989.

RV ENDEAVOR ADCP INFORMATION. University of Rhode Island Graduate School of Oceanography. http://endata.gso.uri.edu

Shonting, D. H., G. S. Cook, and F. G. Wyatt, Jr. (1966). The Seasonal Distribution of Oceanographic Variables Measured in Rhode Island Sound During 1963-1964, *Naval Underwater Weapons Research and Engineering Station NUWS Consecutive No. 423*.

Shonting, D. H. (1969). Rhode Island Sound Square Kilometer Study 1967: Flow Patterns and Kinetic Energy Distribution, *Journal of Geophysical Research*, 74, 3386-3395.

Shonting, D. H. and G. S. Cook (1970). On the Seasonal Distribution of Temperature and Salinity in Rhode Island Sound, *Limnology and Oceanography*, 15, 100-112.

Sifling, J. P. (1997). Observational Experiments in Hydrodynamics of the Narrow River Estuary using an Acoustic Doppler Current Profiler. Masters thesis, University of Rhode Island, Graduate School of Oceanography, Narragansett, RI.

Signell, R. P. (1987). Tide- and Wind-Forced Currents in Buzzards Bay, Massachusetts. *WHOI Technical Report 87-15*.

Spaulding, M. L. and R. B. Gordon (1982). A Nested Numerical Tidal Model of the Southern New England Bight. *Ocean Engineering*, 9, 107-126.

Spaulding, M. L., and F. M. White (1990). Circulation Dynamics in Mt. Hope Bay and the Lower Taunton River, *Coastal and Estuarine Studies*, 38, 494-510.

TIDAL INFORMATION. University of South Caroline. http://tbone.biol.sc.edu/tides

Weisberg, R. H., and W. Sturges (1976). Velocity Observations in the West Passage of Narragansett Bay: A Partially Mixed Estuary, *Journal of Physical Oceanography*, 6, 345-354.

Determination of Henry's Law Constants for Hydrogen Peroxide in Synthetic Seawater and Sodium Chloride Solutions of Varying Activities

Leah M. Bandstra
Beloit College,
Beloit, Wisconsin

Prepared for:
The Summer Undergraduate Research Fellowship in Oceanography

Advisors:
Dr. Brian Heikes
Dr. Dana Kester

Graduate School of Oceanography
University of Rhode Island

August 2000

Abstract

Hydrogen peroxide (H_2O_2) plays a vital role in various atmospheric processes such as the formation of HO_x, a species that removes pollutants from the atmosphere. Near the sea surface, the concentration of hydrogen peroxide in the atmosphere drops dramatically. Some explanations for this phenomenon involve hydrogen peroxide dissolving at the sea surface or in seawater aerosols near the surface of the sea. To determine the feasibility of these theories, the Henry's law constant of hydrogen peroxide in seawater was determined at 18°C. The value determined was 1.2×10^5, higher than the value we determined for water, 9.9×10^4. The Henry's law constants were also determined to be 1.1×10^5 and 1.8×10^5 in 1 M NaCl and 3 M NaCl, respectively. These results lead to speculation that an association between hydrogen peroxide and the ions in solution might be a cause of the increased solubility.

Introduction

Hydrogen peroxide, H_2O_2, plays a vital role in various atmospheric processes. The reaction of hydrogen peroxide with light to form either HO or HO_2 radicals (known collectively as HO_x) is of particular interest in terms of atmospheric contaminants [*Logan et al.*, 1981]. HO_x reacts with a range of pollutants, removing them from the atmosphere. The concentration of these species, therefore, is directly related to the oxidizing capacity of the earth's atmosphere, the capacity of the atmosphere to clean itself.

As more pollutants are being added to the atmosphere every day, it becomes important to understand the dynamics of the HO_x system and to know what is controlling its concentration. Under certain conditions, HO_x radicals can react with each other to form hydrogen peroxide. In this way hydrogen peroxide acts as a reservoir species for HO_x, such that the dissociation of H_2O_2 produces HO_x and HO_2 + HO_2 makes H_2O_2. Hydrogen peroxide has become the focus of much research due to its involvement with the HO_x system.

It is expected that the concentration of hydrogen peroxide in the atmosphere would closely follow the concentration of water in the atmosphere due to a series of reactions in which hydrogen peroxide is formed from ozone and water. Figure 1 shows a profile of the increasing amount of water in the atmosphere from an altitude of 12 km down to sea

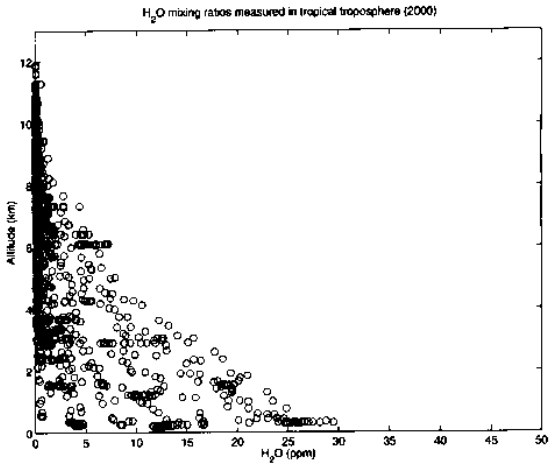

Figure 1: Profile of H_2O in the atmosphere from 12 km to sea level (data taken from NASA PEM-Tropics B Mission aboard DC8)

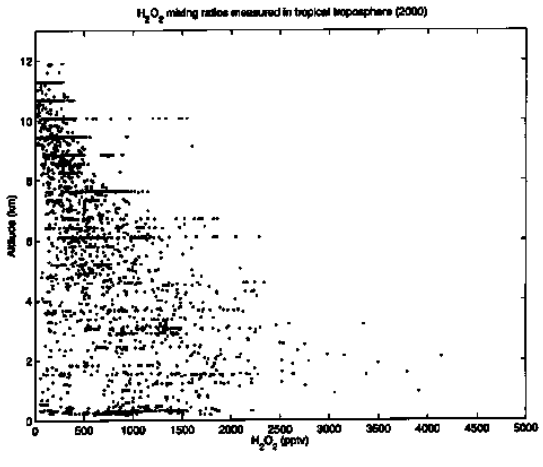

Figure 1: Profile of H_2O_2 in the atmosphere from 12 km to sealevel (data taken from NASA PEM-Tropics B Mission aboard DC8)

level. Similarly, Figure 2 shows the concentration of hydrogen peroxide in the atmosphere over the same altitude. At an altitude of approximately 1 km, the amount of hydrogen peroxide falls dramatically as sea level is approached. Several theories exist attempting to explain this occurrence.

Two of the major explanations for the drop in hydrogen peroxide concentration near the ocean surface involve hydrogen peroxide dissolving in seawater. One theory proposes the ocean itself as a sink for hydrogen peroxide, with hydrogen peroxide dissolving into the ocean at the air-sea interface. Another related possibility involves hydrogen peroxide dissolving in the seawater aerosol droplets suspended in the atmosphere near the surface of the sea. These aerosols contain dissolved sulfur dioxide, SO_2, from sea life and other processes occurring in the ocean. Hydrogen peroxide is known to oxidize sulfur dioxide, creating sulfuric acid, H_2SO_4 [*Calvert et al.,* 1985]. If hydrogen peroxide dissolves readily in these aerosols as well as at the surface of the sea, these processes could play a major role in explaining the drop in hydrogen peroxide concentration near the sea surface and have large implications on the sulfur chemistry in the boundary layer.

For dilute concentrations of a gas, its solubility in a given liquid is described by Henry's law. Henry's law states that the amount of a gas dissolved is directly proportional to the partial pressure of the gas, such as hydrogen peroxide, at equilibrium:

$$[H_2O_2]_{aq} = K_h P_{H_2O_2}$$

where $[H_2O_2]_{aq}$ is the known concentration of hydrogen peroxide in solution, $P_{H_2O_2}$ is the measured partial pressure of hydrogen peroxide in the air, and K_h is the Henry's law constant. Each gas has a characteristic Henry's law constant, which is a function of temperature and salinity. At higher temperatures, gases will evaporate, so less remains dissolved in the liquid. The major focus of the research presented here is the effect salinity has on the Henry's law constant of hydrogen peroxide.

Previously, the Henry's law constant of hydrogen peroxide in water has been determined and is well accepted (recently summarized in *O'Sullivan et al.* 1996). *Lind*

and Kok [1986] have also experimented with hydrogen peroxide in dilute sulfuric acid solutions and solutions of ammonium sulfate. It was found that the Henry's law constant decreased in the sulfuric acid solutions, but increased in the ammonium sulfate solutions. These results raise questions about associations between hydrogen peroxide and the ions in solution and the affects of pH on the solubility.

In this paper, we present our results for the Henry's law constant of hydrogen peroxide in a synthetic seawater solution, as well as results in both 1 M and 3 M sodium chloride solutions. Henry's law constant of hydrogen peroxide in water were also obtained as a verification of our method.

Experimental

Apparatus. Three major steps are involved in determining the Henry's law constant of hydrogen peroxide. First, equilibrium must be established between an aqueous solution of hydrogen peroxide and air. Second, the hydrogen peroxide must be removed from the gas phase and collected. Finally, the concentration of hydrogen peroxide in the collected sample must be analyzed.

Establishing Equilibrium: A system of continuous-flow glass scrubbing coils was used to establish an equilibrium between humidified zero air and a hydrogen peroxide standard, similar to those described in O'Sullivan et al, 1996 (Figure 3). To humidify the

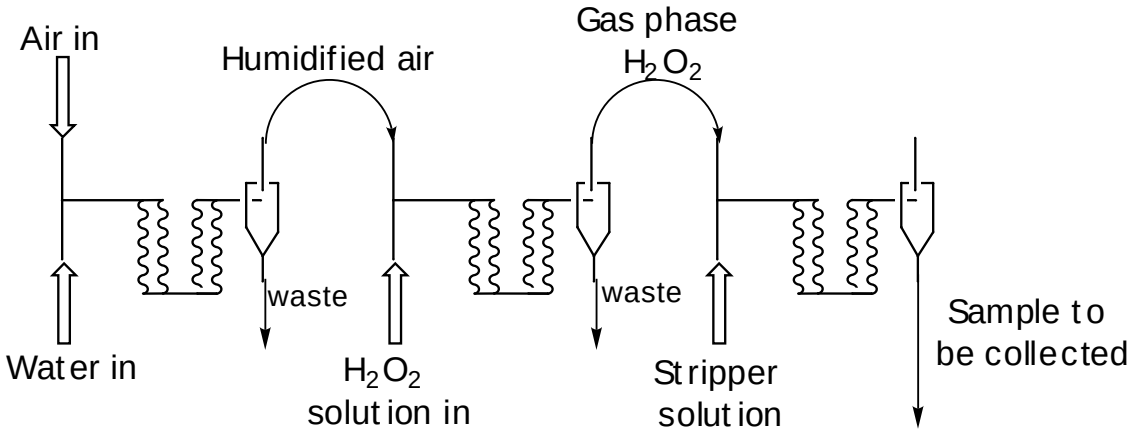

Figure 3: Schematic of continuous-flow glass scrubbing coils used to establish equilibrium and collect gas-phase hydrogen peroxide.

air, 18 MΩ Milli-Q water was pumped through a set of coils with zero air (Scott-Marrin, Inc.) at a rate of 3.24 x 10^{-4} standard liters per minute (determined by calibrating 3-stop tygon tubing) using a peristaltic pump (Ismatec). The zero air flow rate of 0.5 slpm was controlled with a mass flow controller (MKS Instrument Corp.). This humidified air was then pumped into a second set of coils with the aqueous hydrogen peroxide standard using a peristaltic pump (Ismatec). The gas phase hydrogen peroxide was then diluted with zero air at 1.5 slpm using a mass flow controller (MKS Instrument Corp.) before going to the collection coils. This dilution was performed so the gas would not condense upon transportation from the generation water bath to the collection water bath. Both sets of coils were submerged in a water bath and the temperature remained constant at 18°C for all experiments discussed.

Collection: In the collection coils, the diluted gas phase hydrogen peroxide was reacted with a stripper solution of pH 6 using potassium hydrogen phalate as a buffer to remove the hydrogen peroxide gas from the air. The stripper was pumped in at 3.24 x 10^{-4} slpm and the samples were pumped out at 3.24 x 10^{-4} slpm using a peristaltic pump (Ismatec). The collection coils were also submerged in a water bath with the temperature controlled at 18°C. The stripper solution with dissolved hydrogen peroxide was collected at 3.0 minute intervals for quantification by high performance liquid chromatography (HPLC).

Quantification: Hydrogen peroxide quantification was done using a method described by *Lee et al.* [1995] (Figure 4). Collected samples were injected into the HPLC

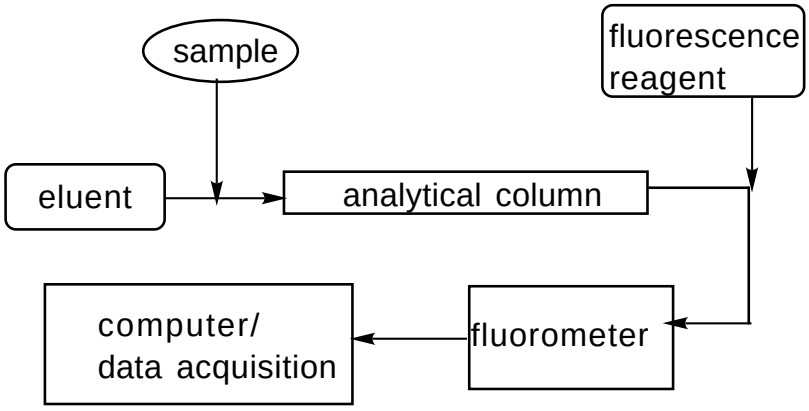

Figure 4. General schematic of HPLC system used for quantification.

and eluted with a dilute solution of sulfuric acid and EDTA . The hydrogen peroxide sample was separated on an Inertsil 5 μm ODS-2 column (MetaChem Technologies, Inc.) and then reacted with a fluorescence reagent of horseradish peroxidase and PHOPAA (p-hydroxyphenylacetic acid), the result of which is a fluorescence proportional to the quantity of hydrogen peroxide in the sample. The fluorescence is then measured using a fluorometer (LDC Analytical Fluoromonitor III). Using a personal computer and HP ChemStation, peak heights were collected for hydrogen peroxide and compared to a calibration curve to find the concentration of hydrogen peroxide in each sample.

Solutions and Reagents: The 1.0 mM hydrogen peroxide standards were prepared from a stock solution of 50 mM hydrogen peroxide, which was stored under refrigeration. The 50 mM stock solution was prepared by diluting 2 mL 30% H2O2 (J.T. Baker, Inc.) in 100 mL Milli-Q water. For the seawater standard, the stock solution was prepared with seawater so as to avoid dilution of the salts in solution upon preparation of the 1.0 mM standard. The same was done for the 50 mM hydrogen peroxide stock solutions prepared in 1 and 3 M solutions of sodium chloride.

The synthetic seawater was prepared as described in Kester et al, 1967. All salts were ACS reagent grade and were obtained from Anachemia. The sodium chloride used for the 1 and 3 M solutions was also reagent grade and was obtained from J.T. Baker, Inc.

Experimental Procedure: A general procedure was followed for each determination of the Henry's law constant of hydrogen peroxide. For trials in water, water was used to humidify the air. For the seawater and sodium chloride trails, either seawater or the appropriate sodium chloride solution, respectively, was used to humidify the zero air in the first set of coils. Coil blanks were obtained before the hydrogen peroxide standard was run through for every trial due to trace amounts of hydrogen peroxide inherent in the coil system. Water, seawater, or the appropriate sodium chloride solution was pumped through at 18^{o}C for several hours. It was found that after having run a hydrogen peroxide standard through the coils it took up to 8 hours to clean the system so that the coil blanks were no longer steadily decreasing.

After several coil blank concentrations were obtained and averaged, the hydrogen peroxide standard was run through the coils. The hydrogen peroxide standard was kept in the water bath so that it could come to thermal equilibrium with the coil system.

Again, it was found that the concentration of hydrogen peroxide in the gas phase was steadily increasing for several hours, indicating that equilibrium had not yet been reached. For this reason, the standard was also run for several hours, often for 8 or more, before data was taken.

Samples were collected every three minutes and manually injected into the HPLC. Hydrogen peroxide peaks appeared at 3.6-4.0 minute elution times and their heights were recorded. A calibration curve was obtained for the HPLC system using 50, 125, 250, 500, and 1000 nM solutions of hydrogen peroxide in water. The peak heights obtained from the coil samples were compared to the calibration curve to find the concentration in the sample.

Calculations: Once the concentration of hydrogen peroxide in the sample was obtained, the partial pressure of H_2O_2, $P_{H_2O_2}$, in the coil can be found. The ratio of $P_{H_2O_2}$ to P_{total} can be found by:

$$\frac{P_{H2O2}}{P_{total}} = \frac{22.4 \times f_a \times c_{coil}}{F_g} \qquad \textbf{Equation (1)}$$

where f_a is the aqueous flow rate through the coils (controlled using three-stop tygon tubing and Ismatec peristaltic pump), c_{coil} is the concentration of hydrogen peroxide in the gas phase (as was determined by HPLC), and F_g is the total air flow rate through the system set by the mass flow controller settings. Once $P_{H_2O_2}$ has been found from (1), the Henry's law constant can be determined as follows:

$$[H_2O_2]_{aq} = K_h P_{H2O2} \qquad \textbf{Equation (2)}$$

In the Henry's law equation, $P_{H_2O_2}$ is multiplied by four to account for the one to four dilution performed before the gas was sent to the collection coils. From these calculations, a dimensionless Henry's law constant is obtained for hydrogen peroxide in water, seawater, and 1 and 3 M sodium chloride. Alternatively, the Henry's law constant

can be determined by plotting $P_{H_2O_2}$ versus $[H_2O_2]_{aq}$ (in this case, $4P_{H_2O_2}$ was used due to the dilution). The slope of this line will be the Henry's law constant.

Results

The Henry's law constant of hydrogen peroxide in water, seawater, and 1 and 3 M sodium chloride at 18°C was found for a hydrogen peroxide standard of 1.0 mM. Table 1 summarizes our results as well as previously determined results in water at 18°C. Table 2 shows the results for the Henry's law constant of hydrogen peroxide in 1 and 3 M sodium chloride.

Figures 5 and 6 show the plot of $P_{H_2O_2}$ versus $[H_2O_2]_{aq}$ for water and seawater, respectively, for 0.5, 1.0, and 3.0 mM hydrogen peroxide solutions. The slope shown on the graph is the Henry's law constant for hydrogen peroxide in each liquid.

Table 1: Henry's Law Constants for 1.0 mM H_2O_2 in Water and Seawater at 18°C

	Water	Synthetic seawater
This Study	9.9E+04 (±13%)	1.2E+05 (±10%)
Schumb, 1955	1.3E+05	N/A
Hwang and Dasqupta, 1985	1.3E+05	N/A
Lind and Kok, 1986 & 1994	2.2E+05 (± 8%)	N/A
Staffelback and Kok, 1993	2.0E+05	N/A
O'Sullivan, 1996	1.5E+05 (±10%)	N/A

Table 2: Henry's Law Constants for H_2O_2 in 1 M NaCl and 3 M NaCl at 18°C

	1 M NaCl	3 M NaCl
This Study	1.1E+05 (10%)	1.8E+05 (10%)

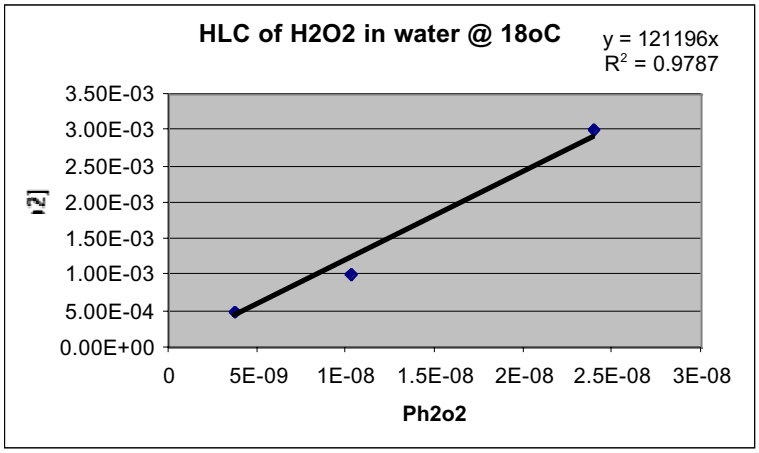

Figure 5: $P_{H_2O_2}$ versus $[H_2O_2]_{aq}$ at 18°C in water

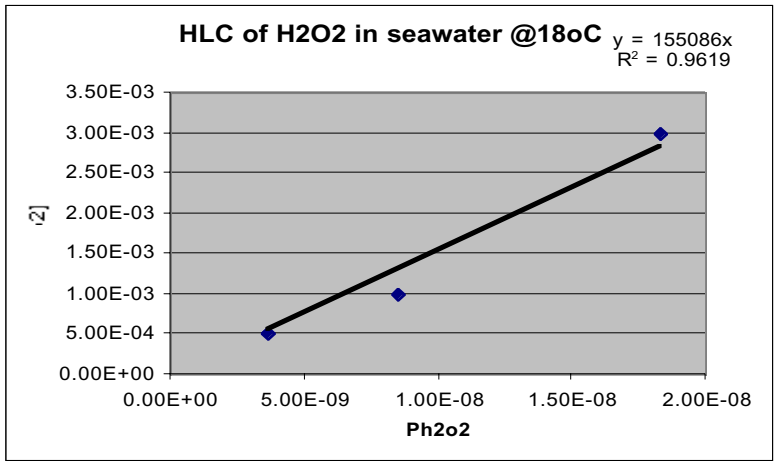

Figure 6: $P_{H_2O_2}$ versus $[H_2O_2]_{aq}$ at 18°C in seawater

Discussion

We determined the Henry's law constant of hydrogen peroxide in the synthetic seawater at 18°C to be greater than for water, meaning that more hydrogen peroxide is dissolved in the seawater than in water. Similarly, the Henry's law constant for 1 M sodium chloride was greater than for water, and the Henry's law constant in 3 M sodium chloride was greater that for 1 M sodium chloride. These results lead to the theory that

there is an association occurring between the hydrogen peroxide molecules and the salt ions, causing more hydrogen peroxide to dissolve in solutions with higher ionic strength.

While we are confident in the precision of our data due to the lengthy equilibration times, we realize that our results for water are low compared to those of other researchers. It is possible and likely that experimental error might be a cause. If the hydrogen peroxide standards used were other than 1.0 mM, the Henry's law constant would be inaccurate as compared to previous data. Leakage into or out of the system through the water bath would play a major role in affecting the actual hydrogen peroxide concentration and greatly affect the Henry's law constant. It is also possible that the partial pressure of hydrogen peroxide, $P_{H_2O_2}$, was high. As shown in Equation 1 above, $P_{H_2O_2}$ is calculated from aqueous flow rates, gas flow rates, and the total pressure, P_{total}. If F_g, the total air flow rate through the system, was measured to be lower than it actually was from incorrect calibrations, $P_{H_2O_2}$ would be high. It is also possible that the total pressure, P_{total} or the aqueous flow rate, f_a, were measured to be higher than they actually were. While any of these experimental difficulties might be an important factor, we are still confident that the Henry's law constants increased for solutions of higher activity.

Other researchers have found similar results when looking at Henry's law constants in seawater solutions. *Kucklick et al.* [1991] studied the temperature dependence of the Henry's law constants of hexachlorocyclohexanes in distilled water and artificial seawater. While hexachlorocyclohexanes are not related to hydrogen peroxide, the fact that they also saw a significant increase in the Henry's law constant in seawater over water at high temperatures is encouraging.

Also of interest is the work done by *Lind and Kok* [1986] with hydrogen peroxide in dilute sulfuric acid and solutions of ammonium sulfate. They found that the Henry's law constant increased in solutions of ammonium sulfate. This points to associations between ions in solution and hydrogen peroxide as the cause of the increasing Henry's law constant. *Lind and Kok* [1986] also found that the Henry's law constant of hydrogen peroxide decreased in sulfuric acid solution. On the other hand, *Staffelbach and Kok* [1993] reported an increase in Henry's law constants at pH values of 2.1 to 2.4 as compared to those at neutral pH. All of these results lead to more questions than answers.

Clearly, the dynamics of the hydrogen peroxide/seawater system are complex. Numerous factors play important roles in determining how hydrogen peroxide will dissolve in seawater, including pH, temperature, salinity, ion character, and activity. Since seawater is not just salt, but also contains organic matter that might affect the solubility, it is also important to examine the behavior of hydrogen peroxide in real seawater.

Since our system in particular has proven difficult to control, an important next step is to determine the cause of the complications we encountered, including the lengthy equilibration times and difficulty cleaning the system. Once this is done, the temperature dependence of the Henry's law constant of hydrogen peroxide in seawater could be determined in an effort to verify our conclusions.

Conclusions

The Henry's law constants of hydrogen peroxide in synthetic seawater, 1 M, and 3 M sodium chloride were found at 18^{o}C. This was done using a system of continuous-flow glass scrubbing coils as described in *O'Sullivan et al.* [1996] to establish equilibrium between an aqueous concentration of hydrogen peroxide and air and high performance liquid chromatography for quantification as described in *Lee et al.* [1995]. It was found that the Henry's law constant of hydrogen peroxide in a synthetic seawater solution is greater than in water. Similarly, it was found that more hydrogen peroxide dissolved in a 1 M sodium chloride solution than in a 3 M sodium chloride solution. These trends point to an association between hydrogen peroxide and ions in solution as the cause of the increasing in Henry's law constant.

Acknowledgement. The research presented was supported by NASA grant NCC 1302 and the NSF SURFO program at the Graduate School of Oceanography, University of Rhode Island. I would like to thank Julie Snow and Dr. Brian Heikes for their support and guidance, as well as Dr. Dana Kester, Dr. Rob Pockalny, and Dr. Daniel O'Sullivan.

References

Calvert, J.G., A.L. Lazrus, G. Kok, B. Heikes, J.Walega, J. Lind, and C. Cantrell, Chemical mechanisms of acid generation in the troposphere, *Nature, 317,* 27-35, 1985.

Kucklick, J.R., D.A. Hinckley, T.F. Bidleman, Determination of Henry's law constants for hexachlorocyclohexanes in distilled water and artificial seawater as a function of temperature, *Mar. Chem. 34*, 197-209, 1991.

Lee, M., B.C. Noone, D. O'Sullivan, and B.G. Heikes, Method for the collection and HPLC analysis o hydrogen peroxide and C1 and C2 hydroperoxides in the atmosphere, *J. Atmos. Oceanic Technol. 12*, 1060-1070, 1995.

Lind, J.A. and G.L. Kok, Henry's law determinations for aqueous solutions of hydrogen peroxide, methylhydroperoxide, and peroxyacetic acid, *J. Geophys. Res. 91,* 7889-7895, 1986.

Logan, J.A., M.J. Prather, S.W. Wofsy, and M.B. McElroy, Tropospheric chemistry: a global perspective, *J. Geophys. Res. 86*, 7210-7254, 1981.

O'Sullivan, D.W., M. Lee, B.C.Noone, B.G. Heikes, Henry's law determinations for hydrogen peroxide, methyl hydroperoxide, hydroxymethyl hydroperoxide, ethyl hydroperoxide, and peroxyacetic acid, *J. Phys. Chem. 100,* 3241-3247, 1996.

Staffelbach, T.A. and G. Kok, Henry's law constants for aqueous solutions of hydrogen peroxide and hydroxymethyl hydroperoxide, *J. Geophys. Res. 98*, 12,713-12,717, 1993.

Distribution of Anthropogenic Contaminants in Sediments and Suspended Particles in Narragansett Bay, Rhode Island

Teresa Dennison
Maine Maritime Academy

Prepared for:
The Summer Undergraduate Research Fellowship in Oceanography

Advisors:
Dr. Elizabeth Lacey Laliberte
Dr. John King

Graduate School of Oceanography
University of Rhode Island

August 2000

Abstract

Surficial sediments and sediment traps from 11 stations throughout Narragansett Bay were analyzed for grain size and trace metal concentrations of zinc, lead, nickel, copper, and cadmium. Most surface sediments have a high percentage of silt and clay, whereas the sediment traps have a higher proportion of silt. Trace metal concentrations were normalized by grain size in order to get results independent of lithology. Trace metal concentrations have decreased in the northern Providence River, whereas resuspension and down bay transport has decreased sediment quality further down the River and Bay. All of the sediments analyzed had trace metal concentrations below the ER-M, but it is likely that a small percentage of the biota may have been affected by the observed contaminant concentrations. Historical studies have shown an exponential decrease in trace metal concentration down the bay, however, the results of this study show that there is a mid-bay increase in Narragansett Bay due to resuspension events.

Introduction

Historically many industries and sewage treatment plants have disposed of effluent in the Providence River. An increase in population and industrial activities has affected the environment of the Narragansett Bay and caused an increase in the influx of domestic and industrial waste into the Bay (Corbin, 1989). The contaminants come from both point and non-point sources. Point sources include facilities that discharge directly into surface waters through a pipe (e.g. sewage treatment plant effluent) on a regular basis. Non- point source discharge is the transport of dissolved and particulate materials to surface waters, via surface runoff from precipitation (NOAA/EPA, 1988).

Seasonal and episodic events such as rainstorms, tide and wind currents, ship activities, dredging, etc. may lead to the resuspension of sediments and significant changes in the concentration of dissolved oxygen, chemical contaminants, and nutrients of marine waters. These events may also lead to the input, remobilization and transport of chemicals in the water column. It is known that the Providence and Taunton Rivers (Figure 1) have increased contaminant concentrations in the surficial sediment, resuspended sediment, and water column. Previous studies have shown that most contaminant concentrations decrease exponentially down the Bay (Bender et al., 1988, Corbin, 1989, King et al., 1995). King et al. (1995) found that the freshwater flow from the Providence River significantly affected the distribution of anthropogenic metals in the surface sediments of the Narragansett Bay. Approximately ninety percent of the fresh water entering the Bay comes from the Providence and the Taunton Rivers and drains rural and urban areas (Bender et al., 1989). Figure 2 shows the distribution of freshwater transport from the Providence and Taunton Rivers, as well as freshwater current flows.

There are many sources of metals into the Narragansett Bay System. Rivers bring metals into the bay as a result of weathering and from the accumulation of domestic and industrial effluent and waste. Some metals enter the Bay through atmospheric deposition, whereas others enter and exit the Bay through the tides (Bender, 1989). The anthropogenic metals cadmium, lead, copper, zinc, and nickel are the dominant inputs of the metal load of rivers and sewage treatment plants, which occur at the head of the Bay. Due to the historic combustion of leaded gasoline, lead has also had atmospheric transportation and deposition, therefore an additional input for lead is atmospheric

deposition, (Nixon, 1991). King et al. (1995) found that the Providence River was a major source of anthropogenic metals into the Bay.

Trace metals effect biochemical systems of all organisms. Many trace metals are essential nutrients. At high levels however, they can be toxic. Metal loading has increased due to human activities (Bender et al., 1989). Trace metals are transported to the sediments from the water by many pathways. In general, when dissolved metals from natural or anthropogenic sources come in contact with saline waters, they are quickly adsorbed onto particulate matter and are removed from the water column to the bottom sediments (Windom, 1988). Once deposited, stability depends on the chemical association of metals and the chemistry of the sediment/ interstitial pore waters. The rapid settling of particle associated metals to the sediment interface happens under " normal" physical and chemical conditions (King et al., 1995).

There are several factors that can affect the accumulation of metals in sediments. The amount of the contaminant input to an area that is available for accumulation in sediments, the grain size, and the organic carbon content – organic material may form complexes with metals in the sediment or interstitial waters, are some of the many factors (King et al., 1995).

Trace metal concentrations have significantly decreased in the northern section of the Providence River, whereas resuspension and down bay transport of sediments have degraded sediment quality down the river and further down Bay (CICEET Prop, 1999). Metals in the Bay exist in dissolved and particulate forms. Dissolved metals may be bound up in dissolved organic matter (Bender et al., 1989). Absolute metal concentrations in coastal sediments are influenced by a variety of factors including sediment mineralogy, grain size, organic content, and anthropogenic enrichment (Windom, 1988). The grain size of the surface sediments and the trap material are favorable for accumulating trace metal contaminants because they are mostly silts and clays.

An examination of surface sediments and resuspended sediments yield information on the impact of anthropogenic contaminants on the Providence River and Narragansett Bay. In this study, surficial sediments and sediment trap material from selected locations in Narragansett Bay were analyzed for anthropogenic trace metals (zinc, copper,

cadmium, lead, and nickel). In order to characterize sediment quality, grain size was also determined. Normalization of trace metal concentration by grain size indicates contaminant concentration independent of lithology. The results are show a mid bay increase in trace metals due to the resuspension events.

Setting

Narragansett Bay is located in south- eastern New England with a North-South orientation (Figure 1). Glacial processes have modified this drowned river valley making it a complex depositional environment. As sea levels changed, beach and estuarine sediments were deposited. Sediment accumulation is governed by estuarine sedimentation processes that have deposited fine sediments in the upper and middle bay areas, with sandy sediment at the mouths of the passages (McMaster, 1960). Natural estuarine sediments are predominately composed of river transported debris resulting from continental weathering (Windom, 1988). Narragansett Bay covers 328 km^2, draining 4708 km^2, most of which lies in Massachusetts (Corbin, 1989; Pilson, 1985). The Narragansett Bay System can accommodate all the sediment input it receives (Nichols, 1986) and has a relatively high ability to retain suspended particles and attached pollutants (NOAA/EPA, 1989).

Narragansett Bay is a two-layered tidal estuary with non-tidal surface flow out of the Bay toward the South and bottom flow into the Bay toward the North (McMaster, 1960). The Providence River is a partially mixed estuary due to freshwater input (Corbin, 1988), whereas the Taunton River becomes a salt wedge during high periods of flow (King et al., 1995). Natural metal concentrations vary widely among estuaries (Windom, 1988).

Materials and Methods

Surface sediments and suspended particulate material was collected at 11 sites throughout Providence River and Narragansett Bay (Figure 1), the sites are listed in Table 1. Surface sediment was collected using a small grab sampler. The top two centimeters of sediment was subsampled in the field using acid- cleaned teflon coated titanium tools. Sediment traps were deployed and surface sediments were collected in March, 2000. In

June, 2000 sediment traps and surface sediments were collected again. The trap at station one was not present during the June collection. Sediment traps are used to get a representative sample of suspended particulate material from the water column and see if contaminated material is moving down bay. The type of trap used is a Gardner trap, with a diameter of 10 cm and an aspect ratio (height/ diameter) of 1.5 (King et al., 1995). (Figure 3). In the lab, the sediment is removed from the traps and placed in acid cleaned containers so it can be prepared for analyzing. Analyses included grain size and total trace metal concentration.

Grain size distribution of the sediment samples was determined using an Elzone 180 XY Particle Size Analyzer. This instrument measures the average diameter of a particle by passing it through a constant electrical current. The disruptance of the current is proportional to the size of the particles. Sample preparation involves acidifying 5-10 grams of wet sediment in acetic acid to remove inorganic carbon. Fifty milliliters of thirty- percent hydrogen peroxide is added to remove organic matter. The sample is then rinsed with ultra-purified deionized water and the >63 *u*m fraction is separated by sieving and the weight is determined. The remaining sediment is < 63 *u*m and a few drops of it are dispersed in 4% Sodium Pyrophosphate solution and introduced into the particle size instrument. All data is ultimately reported as a percentage of the total sample for 3 different sizes: silt, clay, and sand (Table 2). For this study, percent clay and silt data are used because that that is where sediment contaminants preferentially bind. The first step in the study of trace metals in sediments is usually the correction for grain size as there is a marked decrease in the level of metal contaminants as the sediment particle size increases (Forstner et al., 1978).

Adsorptive bonding and complexation by organic material results in the removal of metals from an aqueous solution and transformation into a solid. The adsorption of metals onto the surfaces of clay minerals is due to charge differences between clay particles and metals. A strong bond is formed from the metals and the particle surface by electrostatic charge. The greater the surface area the greater the binding. (King et al., 1995).

Much of the natural component of metals in estuarine sediments is chemically bound in aluminosilicate structures (Windom, 1988). Metals are present as cations, whereas clay minerals posses a negative charge as the result of an Al^{+3} substitution for Si^{+4} (King

et al., 1995). The adsorbed anthropogenic component is more loosely bound, which may make it more available to estuarine biota and when sediments are disturbed it may be released into the water column in altered forms (Windom, 1988). It is likely that metals from off shore waters will be retained in areas that have an abundance of fine particles suspended in the water column, like the areas and sediments analyzed in this study.

In addition to grain size determination, the concentration of trace metals were determined. In order to determine trace metal concentration, a total sediment digestion was performed. Approximately 5 grams of wet sediment was added to a sterile centrifuge tube and freeze dried for two days. Then 0.2 grams of homogenized sediments were added to the teflon digestion vessels. Working under a fume hood, 1.0 ml of concentrated hydrochloric acid and 5.0 ml of concentrated nitric acid were added to each vessel. When no reaction was evident, 4.0 ml of concentrated hydrofluoric acid was added to each vessel. The vessels were then racked and placed in a heated sonicator, which was filled with deionized water until approximately 2 cm below the base of the caps. The sonicator was covered and ran with the heat on for 48 hours. After cooling, 30 ml of 5 % boric acid was added and the contents were transferred into 50-ml volumetric flasks. The digestion vessels were rinsed with deionized water and added to the flasks. The solution is then added to acid- striped polyethylene bottles and labeled appropriately.

To analyze for trace metal concentrations the digested samples were analyzed by a graphite furnace atomic absorption spectrophotometry (AA) using a Perkin-Elmer 4100 AA. Standards of a known concentration were analyzed and a calibration curve of .99 or better was required for each element. Sample absorbence data obtained by the instrument was compared to a standard curve in order to calculate the metal concentration in samples. A certified standard reference material, MESS 2, was used to test for accuracy. MESS 2 consists of dried homogenized marine sediment from the Beaufort Sea. It has been tested for 19 trace elements within the 95% confidence limit (National Resource Council, 1981).

After the trace metal concentrations were obtained from the AA, they were normalized by grain size. Trace metal concentrations are normalized to grain size in order to indicate contaminant concentrations independent of lithology. Normalizing grain size has various methods. One method used successfully in coastal waters is to

determine the linear relationship between contaminant concentration and the fraction of the size distribution that is smaller than 63*u*m after King et al. (1995). The contaminant concentrations are then normalized to grain size by dividing the contaminant concentration by the percent silt and clay combination (Table 3). This is done because contaminants are more strongly attracted to clay particles than sand particles.

Results and Discussion

The results of the grain size analysis are listed in Table 2. The percentage of sand, silt, and clay from the surface sediments are plotted at each station in figure 4. The grain size distribution for every sediment trap, except station one, is plotted on figure 5. In the surface sediment at all stations except for station one, there was a high percentage of silt. Station one had a high percent of sand and no clay was present. The sediment trap showed an even greater proportion of silt than the surficial sediment at each of the stations. All of the other stations had a higher percentage of clay than sand.

The results of the trace metal concentrations in the surface sediments and sediment traps are summarized in Table 3. Variations in the metal concentrations in the surface sediments and sediment traps for three different flow patterns down the bay are shown in Figures 6-8. It can be seen from these graphs that there is a slight increase in concentrations near the mid- bay area. Figure 6 shows a mid- bay increase in anthropogenic contaminants for the West Passage flow pattern starting near Rumstick Neck. Both flow patterns for the East Passage show an increase in anthropogenic contaminant concentrations (Figures 7 &8).

The normalized concentrations are shown in Table 4. Figures 9 -11 show the variation in the normalized data of the surficial sediments and sediment traps for different flow patterns down the bay. The normalized graphs show that there is not an exponential decrease in contaminant metal concentration down the bay. There is a notable decrease in the concentration from station 6 down the bay, but it is not an exponential decrease. It is harder to see the mid- bay increase in the normalized data for surface sediments because of the high percentage of sand at station one. The sediment traps show the mid-bay increase better because they had a higher ratio of silt and clay than the surface sediments.

In order to characterize sediments, the concentrations of the metals found were compared to the sediment quality guidelines of Long et al. (1995). These guidelines are estimated by comparing sediment contaminant concentration data and observed biological effects in a large number of marine and estuarine settings. The incidence of effects was quantified within three concentration ranges: (1) less than effects range- low (ERL), (2) ERL to effects range- median (ERM), and (3) greater than ERM (King et al., 1995).

The guidelines for the contaminants analyzed in this study are shown in Table 5. The ERL is the range at which a small number of organisms could be affected by the chemical contamination concentration. Below the ERL the biota of an area are not likely going to be affected by the trace metal concentration levels. Trace metal concentrations above the ER-M have a high probability for biological effects.

Figures 12 and 13 show the ERL of the metals analyzed in this study for all the surface sediment sites and sediment traps respectively. In the surface sediments and trap material analyzed, the trace metal concentrations were all below the ER-M. Surficial sediments show, as seen in figure 12, that nickel and zinc were below the ERL at stations 7 and 9. Station 10 was below the ERL for all anthropogenic contaminants tested for. Every metal was below the ERL at station one. Cadmium was below the ERL for all the stations. Sediment traps, as seen in figure 13, show the same trend for Cadmium. Nickel was below the ERL at station 6. For much of the East passage flow pattern zinc was below the ERL.

For most of the metals tested, with the main exception being cadmium, there is a possibility that a small percent of the biota might be affected by the metal concentrations of the materials analyzed at most stations. Sediment traps showed high levels of contaminants, sometimes being higher than the surface sediments. Figure 6 shows that most of the trap material, in the flow pattern of the West Passage, was higher than surface sediments. Sediment trap 7 has higher contaminant concentrations than surface sediments for all anthropogenic trace metals except cadmium. Station 4 has higher trap values for all the anthropogenic trace metals except cadmium and nickel (Figure 7). Copper, lead, and nickel have higher sediment trap concentrations than the surface

sediments (Figure 8). This could be due to the fact that resuspension can cause the remobilization and transport of chemicals in the water column.

Conclusions

Seasonal and episodic events may lead to the resuspension, and transport of chemical contaminants in the water column. There are many sources of anthropogenic trace metal contaminants into the Narragansett Bay. Trace metals are being transported to sediments by being adsorbed to particulate matter. Smaller particles have greater surface area to volume ratios. Clays have a negative charge that attracts positively charged trace metals. The decrease in sediment quality of the Narragansett Bay is due to the resuspension of sediments with anthropogenic trace metal contaminants.

Grain size analysis showed that sediment traps had a higher proportion of silt than the surficial sediments. Sediment trap material had higher levels of contaminant concentrations then the surface sediments at some stations. Sediment quality analysis showed that a small percentage of the biota might be affected by the concentration of the anthropogenic contaminants. Surficial sediment and sediment traps that were analyzed for chemical contaminant concentrations and grain size show a mid- bay increase in the chemical contaminant concentration for three possible flow patterns in Narragansett Bay.

REFERENCES

Bender, M., D. Kester, D. Cullen, J. Quinn, J. King, D. Phelps, and C. Hunt, Trace metal pollutants in Narragansett Bay waters, sediments, and shellfish, Report to the Narragansett Bay Project.

Cooperative Institute for Coastal and Estuarine Environmental Technology (CICEET) FY99 Proposal Application, 1999.

Corbin, J., 1989. Recent and historical accumulation of trace metal Contaminants in Narragansett Bay sediments, RI, M.S. Thesis, University of Rhode Island, Kingston, RI, 295 pp.

Forstner, U., Muller, G., and Stoffers, P., 1976. Heavy metal contamination in Estuarine and coastal sediments: sources, chemical association and diagenetic effects. In: Biochemistry of estuarine sediments, Proceedings of a UNESCO/SCOR workshop held in Melreux, Belgium. November 29, to December 3, 1976, UNESCO, 49-69.

King, J., J. Corbin, R. McMaster, J. Quinn, P. Gangemi, D. Cullen, J. Latimer, J. Peck, C. Gibson, J. Boucher, S. Pratt, L. LeBlanc, J. Ellis, and M. Pilson, 1995. A study of the sediments of Narragansett Bay, Vol. I: The surface sediments of Narragansett Bay, Final Report submitted to Narragansett Bay Project, March, 31, 203pp.

Long, E. R., D.D. MacDonald, S.L. Smith, and F. D. Calder, 1995. Incidence ofAdverse biological effects within ranges of chemical concentrations in marine and estuarine sediments, Environmental Management, Vol. 19(1): 81-97.

McMaster, R.L., 1960. Sediments of the Narragansett Bay system and RhodeIsland Sound, Rhode Island, *Journal of Sedimentary Petrology*, 30(2): 249-274.

National Research Council of Canada, 1981. MESS-2, BCSS-1, PACS-1: MarineSediment reference materials for trace metals and other constituents, Institute for Environmental Research and Technology, Canada.

Nichols, M., 1986. Storage efficiency of estuaries. In: River Sedimentation, Volume 3, (Wang, S., H. Shen, and L. Ding, eds.), Proceedings of the Third International Symposium on River Sedimentation, The University of Mississippi, 273-289.

Nixon, S.W., 1991. Recent metal inputs to Narragansett Bay, Final ReportSubmitted to the Narragansett Bay Project, 57pp.

NOAA/EPA Team, 1989. Susceptibility of east coast estuaries to nutrientdischarges: Passamaquoddy Bay to Chesapeake Bay, Summary Report on Near Coastal Waters.

Pilson, M.E.Q., 1985. On the residence time of water in Narragansett Bay, *Estuaries,* 8(1): 2-14.

Windom, L.H., 1988. A guide to the interpretation of metal concentrations inEstuarine sediments, Florida Department of Environmental Regulation Coastal Management Zone.

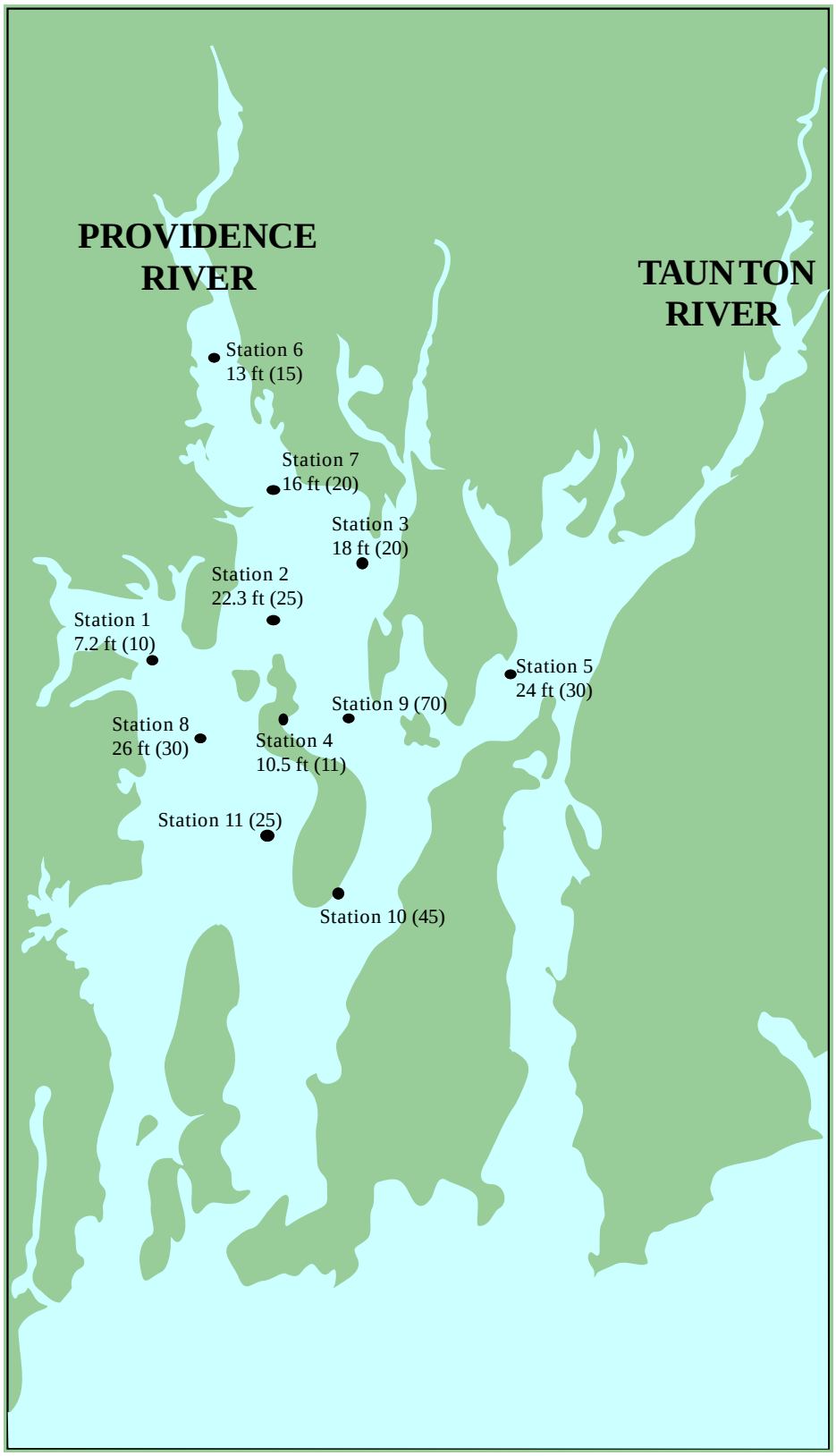

Figure 1. Station locations within Narragansett Bay. Water depth (in feet) of each station is shown in parentheses.

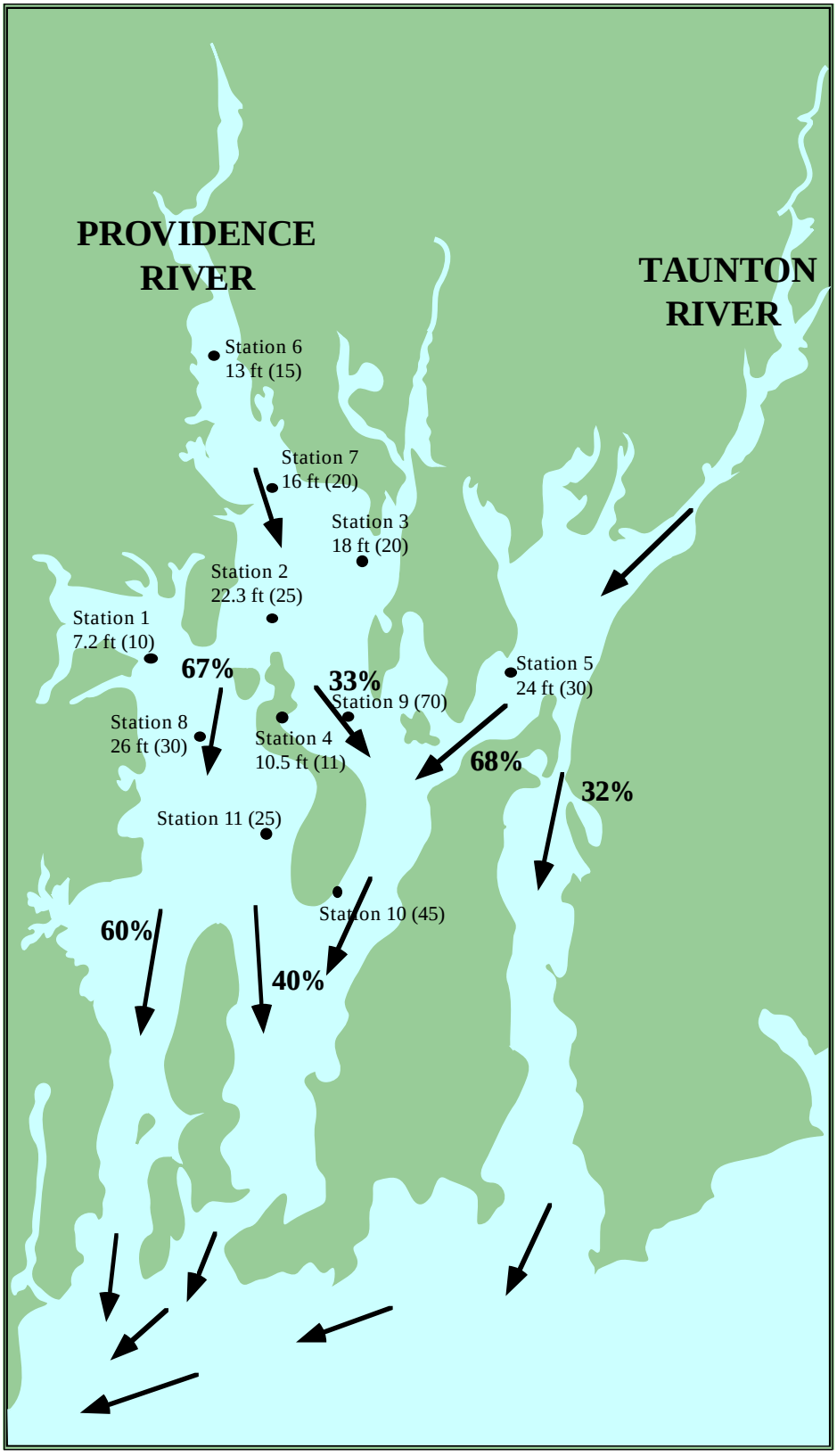

Figure 2. Freshwater surface flow and directional percentage

Table 1. Site location of surface samples and sediment traps.

Station	**Location**	Latitude	Longitude
Station 1	Off Sandy Point	41 39.6344'N	71 23.9030'W
Sed. Trap 1	Off Sandy Point	41 30.6227'N	71 23.9128'W
Station 2	Ohio Ledge	41 41.011'N	71 20.456'W
Sed. Trap 2	Ohio Ledge	41 41.016'N	71 20.457'W
Station 3	Rumstick Neck	41 41.6054'N	71 18.0941'W
Sed. Trap 3	Rumstick Neck	41 41.5494'N	71 18.0347'W
Station 4	Prudence Island Harbor(near dock)	41 38.504'N	71 20.424'W
Sed. Trap 4	Prudence Island Harbor(near dock)	41 38.502'N	71 20.434'W
Station 5	Off Hope Point	41 40.2143'N	71 13.8342'W
Sed. Trap 5	Off Hope Point	41 40.1730'N	71 13 8404'W
Station 6	Sabin Point	41 46.1458'N	71 22.2672'W
Sed. Trap 6	Sabin Point	41 46.1030'N	71 22.2963'W
Station 7	Nayatt Point (near lighthouse)	41 43.2629'N	71 20.5440'W
Sed. Trap 7	Nayatt Point (near lighthouse)	41 43.2118'N	70 20.5053'W
Station 8	Middle of West Passage(N of Allen Harbor)	41 38.4481'N	71 23.0433'W
Sed. Trap 8	Middle of West Passage(N of Allen Harbor)	41 38.3052'N	71 23.1367'W
Station 9	"deep hole"	41 37.856'N	71 17.747'W
Station 10	T dock	41 34.697'N	71 19.184'W
Sed. Trap10	T dock	41 34.701'N	71 19. 187'W
Station 11	Off Hope Island	41 36.157'N	71 20.995'W
Sed. Trap11	Off Hope Island	41 36.157'N	71 21.000'W

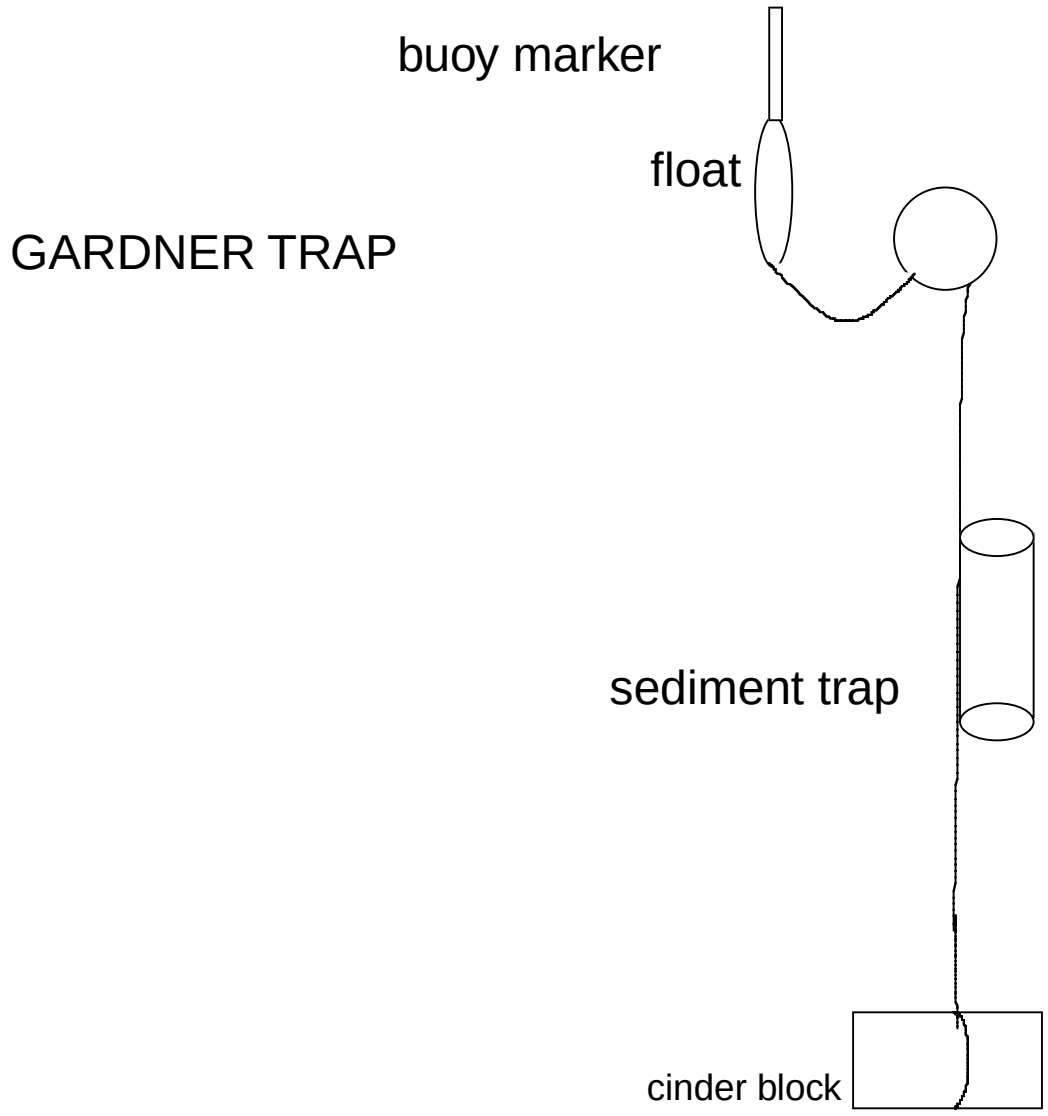

Figure 3. Diagram of a Gardner trap.

Table 2. Percent composition of sediments.

	DRY WEIGHT (g)		% Vol	% Vol				%SILT	
Sample Name	**>63**	**<63**	**>3.9u**	**>15.6u**	**% SAND**	**% SILT**	**%CLAY**	**63-15.6u**	**<15.6u**
Station 1	3.86	0.05	97.42	31.66	98.8	1.1	0.0	0.4	0.8
Station 2	0.17	0.85	92.3	11.27	16.6	77.0	6.4	9.4	74.0
Station 3	0.19	0.65	98.68	58.77	22.9	76.1	1.0	45.3	31.8
Station 4	0.17	0.46	96.66	21.85	27.2	70.4	2.4	15.9	56.9
Station 5	0.17	1.22	97.38	20.13	12.1	85.6	2.3	17.7	70.2
Station 6	0.70	0.62	96.45	17.82	53.2	45.1	1.7	8.3	38.5
Station 7	0.67	0.19	94.94	13.12	77.7	21.1	1.1	2.9	19.4
Station 8	0.27	1.20	96.14	23.86	18.5	78.3	3.1	19.4	62.0
Station 9	1.52	1.45	98.35	24.95	51.1	48.1	0.8	12.2	36.7
Station 10	2.48	0.57	99.92	26.76	81.2	18.8	0.0	5.0	13.7
Station 11	0.46	1.60	100	23.69	22.3	77.7	0.0	18.4	59.3
sediment trap 2	0.03	0.55	96.31	16.79	5.2	91.3	3.5	15.9	78.9
sediment trap 3	0.04	0.66	94.4	4.335	6.3	88.5	5.2	4.1	89.7
sediment trap 4	0.02	0.16	100	29.45	10.1	89.9	0.0	26.5	63.5
sediment trap 5	0.03	1.24	97.12	17.78	2.7	94.5	2.8	17.3	80.0
sediment trap 6	0.008	0.038	98.32	24.59	17.4	81.2	1.4	20.3	62.3
sediment trap 7	0.032	0.34	93.85	12.79	8.6	85.8	5.6	11.7	79.7
sediment trap 8	0.048	0.618	96.58	16.22	7.2	89.6	3.2	15.1	77.7
sediment trap 9	0.14	1.128	98.18	29	11.0	87.3	1.6	25.8	63.2
sediment trap 10	0.081	1.115	100	1.043	6.8	93.2	0.0	1.0	92.3
sediment trap 11	0.005	0.193	95.45	13.82	2.5	93.0	4.4	13.5	84.0

Table 3.
Anthropogenic contaminant concentrations for surface sediments and sediment traps.

	Cd (ug/g)	Cu (ug/g)	Pb (ug/g)	Ni (ug/g)	Zn (ug/g)
Station 1	0.095	9.2	14.87	2.72	13.4
Station 2	0.405	102.7	78.7	26.43	229
Station 3	0.566	97.8	73.1	23.44	275
Station 4	0.811	99.7	82.7	22.02	260
Station 5	0.261	55.8	68.3	23.65	172
Station 6	0.718	205	125	20.8	263
Station 7	0.195	40.7	35.8	7.5	116
Station 8	0.395	96	87.7	23.1	282
Station 9	0.202	38.1	47	14.7	81
Station 10	0.081	17.4	26	11.61	101
Station 11	0.162	38.4	44.9	19.7	236
Sed. Trap 2	0.244	117.3	92.3	29.2	253
Sed. Trap 3	0.262	106	86.3	28.7	120
Sed. Trap 4	0.471	178.2	79.5	24.8	295
Sed. Trap 5	0.215	56.4	66	26.6	227
Sed. Trap 6	0.673	135.8	118.7	19.1	233
Sed. Trap 7	0.333	99.2	84.2	24.68	134
Sed. Trap 8	0.24	80	71.5	27.66	268
Sed. Trap 9	0.132	49.5	59.9	26.48	118
Sed. Trap 10	0.148	45.2	54.6	24.92	128
Sed. Trap 11	0.201	47.2	49.1	24.98	202
Blank 1 (ug/l)	0.27	1	0	0.21	nd
Blank 2 (ug/l)	0.22	0.8	1.8	0.21	7.7
MESS 2 #1	0.267	34.5	21.4	47.9	230
MESS 2 #2	0.257	36.9	21.23	49.4	205
MESS 2 #3	0.267	36.7	22.71	36	211
Sed.Trap 2 dup	0.268	113.1	87.4	29.4	198

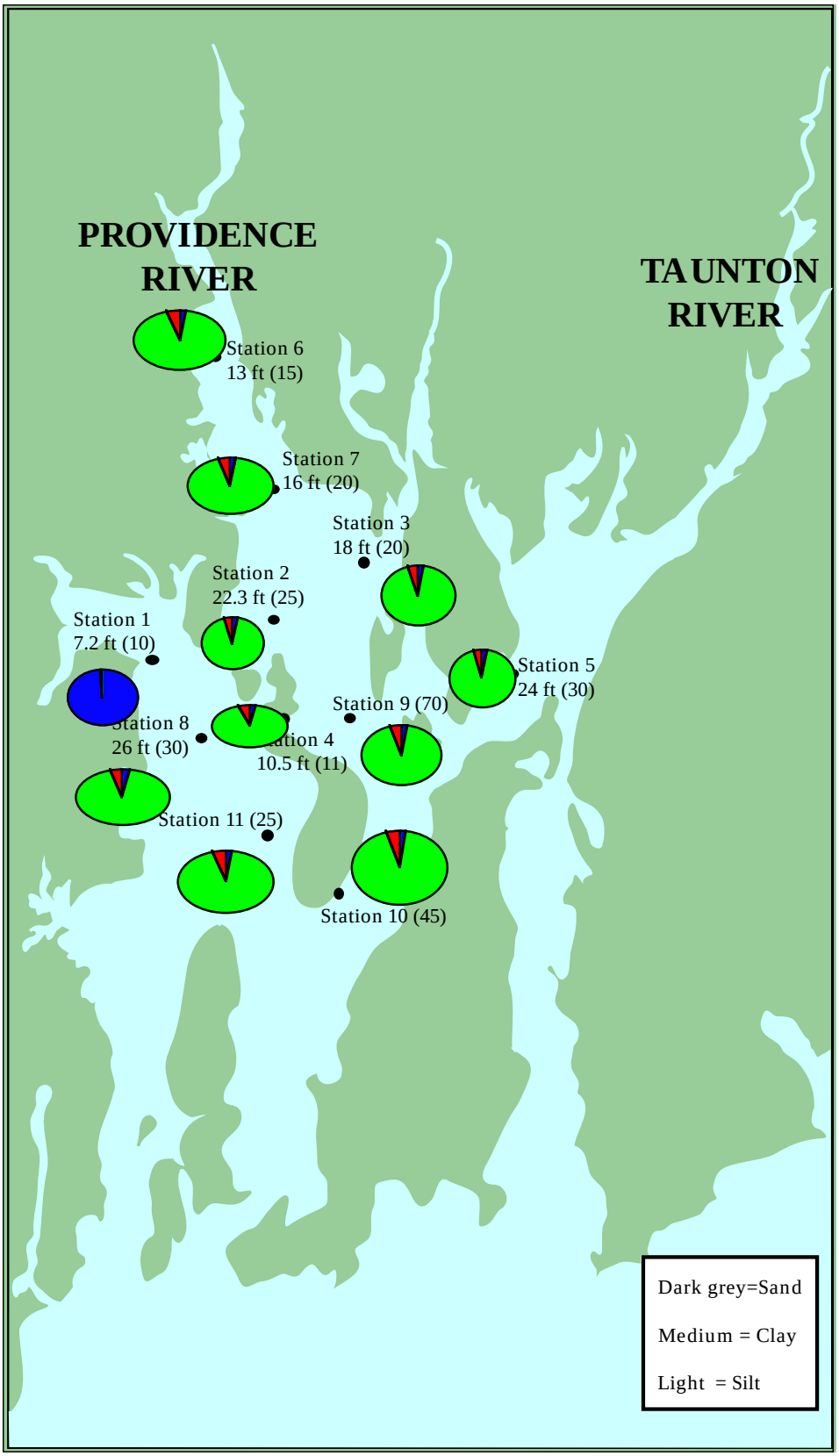

Figure 4. Surface sediments

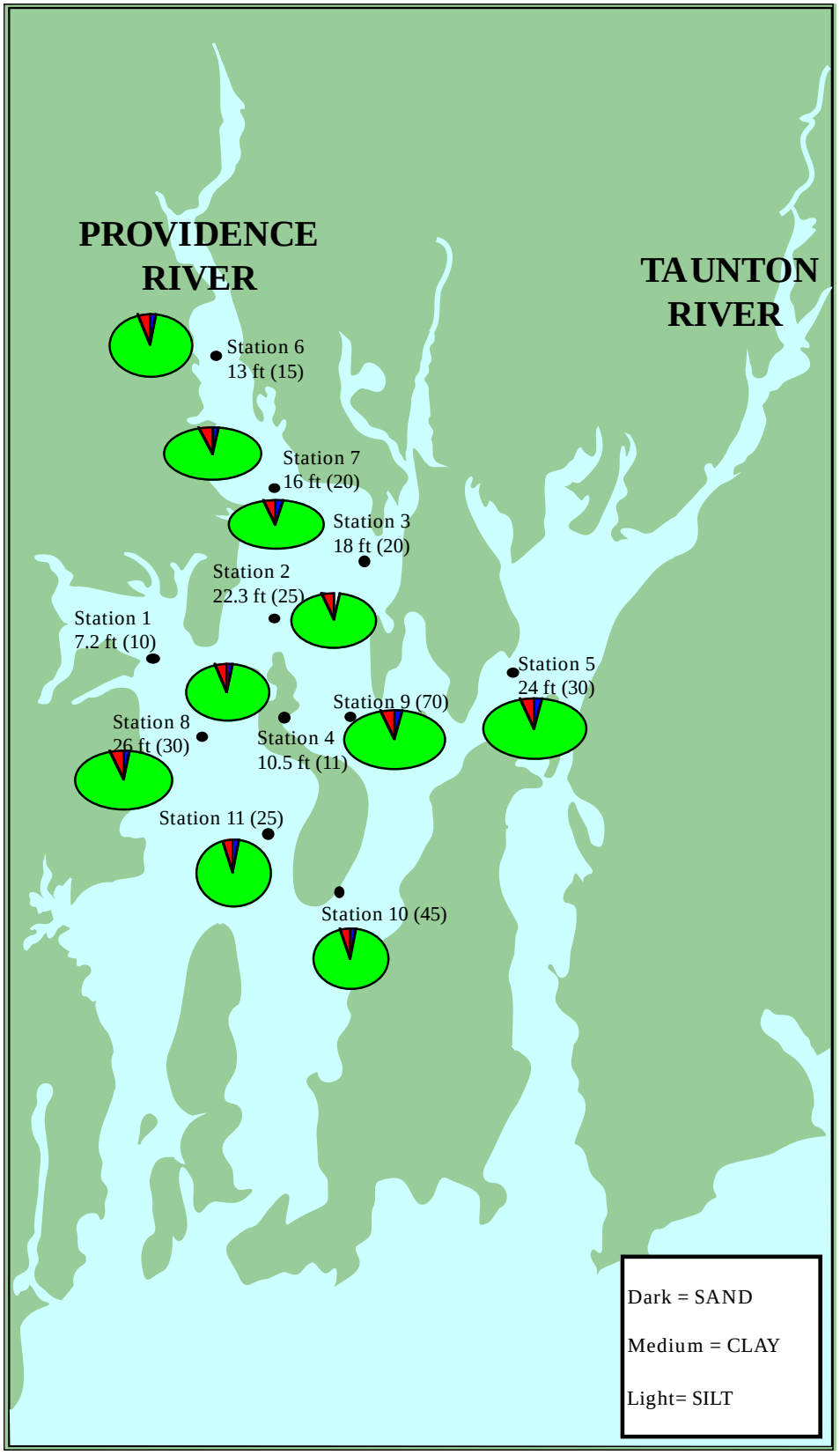

Figure 5. Grain size distribution of sediment traps.

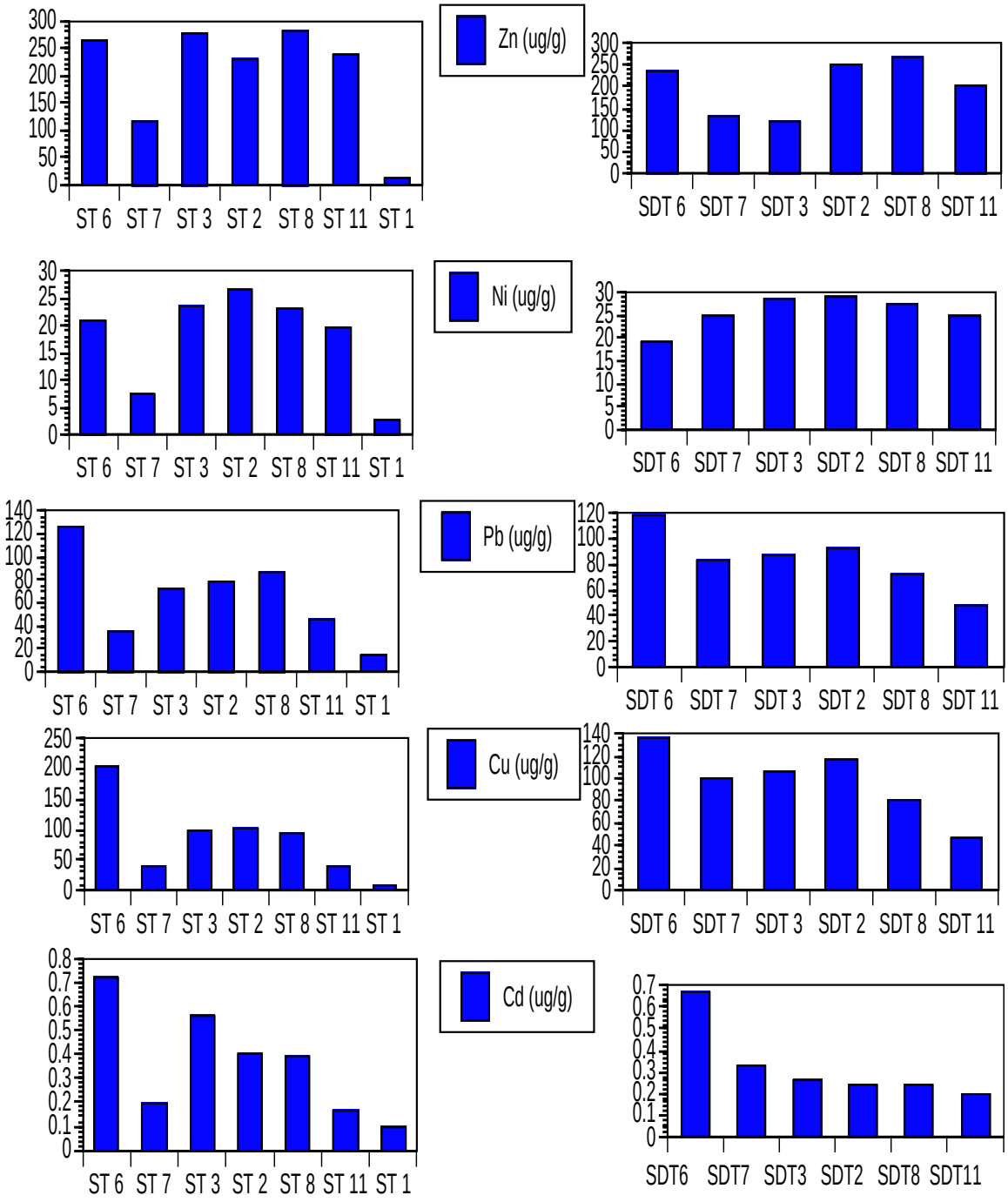

Figure 6. Anthropogenic concentrations of a possible flow pattern down the West Passage.

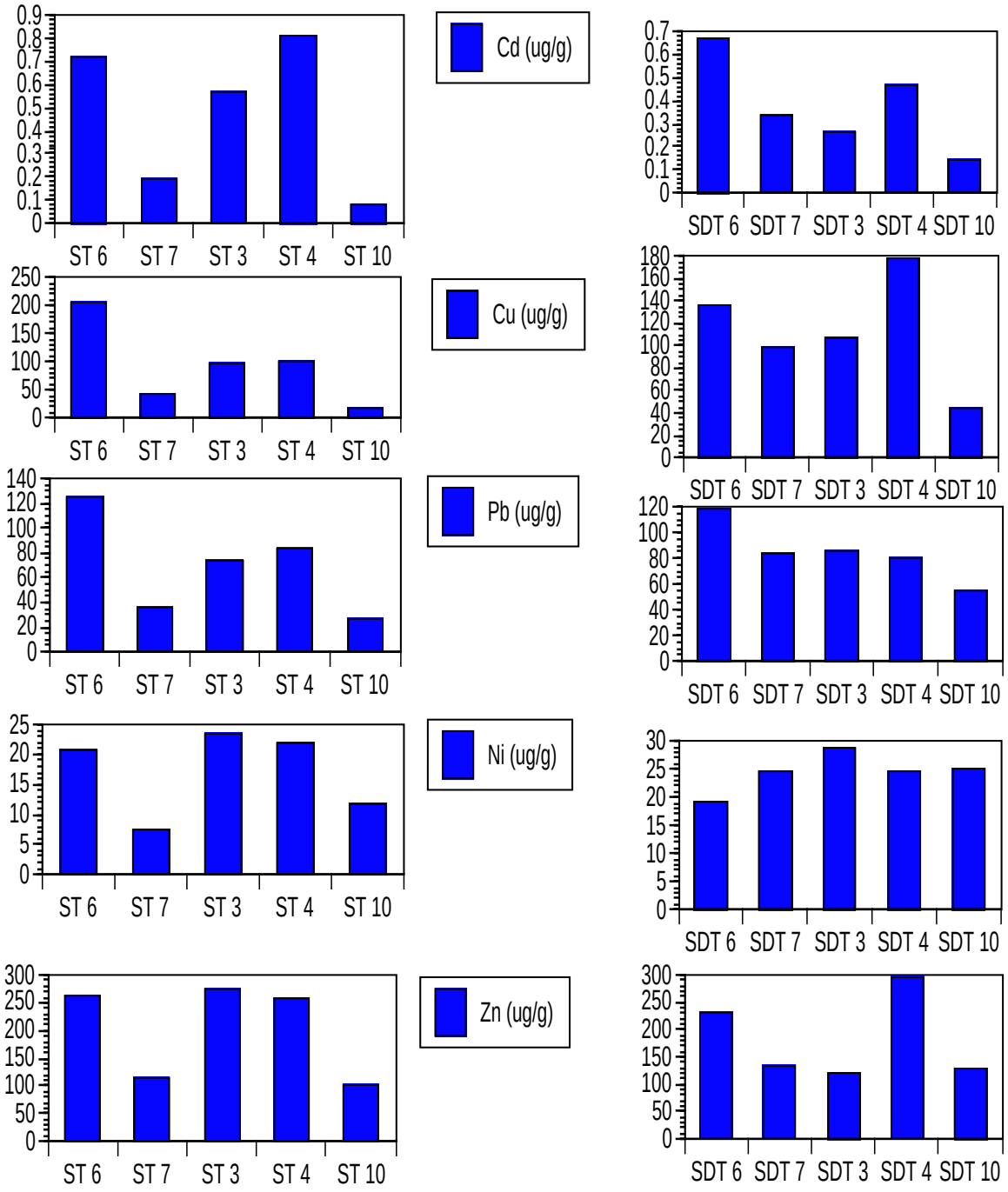

Figure 7. Anthropogenic concentrations of a possible flow pattern down the East Passage, near Prudence Island.

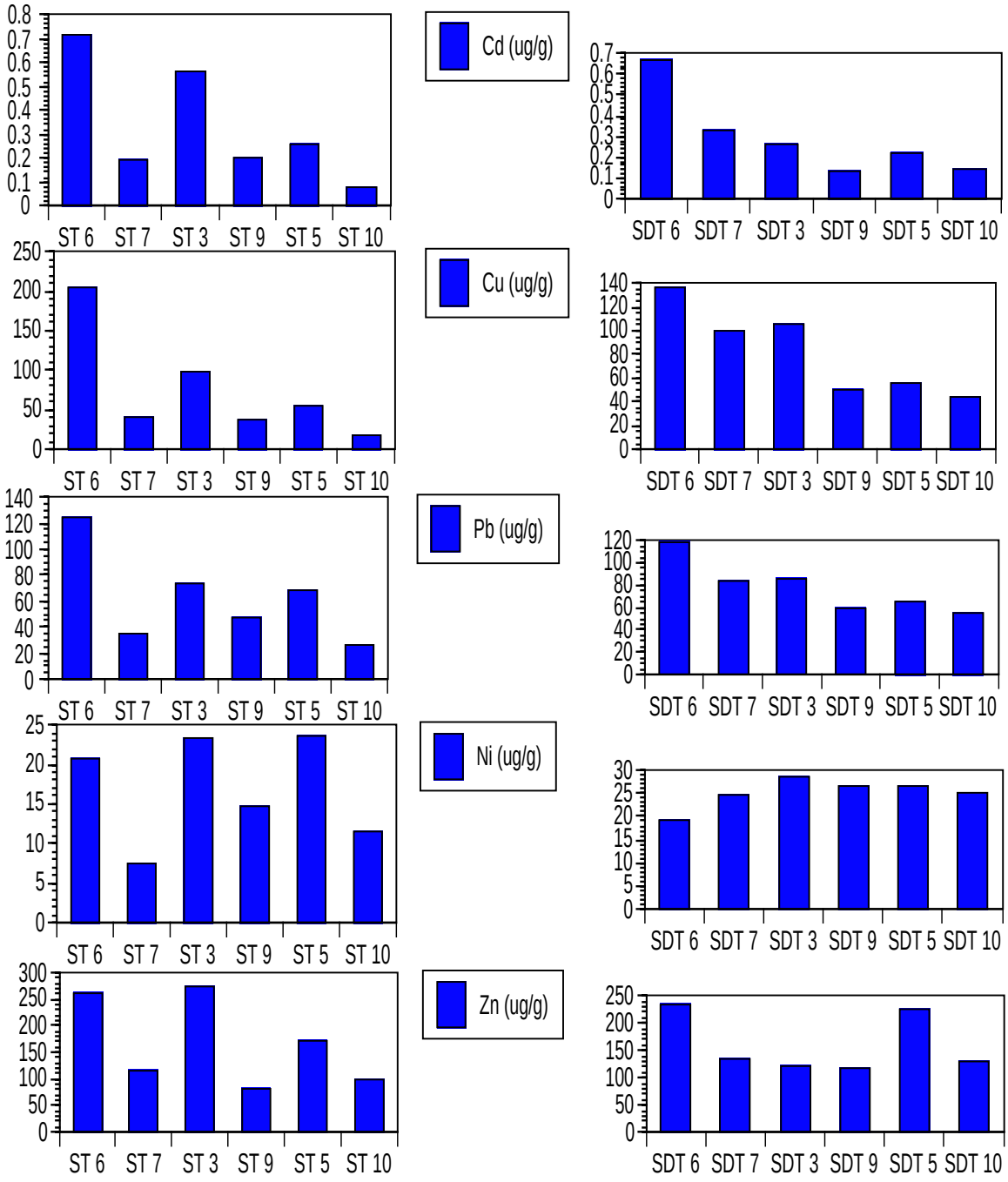

Figure 8. Anthropogenic concentrations of a possible flow pattern down the East Passage.

Table 4. Anthropogenic contaminant concentrations normalized to grain size.

	Cd	Cu	Pb	Ni	Zn
Station 1	0.08636364	8.36363636	13.5181818	2.47272727	12.1818182
Station 2	0.00485612	1.23141487	0.94364508	0.31690647	2.74580336
Station 3	0.00734112	1.26848249	0.94811933	0.30402075	3.56679637
Station 4	0.01114011	1.36950549	1.13598901	0.30247253	3.57142857
Station 5	0.00296928	0.63481229	0.77701934	0.26905575	1.95676906
Station 6	0.01534188	4.38034188	2.67094017	0.44444444	5.61965812
Station 7	0.00878378	1.83333333	1.61261261	0.33783784	5.22522523
Station 8	0.00485258	1.17936118	1.07739558	0.28378378	3.46437346
Staton 9	0.00413088	0.7791411	0.96114519	0.3006135	1.65644172
Station10	0.00430851	0.92553191	1.38297872	0.61895093	5.37234043
Station11	0.00208494	0.49420849	0.57786358	0.25353925	3.03732304
Sed. Trap 2	0.00257384	1.23734177	0.97362869	0.30801688	2.66877637
Sed. Trap 3	0.00279616	1.13127001	0.92102455	0.30629669	1.28068303
Sed. Trap 4	0.00523915	1.98220245	0.88431591	0.27586207	3.2814238
Sed. Trap 5	0.00220966	0.57965057	0.67831449	0.27338129	2.33299075
Sed. Trap 6	0.0081477	1.6440678	1.437046	0.23123487	2.82082324
Sed. Trap 7	0.00364333	1.08533917	0.92122538	0.27002188	1.46608315
Sed. Trap 8	0.00258621	0.86206897	0.77047414	0.29806034	2.88793103
Sed. Trap 9	0.00148315	0.55617978	0.67303371	0.29752809	1.3258427
Sed. Trap 10	0.00158798	0.48497854	0.58583691	0.26738197	1.37339056
Sed. Trap 11	0.00206154	0.48410256	0.50358974	0.25620513	2.07179487
Sed. Trap 2 dup	0.002827	1.19303797	0.92194093	0.31012658	2.08860759

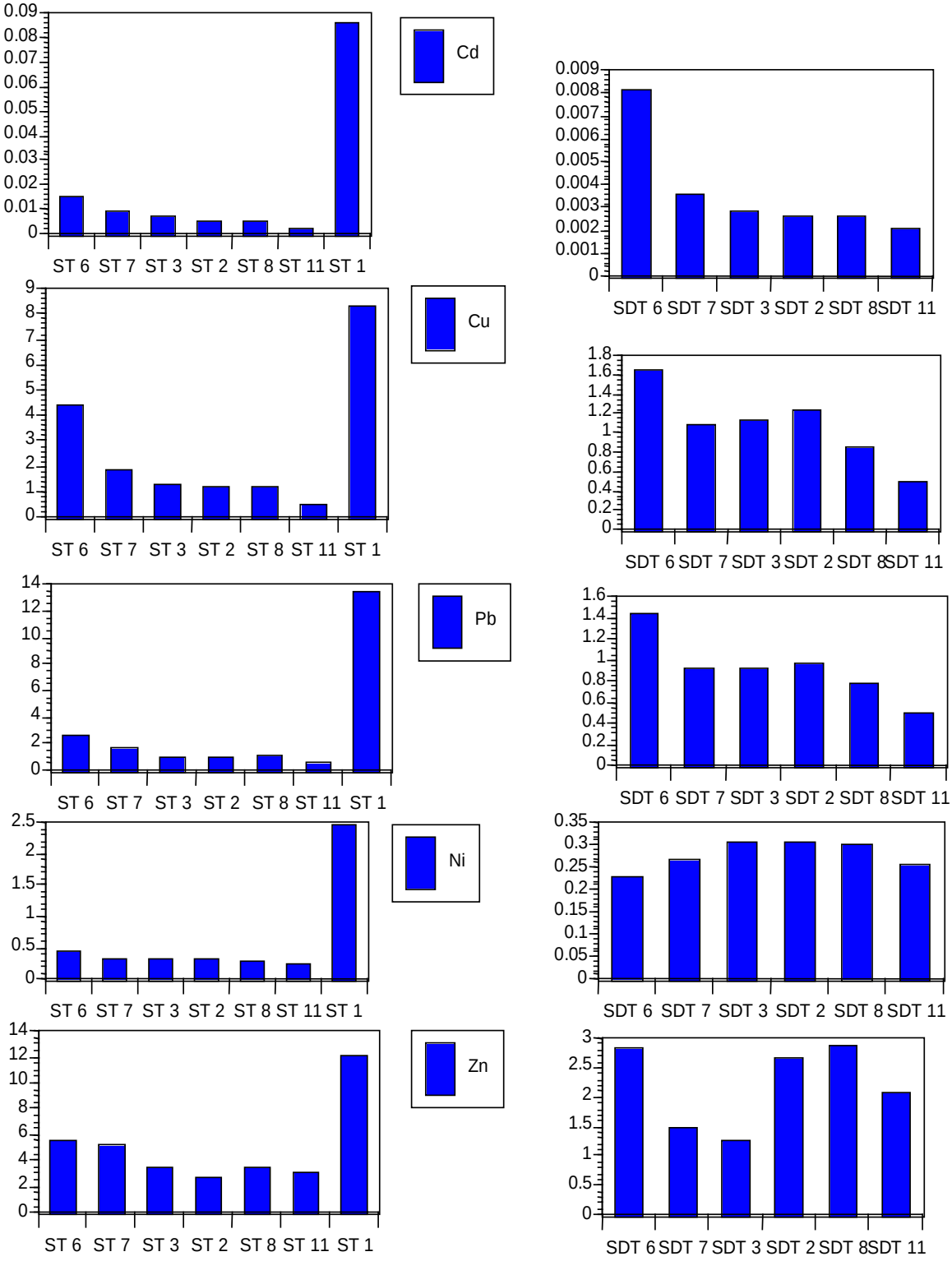

Figure 9. Normalized anthropogenic concentrations of a possible flow pattern down the West Passage.

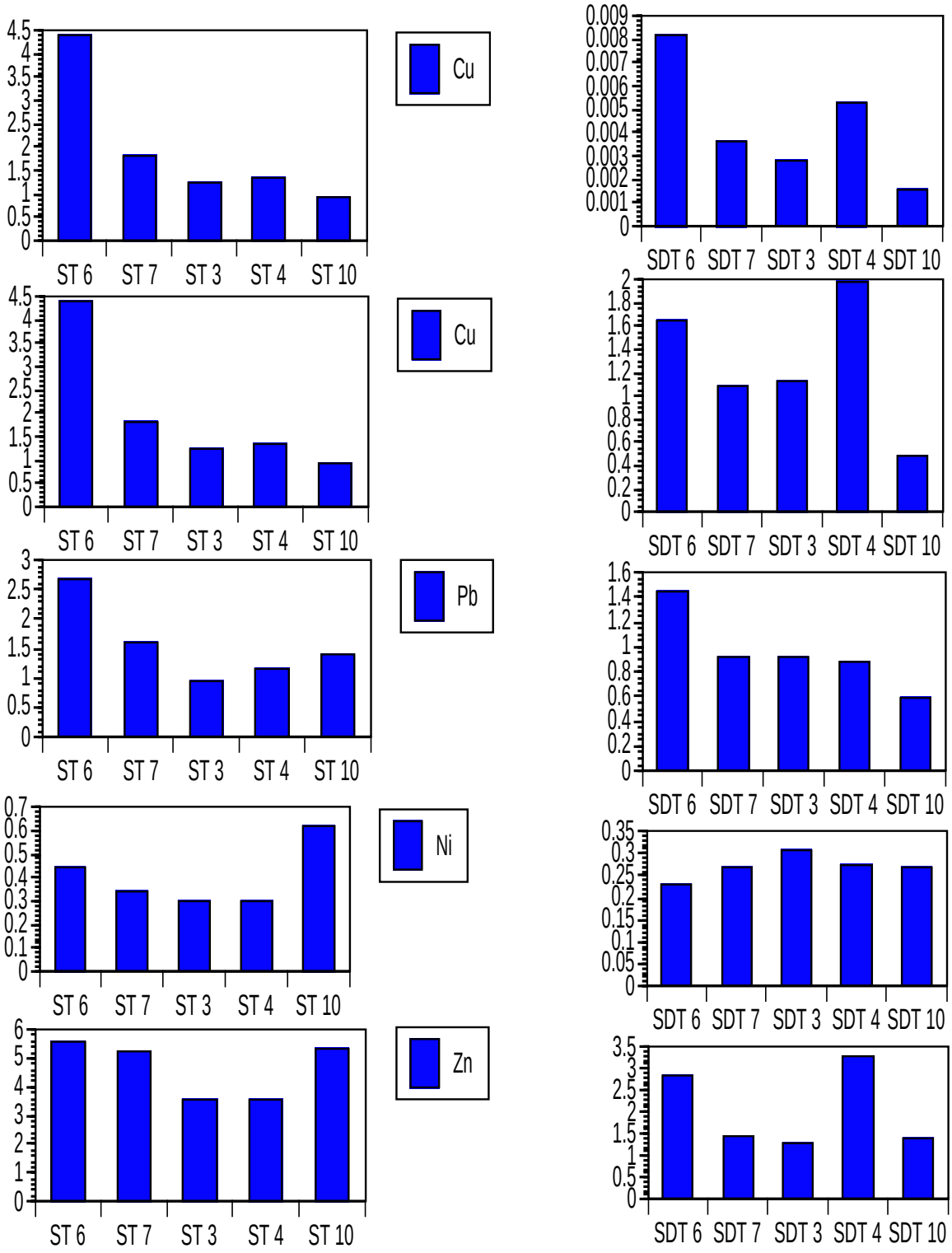

Figure 10. Nomalized anthropogenic concentrations of a possible flow pattern down the East Passage, near Prudence Island.

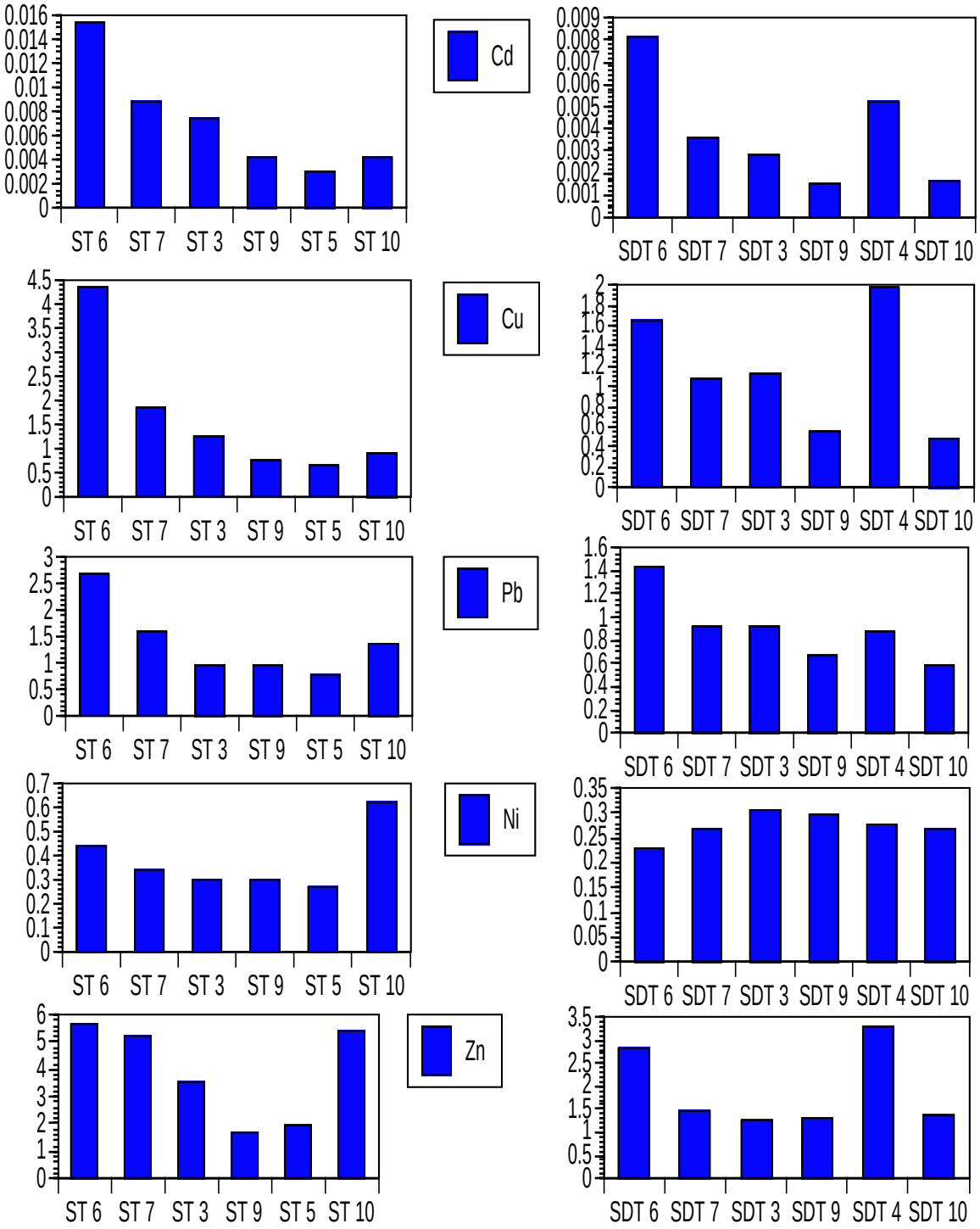

Figure 11. Normalized anthropogenic concentrations of a possible flow pattern down the East Passage.

Table 5. ERL and ERM guideline values for selected contaminants. (Long et al., 1995).

Chemical	Guidelines ERL		ERM
Cadmium	1.2		9.6
Copper	34		270
Lead	46.7		218
Nickel	20.9		51.6
Zinc	150		410

All concentrations are in ppm dry weight.

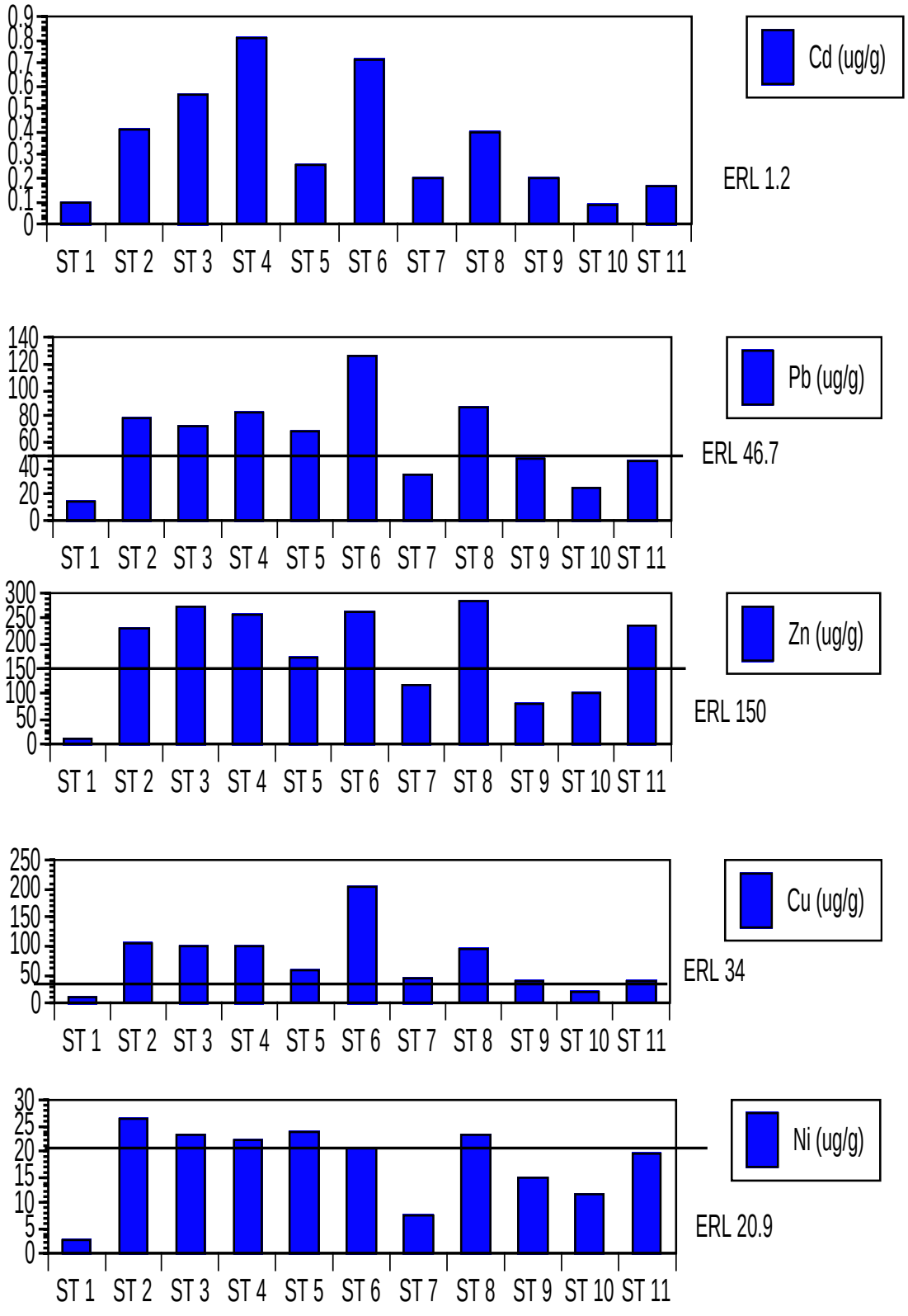

Figure 12. ERL for surface sediments

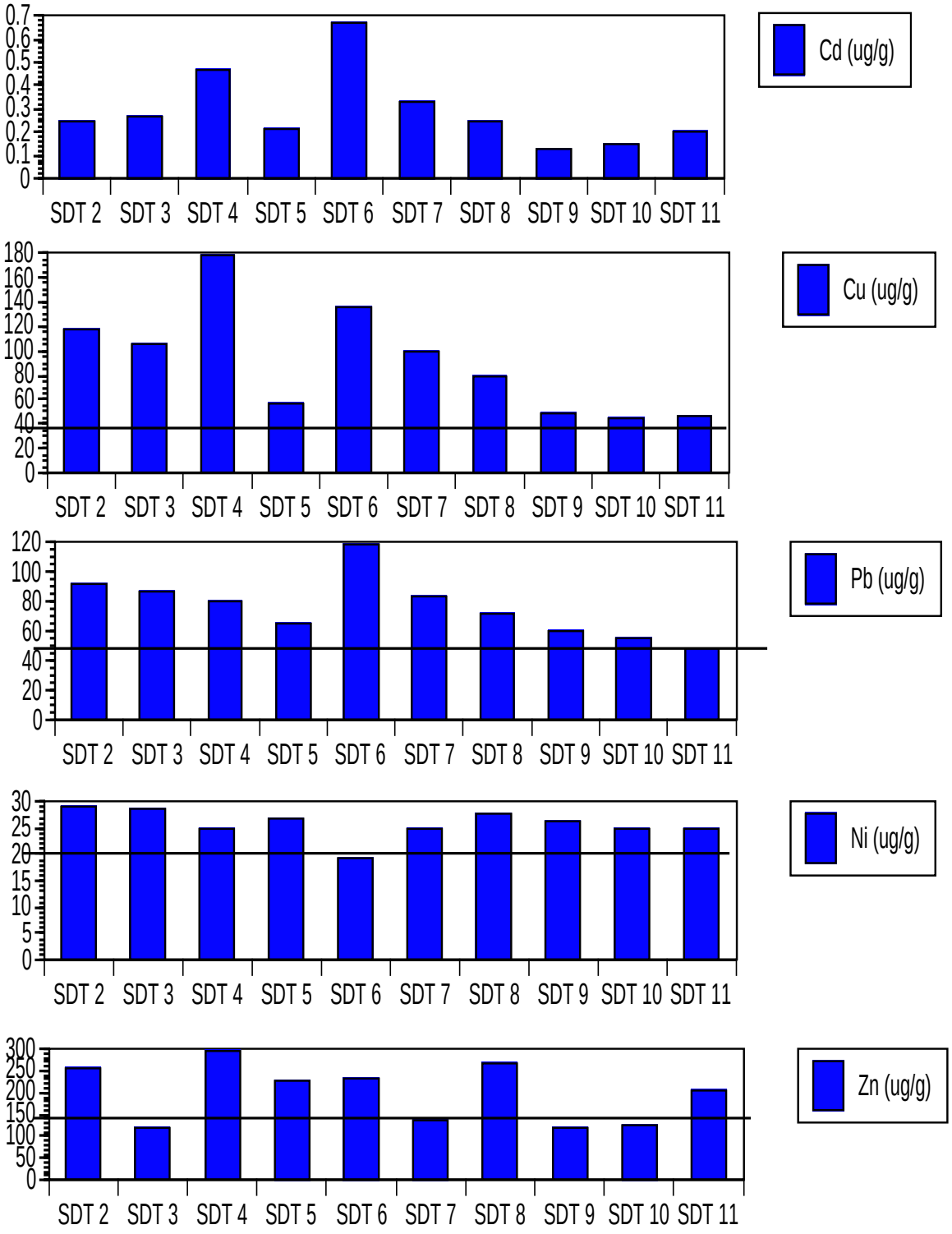

Figure 13. ERL for sediment traps.

Current Switching Within a Rotating Framework: A Gulf Stream Simulation

Jason Jarrell
Marshall University
West Virginia

Prepared for:
The Summer Undergraduate Research Fellowship in Oceanography

Advisors:
Dr. Thomas Rossby
Dr. Peter Cornillon

Graduate School of Oceanography
University of Rhode Island

August 2000

Abstract

In this paper, we wish to test by means of laboratory experiments on a rotating table a hypothesized current switching mechanism to explain the rapid warming at the end of the last glacial maximum about 15,000 yeas ago. The apparatus has a simplified structure of the North Atlantic bathymetry. The significance of the conjecture motivating the experiment depends on the suddenness of the switch from the paleo-Gulf Stream (during the glacial maximum) to that of the present Gulf Stream (post-last glacial maximum). This theory, introduced by T. Rossby, states the pGS was a zonal current heading eastward across the Atlantic south of the Grand Banks. The change to today's Gulf Stream resulted from both a slow shift northward of the pGS until contact with the Grand Banks was made and the response to a positive feedback system driven by deep convection in the area of the Nordic Seas.

To show this process in the lab, a 120° sector of a tank on a cyclonic rotating table is used. This sector contains three point 'sources', one positive source and two negative sinks. With the source along the western wall, a sink at the same radius on the eastern wall, and a sink at the apex, we wish to show the sudden shift in the current flow in this rotating sector. Initially the eastern sink is on while the apex sink is off, which leads to a zonal current across the tank. Once this zonal flow is evident, the eastern sink is halted, and the apex sink is activated. The new water from the source now takes the path of a new current headed directly toward the apex along the western wall. The time required for the new water to reach the apex sink is quite fast compared to the time needed to maintain the zonal flow (of the same magnitude as the number of days the theoretical switch-time predicts). This result, hence, gives support to Rossby's conjecture of a rapid change in the Gulf Stream that would then lead to a climate change in the North Atlantic and surrounding areas.

History of the Gulf Stream

The time period for the last glacial maximum (LGM) was over ~15,000 years ago. McIntyre's reconstruction of sea surface temperatures in the North Atlantic during the LGM (1976) gives evidence that the path of the pGS was zonal, heading toward and beyond the Azores off the northern coast of Africa (Fig. 1). As the LGM drew to an end nearly 14,600 years ago, it is surmised that the path of the pGS had nearly reached the Grand Banks through a slow migration northward. Another significant change in the paleo-Atlantic was the beginning or strengthening of a thermohaline circulation in the Nordic Seas. The turning on of the circulation was possible because of a steady increase of salinity in the North Atlantic (and Nordic Seas) caused by evaporation of its waters across North America and into the Pacific. The conjecture states that when the salinity reached a certain value, the highly saline waters became dense enough to sink to the deep ocean and flow out of the North Atlantic. The creation of this low pressure, or drop in sea level, resulted in the production of a Kelvin wave. Kelvin waves in general are permitted only to travel along lateral boundaries and, in the northern hemisphere, propagate with the boundary on the right with respect to the direction of travel for the wave (Cushman-Roisin, 1994). Since the wave traveled south, then the right side boundary was composed of the shallow Grand Banks and the fluid boundary of the Labrador Sea, due to its cyclonic circulation. When the wave reached the Grand Banks, the highly saline waters of the pGS traveled north along the same path as the Kelvin wave eventually reaching the low-pressure region of the Nordic Seas. Upon reaching the area of deep convection, the saline waters from the south sink to become part of the deep water which leaves the Nordic Seas along the western wall of Atlantic's ocean basin. This positive-feedback system thus locks into place and hence changes the pGS's path to today's Gulf Stream path (Fig. 2, Robinson et al. 1995).

Experimental Setup

The experimental apparatus consists of a 120° tank sector on a rotating table, several types of electronics to monitor and record the trials, and the pump system (Fig 3).

The sector has a radius of 50cm (Fig 4.) with a polar coordinate system diagram lying beneath the tank. Monitoring and recording of the experiment is done through the combination of a high-resolution digital still-camera and a digital camcorder mounted above the sector. By mounting the cameras directly to the rotating table and transmitting the signal to a remote television via an R/F transmitter, constant monitoring of the condition of each trial is possible. The digital still-pictures are taken with the aid of a remote control then downloaded to a computer where they can be analyzed.

The pump system used consists of a small 1.5-3V DC pump connected to the source and sinks making a (nearly) closed system. Both the source and sinks are made of stiff 3/8" tubing that runs down along the side of the tank. The sinks take in water through a series of small 1/16" holes drilled along a vertical line of the tube. As for the source, a thin foam is placed along a long slit cut down the front of the tube. This foam is then wrapped in cellophane and slit down the front allowing a line vertical line source for the incoming water. Dyed water is introduced into the tubing between the pump and source by means of a drip system (Fig. 3).

Specific placement of the source and sinks is necessary in order to roughly attempt to replicate the Atlantic's structure. The lone source is placed along the western wall of the sector and is meant to represent the inflow of upper ocean water into the North Atlantic. Similarly for the sinks, one is located along the eastern wall at the same radius as the source representing the eastern terminus of the pGS in the north Atlantic during the LGM while the other at the apex, is intended to simulate the sinking of water in the Nordic Seas.

Variations and Results

Slight variations in the experimental setup were needed as trials were run. Several parameters were altered in order to reduce variables within the sector. For the first trials, a well-defined current across the tank could not be formed. As shown in the experiments from Stommel et al. (1958), a zonal flow is the only possibility due to conservation of vorticity. Vorticity conservation states that if a rotating water column moves toward the apex ($-\Delta\rho$ radius), it inherently must either decrease its relative vorticity or increase the

column height (Knauss, 1978). The relationship for the water height as a function of radius, where C is the height of the apex, is given by the following equation.

$$H(r) = \frac{\omega 2 * r2}{2g} + C \qquad \text{(Eq.1)}$$

With Eq.1, it becomes clear that a change in water height in fact cannot compensate for a change in radius, since that would require to column to either increase height and decrease radius or vice versa.

As the trials continued, two additional parameters from the Stommel experiments were needed. Initially the outer radius water height in the sector is approximately 20cm. With a constant angular velocity of 0.5 π sec-1, a height difference from inner radius to outer radius for all trials is approximately 3.15cm. With the 20cm initial outer height, a ratio of inner height to outer height was close to 17:20, while the Stommel trials used a ratio of 1:2 (Stommel et al. (1958). Another parameter used by Stommel was to cover the tank as to prevent wind stress and the presence of an Ekman layer. By covering our tank and only filling for a height ratio of 2:1 (~3.14cm inner radius, ~6.28cm outer radius), we were able to form what appeared to be a zonal current that takes nearly 1-2 hours (~900-1800 rotations) to reach the eastern sink. Upon investigating the data taken from this current, the velocity of the current as a function of radius could be calculated (Fig. 5). A correlation exists between the peak of the graph at 37.5cm and the placement of the source and sink at 37.5cm. This gives support that the flow across the tank is zonal (Fig. 6).

Once this zonal current is present, the switching of sinks is possible. When the switch occurs and a small scale Kelvin wave travels out the western wall, the source water begins to almost immediately to travel northward along the wall. Unlike the slow moving zonal current, the western wall current reaches the apex in less than 10 minutes (~ 150 rotations) (Fig. 6), showing that the pressure wave associated with this Kelvin wave takes place too fast to be observable. This rapid experimental switch and traveling pressure wave lend support to Rossby's idea, that a rapid change northward of the pGS took place at the end of the LGM.

Future Work

The most recognizable addition to the apparatus for a future experiment would be that of a "continent piece" or some other changes in the bathymetry of the sector. The "continent piece" would be located along the western wall near the apex and represent a physical boundary in the Atlantic, the Grand Banks. We would hope to see another rapid switch in direction of the current flow. The location of the new current northward would theoretically run along the western wall, then along the edge of the continent, soon reaching the apex. Any other bathymetric changes to make the sector better resemble the paleo-Atlantic would be beneficial.

Acknowledgements

I would like to extend my gratitude and appreciation for working with Drs. T. Rossby and P. Cornillon of the University of Rhode Island. Their encouragement and guidance aided me through the experiment.

REFERENCES:

Cushman-Roisin, Benoit, 1994. Introduction to Geophysical Fluid Dynamics. Prentice Hall; New Jersey.

Knauss, John A., 1978. Vorticity and Western Boundary Currents: The Gulf Stream. Introduction to Physical Oceanography. Prentice-Hall; New Jersey. 131-135.

McIntyre, A., N. G. Kipp, A. W. H. Be, T. Crowley, T. Kellog, J. V. Gardner, W. Prell, and W. F. Ruddiman, 1976. Glacial North Atlantic 18,000 years ago: A ALIMAP reconstruction. Mem. Geol. Soc. Am., 145, 43-76.

Robinson, S. G., M. S. Maslin and I. N. McCave, 1995. Magnetic susceptibility variations in Upper Pleistocene deep-sea sediments of the NE Atlantic: Implications for ice rafting and paleocirculation at the last glacial maximum. Paleoceanogr., 10, 221-250.

Stommel, H., 1958. Some Examples of Stationary Planetary Flow Patterns in Bounded Basins. Collected Works of Henry M. Stommel, II, 346-354.

T. Rossby, 2000. Current Switching as a Mechanism for Rapid Climate Change.

Figure 1

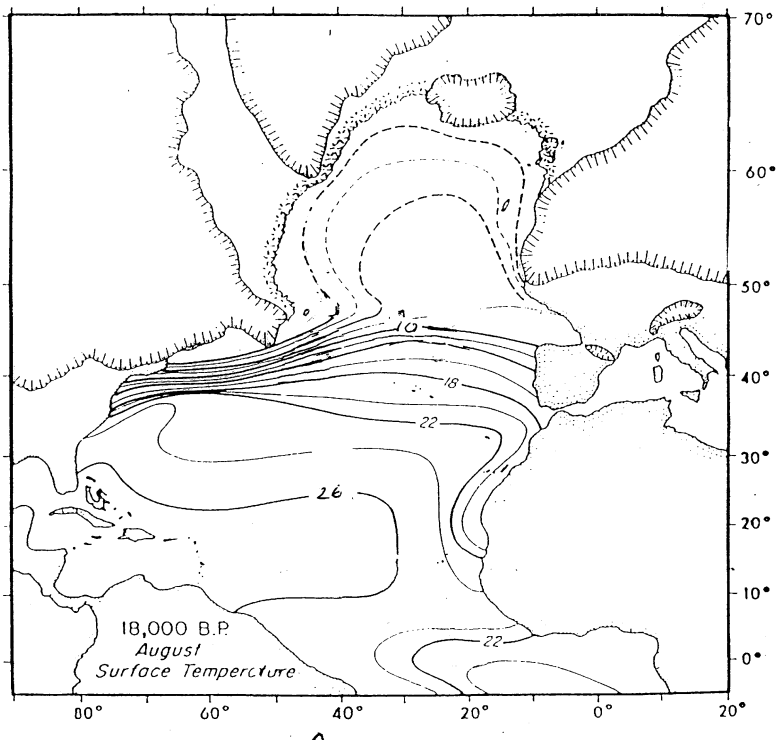

Sea surface temperature 18,000 years B.P. (McIntyre, al., 1976).

Figure 2

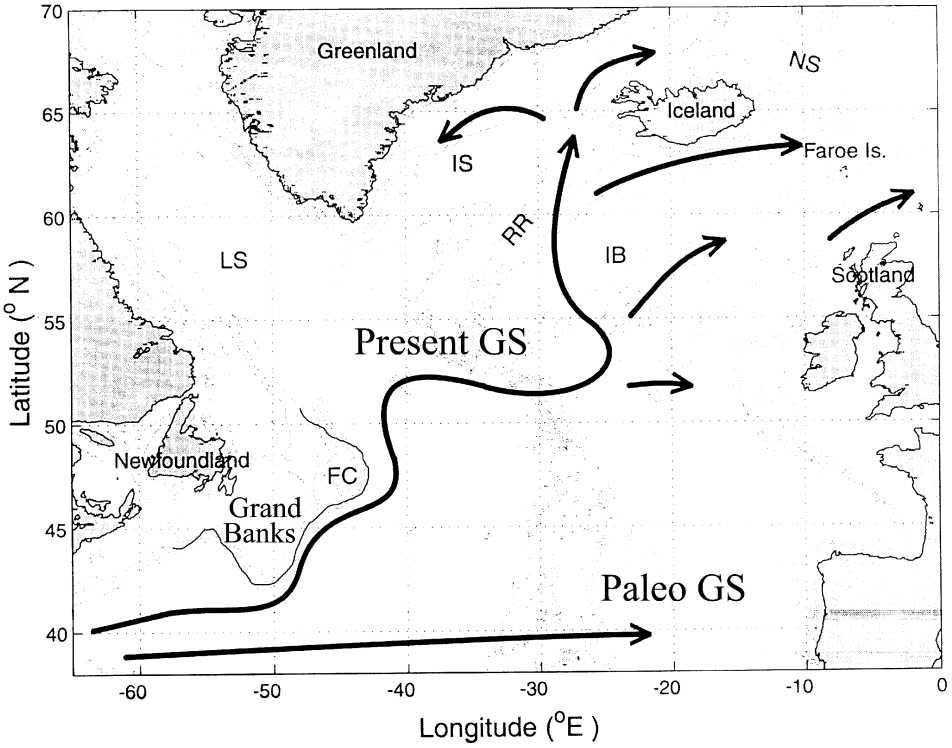

Figure 3

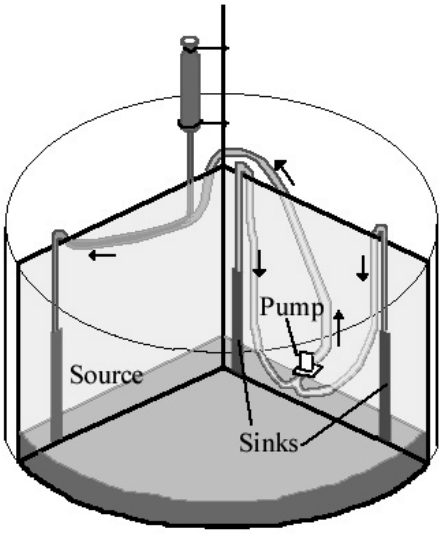

Figure 4

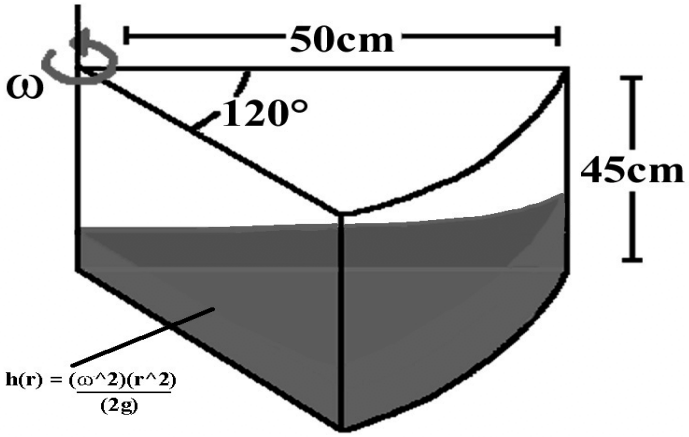

Figure 5

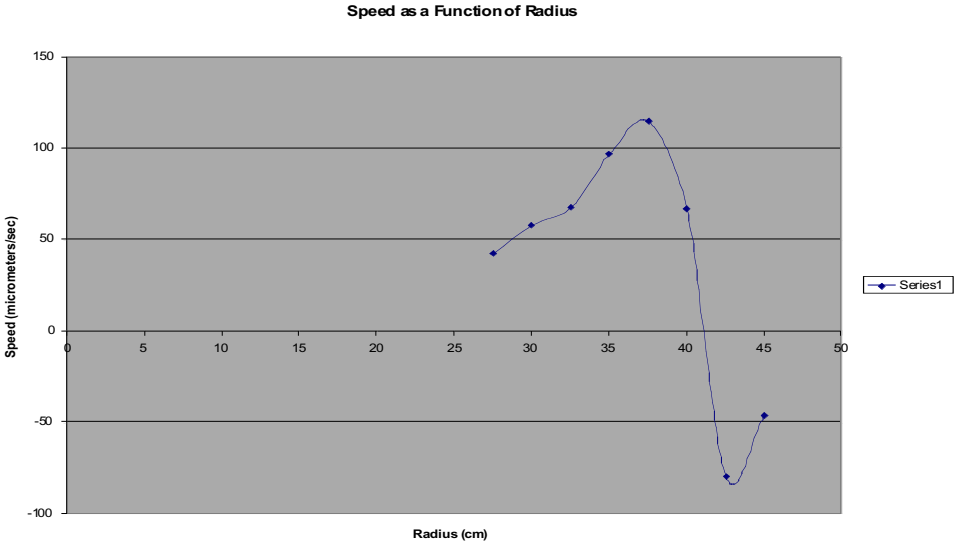

Figure 6

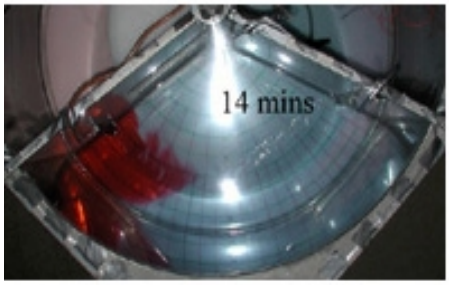
14 mins

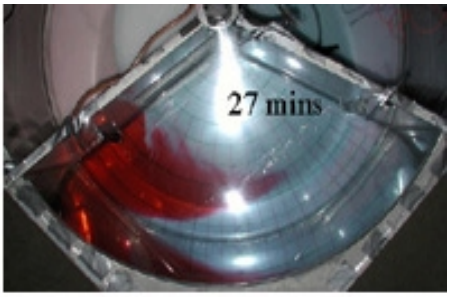
27 mins

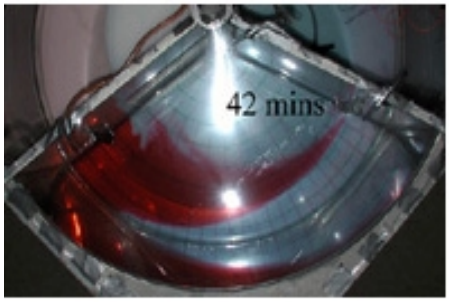
42 mins

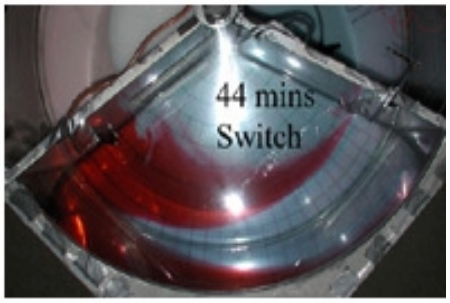
44 mins
Switch

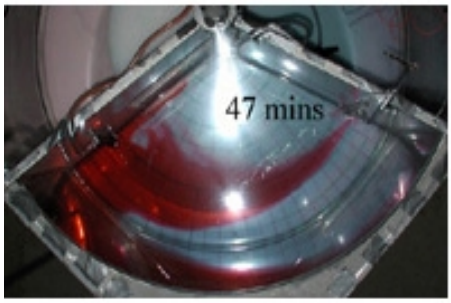
47 mins

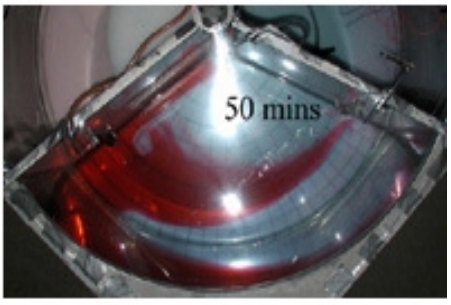
50 mins

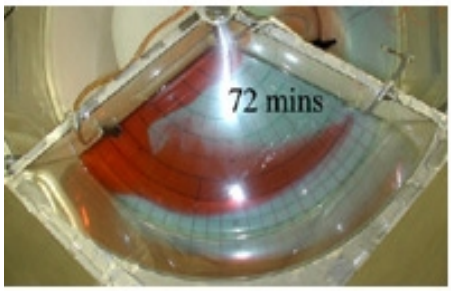
72 mins

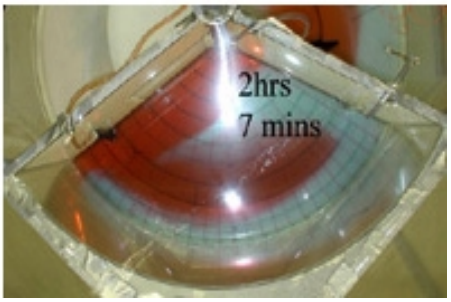
2hrs
7 mins

^{234}Th-derived particle organic carbon flux in the Labrador Sea: significance of carbon-thorium relationship with size

Jennifer E. Szlosek
Massachusetts Institute of Technology

Prepared for:
The Summer Undergraduate Research Fellowship in Oceanography

Advisors:
Brad Moran
Sarah Weinstein
Patrick Kelly

Graduate School of Oceanography
University of Rhode Island

August 2000

ABSTRACT

Measurements of $^{234}Th/^{238}U$ disequilibrium and the $POC/^{234}Th$ ratio of sinking particulate matter in the upper ocean are increasingly being used in oceanographic field programs to estimate the downward flux of particulate organic carbon (POC) from the euphotic zone. It is clear that the $POC/^{234}Th$ ratio of marine particles can vary significantly in space and time due to changes in biological productivity, particle export and particle size distribution. Developing a quantitative understanding of the processes controlling the variability in $POC/^{234}Th$ ratios of marine particles is essential for validating the use of ^{234}Th to estimate POC fluxes from the surface ocean. Here we report water column measurements of $POC/^{234}Th$ ratios in three particle size-classes (1-10 μm, 10-53 μm, and >53 μm) from four stations occupied in the Labrador Sea, July 1999. Samples were collected for determination of dissolved and particulate ^{234}Th activity and POC concentration using large-volume in-situ pumps and Go-flo bottles. Results indicate: 1) $^{234}Th/^{238}U$ disequilibrium at all locations, and; 2) a decrease in the $POC/^{234}Th$ ratio with increasing particle size and, for the intermediate and large-size fractions, with depth. Variability in the $POC/^{234}Th$ ratio with particle size is consistent with simulations derived using a physical adsorption-aggregation model of Burd et al. (2000). ^{234}Th-derived POC export fluxes for the intermediate and large particle size-fractions are similar in magnitude, on the order of 3.2 – 32 mmol C m^{-2} d^{-2}. The implication is that intermediate size particles (10-53 μm) contribute significantly to the total POC flux, which would have been underestimated by calculations based on the large particle size-class (>53 μm) $POC/^{234}Th$ ratio.

INTRODUCTION

A greater understanding of the dynamics of the vertical flux of carbon in the ocean is needed to accurately estimate the magnitude of carbon sequestered in the ocean. ^{234}Th-derived carbon fluxes can be used to calculate the flux of particulate carbon from the surface waters of the ocean. Particulate organic carbon that sinks out of the upper level of the ocean is dependent on seasonal and geographical location in some of the Earth's regions (Rutgers van der Loeff et al., 1997) and on the size distribution of the particles (Burd et al., 2000). Thus, using a POC/^{234}Th ratio that represents the majority of the mass flux out of the euphotic zone (depth with 1% of the light level at the surface) is necessary to accurately calculate the particulate organic carbon flux out of the ocean's surface. A quantitative understanding of the POC/^{234}Th ratio and how it varies with particle size distribution, depth in the water column, and latitude of the globe are needed to properly constrain the ^{234}Th –derived carbon export flux. In this paper, the relationship of POC/324Th ratio with particle size and water depth will be discussed.

Thorium-234, a particle-reactive radio-isotope, is a useful tracer of particle export on short time scales of days to months ($t_{1/2}$=24.1 d), (Coale and Bruland, 1985). ^{234}Th is created continuously by the alpha decay of ^{238}U and would remain in secular equilibrium with ^{238}U if there were no particles in the water. The disequilibrium occurs between ^{234}Th and ^{238}U because the ^{234}Th atom is rapidly hydrolised and passively adsorped to surface sites of particles. This process of adsorption is referred to as "scavenging". (Bruland and Coale, 1986) This disequilibrium is used to determine the thorium flux out of the upper ocean waters by the following equation:

$$P_{Th} = \lambda_{Th} \int_{z_2}^{z_1} \left(A_U - A_{Th} \right) dz \qquad (1)$$

where P_{Th} is the overall removal of flux of particles, λ_{Th} is the decay constant of ^{234}Th (0.0288 d^{-1}), A_U is the activity of ^{238}U, and $A_{Th,T}$ is the total activity for ^{234}Th. Using the equivalent ratios of measured particulate ^{234}Th to measured POC and the ^{234}Th derived particle flux to the unknown POC export flux. The carbon export flux is found by the equation by using the equation:

$$P_{POC} = \frac{POC}{^{234}Th} P_{Th} \qquad (2)$$

where P_{POC} is the export flux of particulate organic carbon, POC is the measured particulate organic carbon, and P_{Th} is the overall removal of flux of particles calculated in equation 1.

The continuum of particle size distribution in the ocean is represented by a decrease in particle abundance with increasing particle size. Despite this relationship, ^{234}Th-derived carbon flux calculations traditionally used the operationally defined size fraction of >53 μm to account for the whole size distribution of the particle fall out (Cochran et al., 1993). Ocean field studies that have measured POC and particulate ^{234}Th of different size fractions have been limited. Moran et al., (1993) found that the magnitude of POC/^{234}Th ratios decreased with particle size. A coupled adsorption-aggregation model developed by Burd et al. (2000) reproduced observations of inverse relationship of the ratio with particle size. To this point there have not been *in-situ* measurements of the POC/^{234}Th ratio on several size fractions to compare with the model's results.

The purpose of this paper is to investigate the possible dependence the POC/^{234}Th ratio has on particle size by analyzing water column measurements of POC/^{234}Th ratios from 3 size fractions: a small particle size-class (1-10 μm), an intermediate size-class (10-53 μm), and a large particle size-class (>53 μm) collected at four stations in the Labrador Sea (Fig. 1). Although the Labrador Sea is proposed to be a prominent area of carbon flux (Tans et al., 1990) there have been few carbon flux studies done. This investigation took place in July 1999, near the end of the spring bloom period for the Labrador Sea. Over all, the results indicate ^{234}Th/^{238}U disequilibrium along the tract, suggesting particle export occurs on short time scales in the upper waters. These data provide evidence that there is a decrease in the POC/^{234}Th ratio with particle size as predicted in the combined model of Burd et al. (2000). The results are used to calculate carbon export fluxes and export ratios (e-ratios) for the different size fractions to see how they compare to the generally excepted flux determined by the POC/^{234}Th ratio of the >53 μm fraction.

METHODS

The work done during this Summer 2000 NSF/REU program involved data analysis of the low-level-beta-counting of the intermediate and large size-classes, determination of ^{234}Th derived particle flux, POC/^{234}Th ratios, POC export flux, and export ratios of all size fractions for the 4 stations indicate in Figure 1. Work done previous to that accomplished by the NSF/REU project are included in the following sections *Sample collection and processing*, *^{234}Th analysis*, and *Particlute organic carbon analysis*.

Sample Collection and Processing

Water samples were collected at four stations along the AR7W line between 55°N, 54°W and 60°N, 49°W in the Labrador Sea in July 1999, on board the Hudson (Fig. 1). Large volume *in-situ* pumps were used to collect samples (200-600 L) sequentially through a series of 5 filters (53 μm, 142 mm diameter, Nitex screen, 10 μm Nitex screen, 1μm pre-filter, and 2 MnO_2-impregnated adsorber cartridges) at five depths (1, 25, 50, 100, 250 m). The smallest fraction of POC was collected via filtration through a 25 mm diameter, 0.7 μm GF/F filter from water collected in Go-Flo bottles due to high loading of the in-situ filter system. The 142 mm Nitex filters were sonicated in filtered seawater and the particles collected on a 25 mm GF/F filter, which was dried at 60°C and stored in petri dishes to be analyzed for ^{234}Th activity and POC/PON. POC and PON analysis were performed on subsamples cut from the 25 mm GF/F filters at the shore-based URI lab and the remaining subsamples were sent to Bedford Institute of Oceanography (BIO) for thorium analysis. The MnO_2-impregnated adsorber cartridges were used to collect dissolved ^{234}Th. The MnO_2 cartridges and 1 μm pre-filter were dried at 60°C in an oven, and then ashed.

^{234}TH Analysis

The activity of the dissolved ^{234}Th and 1-10 μm particle size-class were determined by gamma spectrometry at URI. The ^{234}Th activity of the MnO_2 cartridges and 1 μm pre-filter were counted on a planar Ge detector (2000 mm^2) using the 63.3 keV peak for calculations (Buesseler et al., 1992; Moran et al., 1997; Charette and Moran, 1999). Calibration of the gamma detector for ^{234}Th analysis was done at the correct geometries using the NIST ^{238}U. Decay correction of the samples was made to the mid-point of sample collection. Uncertainties for ^{234}Th were

determined by using a 1σ counting error. The dissolved ^{234}Th activities were corrected for the collection efficiency (E) of the MnO_2 adsorber cartridges by the formula, E = 1 – MnB/MnA, where MnA and MnB are defined to be the ^{234}Th activities of their respective cartridges. The activities of the intermediate and large size-classes were determined by low-level-beta-counting using the subsamples that were sent to BIO. Activities were decay-corrected using the program Sigma Plot described later. To determine the ^{234}Th/^{238}U disequilibrium ^{238}U activities needed to be calculated from salinity measurements. A ^{238}U activity profile was determined from the equation $^{238}U = 0.07081 \times S$ (Chen et al., 1986), using the salinity data at CTD collection depths closest to the *in-situ* filtration depths (i.e. 1, 25, 50, 100, 250 m).

Particulate Organic Carbon Analysis

The cut subsamples (~15-20% of the filter's total weight) were thawed and acidified to remove particulate inorganic carbon using fuming reagent grade 12 M HCl in a desiccator for 24 hr. After which, they were put in an oven to be dried at 60°C. POC concentration of the subsamples were determined using a Carlo-Erba CHN analyzer (Pike and Moran, 1997). To determine the concentration of particulate carbon, the filter blank POC concentration value was subtracted from the total mass of carbon. This difference was then converted to molar units and then divided by volume of water filtered (resulting in units of _mol L^{-1}).

Sigma Plot

The program Sigma Plot was used to access each sample's fit to a computer-generated ^{234}Th decay curve. Every intermediate and large sized sample underwent beta counting at four consecutive times with approximately month-long intervals between each counting. Raw counts per minute (cpm) were calculated by dividing the gross counts by the respective time interval (determined by using the midpoint of time taken for sample collection and the midpoint of time taken for samples to be counted). The gross counts, cpm, and time interval data were entered into a spreadsheet of Sigma Plot. Based on this information, the sigma plot program produces a decay curve of ^{234}Th and represents the entered data as points in the plot area. This program design allows the operator to remove outliers. Data that fall far from the decay curve or that have large error bars would be the likely candidates to be removed. In this study there was high correlation to the decay curve for all of the samples, but one. Hence, no data points were thrown

out. The one exception had its decay curve in an inverse arrangement and is from station 9 at 1 m in the >53 μm size fraction. This example along with the >53 μm particle size-class sample at station 13 and 25 m had negative ^{234}Th activities generated by Sigma Plot and were not used in this study because they had high error and are considered to have counts near the detector's limit. Another sample with high error is from station 18 at 100 m and of the large size-class.

Calculation of ^{234}Th Activity

The activity of ^{234}Th, in units of disintegrations per minute per liter (dpm L^{-1}), was calculated by taking the difference of raw counts per minute and background counts per minute over the multiplication of the efficiency of the detector and the volume of water pumped. Raw cpm values were calculated by the method explained in the previous section and volume of water pumped was read off a flow meter used at sea. A Th/U standard 10 included in each run on the beta counter was used to determine the detector's efficiency. There are 5 detectors used during each run so the average efficiency was calculated for each detector and applied to the samples run on that detector. Two approaches to determining the background counts per minute were compared and found nearly equivalent. The "b" values are the counts per minute of the sample determined by Sigma Plot extrapolating the activity of the decay curve as time goes to infinity. Filter blanks were beta counted during every run to test the background counts of each detector. The sigma plot generated "b" values were plotted against the average counts per minute of the filter calculated for each detector (Fig. 2). The plot comparing the two background cpm values was found to be linear and both methods were determined to be adequate. However, the average filter blank values were chosen to represent the background counts per minute for the calculation of ^{234}Th activity.

RESULTS AND DISCUSSION

Hydrography

Salinity, temperature and nutrient data revealed a difference in the general hydrography of station 25 with the other stations. Hydrography information was taken off of conductivity, temperature and depth (CTD) data provided by Glen Harrison of BIO. CTD readings were not

collected at the exact depths where water was filtered so profiles were plotted using values from depths closest to those at which POC and Thorium data were sampled. These plots with data from the four stations are found on Figure 3. A pycnocline is noticeable between 50 and 100 meters. In comparison with stations 9, 13, and 18 the surface waters of station 25 are notably cool and non-saline which is most likely a result of its close proximity to the southern tip of Greenland (see Figure 1) where fresher cold water enters the basin.

Primary Productivity

New production was estimated using the ^{13}C primary productivity values based on water samples placed in deck boxes for approximately 3 to 4 hour incubation periods. Depths at which productivity values were tested were dictated by the incubator screens and not the depth of the corresponding POC and Thorium measurements. Primary production (PP) values (mmol C m^{-3} d^{-1}) taken at levels closest to where the *in-situ* filtration occurred are included in Figure 4. The production rates near the surface ranged from approximately 1 to 2.75 mmol C m^{-3} d^{-1}. Stations 9, 13, and 18 have values that were grouped together with surface production levels ranging from 2.35 to 2.75 mmol C m^{-3} d^{-1} that decrease rather linearly to near zero production between 44 and 64 meters. These stations are located in the deeper portion of the Labrador Sea Basin whereas station 25 approaches the shelf (see Fig. 1). Station 25 has a low surface production rate of 1 mmol C m^{-3} d^{-1}, a subsurface maximum production near 20 meters, and a deep penetration of production that terminates at 76 m. In this study the lower bound of primary productivity is used to indicate the euphotic level at which biological activity is light limited. The depths 44, 50, 63, and 76 meters were the levels that calculations of POC export flux out the upper water column were considered for stations 9, 13, 18, and 25, respectively.

Thorium Deficit

The ^{234}Th depleted upper waters are evidence of marine particle sinking out of the euphotic zone. Figure 5 shows individual station and mean station activities for both total particulate ^{234}Th and total ^{234}Th activities (dpm L^{-1}) with the station average of ^{238}U activity. The individual station values of dissolved, total particulate, and total ^{234}Th activity, ^{238}U activity and Th/U ratio values are shown in Table 1. The mean thorium deficit occurs between the surface and 100 meters. The ^{234}Th-derived particle flux for each station is determined from these activities by the

equation 1, where the depth of integration is dependent on the depth of the euphotic zone (i.e., where PP goes to zero).

The difference between the integrated uranium and thorium activities revealed that not all stations have a thorium deficit. The values of dissolved thorium at station 13 and 25 at 25 m were exceptionally high. At this depth the thorium activity exceeds that of uranium. The value of dissolved thorium activity at station 25 at 25 m was 5.34 ± 0.74 dpm L^{-1} and the total thorium activity was approximately 200% of that of uranium. This station's total thorium activity value was cast out because the error of the dissolved (<1 μm) thorium activity was greater than 100% and the because it is unlikely for remineralization allowing for such high ^{234}Th activity to occur at a depth of only 25 meters. The dissolved thorium activity of station 13 at 25 m was also high. It had a Th/U activity ratio of 1.3 ± 0.365. This point is included in the data set because there isn't a significant reason to dismiss it. The resulting Th deficit is 0.348 dpm L^{-1}. The high value of dissolved ^{234}Th activity may be due to advection or an absence or termination of the spring bloom production, but that cannot be determined from this data.

Particulate Organic Carbon

Water column measurements of particulate organic carbon for the 3 size fractions are in Figure 6a. The general trend for all particle sizes indicates POC content decreases with depth. This is expected based on light-limited carbon production that occurs via biological activity. There were higher levels of POC concentration in the smallest size fraction and comparable levels for the intermediate and large particle size-classes. A standard error of 5% was used for the 10-53 μm and the >53 μm fractions because of the large variability within the filter blank magnitudes (range of 0.695 to 14.811). High POC was found for station 13 at 1 m in the >53 μm fraction. There was also uncertainty in the POC measurement used for stations 9 and 25 at 25 m for greater than >53 μm and 10-53 μm size-classes respectively. This was due to the total weight of the wedge of the filter being analyzed not being recorded and instead the percentage of the total weight was estimated.

Go-Flo bottles with 0.7 μm GF/F filters that were used to collect the smallest size fraction because of high loading. Two inconsistencies with the rest of the data exist as a result, but are considered negligible in calculations of ^{234}Th-derived carbon export flux. These are the bottles were not tripped at the exact same depths of the in-situ filtration system, but nearly the same

depths and the smallest size fraction doesn't coincide with that of the 1-10 μm fraction of ^{234}Th, but is 0.3 μm larger. The POC concentration of the 0.7 to 10 μm size interval was determined by subtraction of the sum of the values for the 10-53 μm size-class and the >53 μm size-class from the >0.7 μm data provided by the analysis of the Go-Flo bottles done by Glen Harrison. Error for the small fraction was tabulated by taking the root of the addition of the squared error values of each individual size-class. POC measurements and errors of the water column for each station and size interval are listed on Table 2.

^{234}Th Activity

Thorium activity profiles (dpm L^{-1} vs. depth in meters) for individual stations and the station averages are plotted for each size fraction in Figure 6b. The ^{234}Th activity of the small size fraction is considerably larger than that for the intermediate sizes fraction (by 5 to 6% respectively). The station average profile of Fig. 6b shows that thorium activity, like POC content, decreases with depth. This decrease with depth intensifies after 100 m. This may imply that less aggregation is occurring below this level due to the decrease in net production of marine biogenic particles between 50 and 100 m where light limitation becomes a factor. The station mean ^{234}Th profile reveals every size fraction has a subsurface maximum of thorium activity. In both 1-10 μm and >53 μm fractions the peak is at 25 m, but for the 10-53 μm fraction it takes place lower, at 50 m. This prominent feature of a subsurface maximum implies that the large amount of thorium is because of an increase in particles available for ^{234}Th to react with at these particular depths. A cause for more particles at these depths may be an increase in primary productivity. We do not have chlorophyll count data to certify that possibility, but the nutrient data doesn't have a strong peak near those depths as one might expect to be seen to support such an increase in net production. Thus, another process may be the cause of this subsurface maximum. A possibility is that more particles may be entrained in the water column at that depth due to advection, coagulation and adsorption processes.

The 63.3 keV peak used by the gamma detector to determine the activities of the 1-10 μm fraction was difficult to distinguish against the background values and thus some values of Th activity for this fraction have high error (100% and greater) due to counting statistics. The activity at station 25 at 50 m was not even considered for high error (~129% and 200% in the POC/^{234}Th ratio calculation). Also observed was more scatter in the data of the intermediate and

large particle size-classes as expected, granted the rarer appearance of activity at this particle size. Activity for the 10-53 μm fraction gradually decreases, but it doesn't appear to approach a constant value. This may imply that more aggregation may be occurring below the euphotic level. A deeper profile would be needed to determine whether that might be the case.

POC/^{234}Th Ratio

POC/^{234}Th ratios (μmol dpm^{-1}) were calculated and plotted versus depth (Fig. 6c) and are listed with associated errors on Table 2. The profiles of the mean station POC/^{234}Th ratios reveal a striking difference between 1-10 μm and the larger size fractions. Unlike the intermediate and larger size-classes the mean POC/^{234}Th ratio of the 1-10 μm fraction does not decrease with depth but is fairly linear. The most drastic decreases in POC content and thorium activity within the mix layer for the small particle size-class both occur between 50 and 100 m. This can be observed from the Figures 6a and b. Therefore, changes in the POC content and ^{234}Th activity is relatively proportional, yielding a nearly linear POC/^{234}Th profile beyond this depth. On the mean value trace for the 1-10 μm size there is a low point that may be attributable to a flux of 1-10 μm sized particles into the 10-53 μm particle size-class by aggregation. The peak in POC content at 50 m for the 10-53 μm size interval may be a result of this possible transfer of biogenic material between size fractions happening within a depth of 25 to 50 meters. The reason for the decrease in POC/^{234}Th ratio with depth for the intermediate and large size fractions is not understood, but could be due in part to the remineralization of carbon by bacteria.

For most of the analyzed water column the ratio of the small size fraction is about 4 times larger than that of the intermediate and large sized fractions. A log plot of POC/^{234}Th ratio versus diameter size clearly depicts this inverse relationship between POC/^{234}Th and particle size (Fig. 7). This experimental finding indicates that there is some relationship of POC/^{234}Th ratio with particle size, as previously suggested in the model of Burd et al., 2000. Also observable from Figures 6c and 7 is the POC/^{234}Th ratio of the 10-53 μm particle size-class is comparable to the ratio calculated from the >53 μm fraction, which is commonly accepted as representative of the particle size of all the POC sequestered by the ocean.

POC Export Flux and e-Ratios

The Labrador Sea has a large spread in the amount of organic carbon export flux and percentage of the total production that is exported out of the euphotic zone. Particle organic carbon export flux is calculated using the depth at which the primary production rates reached near zero values as the depth that particles leave the euphotic zone. It is quite possible that remineralization might occur within the mix layer. If so, the ratio of integrated POC from surface to euphotic zone over the integrated ^{234}Th activity would not account for the loss of sinking marine particles due to remineralization and would instead tend to over estimate the biogenic carbon actually sequestered by the ocean. In an attempt to account for possible remineralization of carbon the POC/^{234}Th ratio at the bottom of the euphotic zone where the ratio is at its minimum was used to calculate the POC export flux and e-ratios (export ratios, POC export flux over integrated primary production). These calculations were compared with those using an integrated POC/^{234}Th. POC export ratio and e-ratio calculations using the integrated POC/^{234}Th ratio are larger for the intermediate and large size fractions and conversely smaller for the 1-10 μm fraction. Much of the e-ratio values for the two larger fractions were not probable according to the findings of a study of global e-ratio values by Eppley and Peterson, 1979. Many of the e-ratios found by the integrated POC/^{234}Th ratio were well above 0.5 which according to Eppley and Peterson's work is beyond the limit of the percentage of new production that was experimentally found to be exported in the sea (50 % of new production). For this reason, the POC/^{234}Th ratios taken from the bottom of the euphotic zone were used in this study to calculate the carbon export flux. POC export fluxes and corresponding e-ratios are listed in Table 3.

The POC export flux for the intermediate and large size fractions were within the same order of magnitude and varied on average by 1.5 %. This demonstrates that the amount of carbon export flux from the 10-53 μm size-class may be significant. Thus if the particle size distribution of what falls out of the euphotic zone does indeed include particles smaller than >53 μm then the carbon flux into the ocean would be underestimated by as much as fifty percent using carbon flux calculations based on the operationally defined POC/^{234}Th ratio from the >53 μm fraction. Export ratios were calculated for the combined carbon export from all 3 size fractions and from the 10-53 μm and >53 μm particle size-classes alone (Table 3). Stations 9 and 13 had e-ratios less than 0.5 (less than 50 % of new production was exported) for both the combinations of all 3 size fractions and the 2 larger sized fractions.

CONCLUSIONS

The amount of new production and particle scavenging for the end of the spring bloom period in the Labrador Sea is variable. A thorium deficit was observed at all stations, but barely so at station 13. The cause of this may be due to the biological or hydrologic factors at the station, possibly the effect of remineralization or advection, but the cause is not conclusive from this study. Measurements of POC and thorium activity in the Labrador Sea for the 3 size fractions indicate a dependence of POC/^{234}Th on particle size and depth. The POC/^{234}Th ratio and, thus, thorium-derived carbon export fluxes for the 10-53 μm and >53 μm size fractions are similar. E-ratios of combined particle size-classes for stations 9 and 13 are reasonable within the limits proposed by Eppley and Peterson, 1979. This provides evidence that a significant portion of POC export flux is due to intermediate sized particles. It is hoped the results of this project will encourage more studies that quantify the dependence of POC/^{234}Th ratio with size and, in the future, with depth. A better understanding of the dynamics of the carbon-thorium relationship coupled with a quantification of the size distribution of the biogenic fall out will yield ^{234}Th-derived carbon export fluxes that represent ocean carbon budget more accurately.

ACKNOWLEDGEMENTS

I am grateful for the devotion of Rob Pockalny, Rhonda Kenny, Diana Stram, and Chris Kincaid to making the SURFO program not only a summer program that offers some research experience, but allowed participants to learn about the many types of projects in oceanography, meet some of those scientists involved in that research, get a taste of what graduate school requires of you, and learn how to have a blast in Narragansett, Rhode Island! I'd like to thank my two graduate student mentors, Sarah Weinstein and Pat Kelly, for enduring my many interruptions each day, their helpful answers to my questions, and for teaching me how to bale out a boat and when not to jump overboard. From this summer, I not only learned about the relationship of POC and ^{234}Th, but about the importance of asking the right questions in science, how to take on routine lab responsibilities, and the need for balance in life, and I have learned these lessons thanks to the time I was able to spend watching, talking, and working with my advisor Brad Moran. I was blessed with an awesome family for the summer, the SURFOs. We took care of one another like a family and had fun like a family, too! I am sincerely thankful for NSF/REU's support of the URI SURFO program and for the patience of all involved in SURFO.

References

Bruland, K. W. and K. H. Coale, 1986. "Surface Water $^{234}Th/^{238}U$ disequilibria: spatial and temporal variations of scavenging rates within the Pacific Ocean." *In:* Dynamic Processes in the Chemistry of the Upper Ocean (Eds. J.D. Burton, P.G. Brewer, and R. Chesselet), Plenum Press, 159-172.

Buesseler, K.O., Cochran, J.K., Bacon, M.P., Livingston, H.D., Casso, S.A., Hirschberg, D., Hartman, M.C., Fleer, A.P., 1992. Determination of thorium isotopes in seawater by non-destructive and radiochemical procedures. Deep-Sea Research 39, 1103-1114.

Burd, A.B., Moran, S.B., Jackson, G.A., 2000. A coupled adsorption-aggregation model of the POC/^{234}Th ratio of marine particles. Deep-Sea Research I 47, 103-120.

Charette, M.A. and S.B. Moran, 1999. Rates of particle scavenging and particulate organic export estimated using ^{234}Th as a natural tracer in the subtropical and equatorial Atlantic Ocean. Deep-Sea Research 46, 885-905.

Chen, J.H., Edwards, R.L., Wasserburg, G.J., 1986. ^{238}U, ^{234}U, and ^{232}Th in seawater. Earth and Planetary Science Letters 80, 241-251.

Coale, K.H. and K.W. Bruland, 1985. ^{234}Th: ^{238}U disequilibria within the California current. Limnology and Oceanography 30 (1), 22-33.

Cochran, J.K., Buesseler, K.O., Bacon, M.P., Livingston, H.D., 1993. Thorium isotopes as indicators of particle dynamics in the upper ocean: results from the JGOFS North Atlantic Bloom Experiment. Deep-Sea Research I 40, 1569-1595.

Eppley, R.W. and B.J. Peterson, 1979. Particulate organic matter flux and planktonic new production in the deep ocean. Nature 282, 677-680.

Moran, S.B., Buesseler, K.O., Niven, S.E.H., Bacon, M.P., Cochran, J.K., Livingston, H.D., Michaels, A.F., 1993. Regional variability in size-fractionated C/^{234}Th ratios in the upper ocean: importance of biological recycling. The Oceanography Society, Seattle, WA.

Moran, S.B., Ellis, K.M., Smith, J.N., 1997. $^{234}Th/^{238}U$ disequilibrium in the central Arctic Ocean: implications for particulate organic carbon export. Deep-Sea Research II 44 (8), 1593-1606.

Pike, S.M. and S.B. Moran, 1997. Use of Poretics® 0.7 μm pore size glass fiber filters for determination of particulate organic carbon and nitrogen in seawater and freshwater. Marine Chemistry 57, 355-360.

Rutgers van der Loeff, M.M., Friedrich, J., Bathmann, U.V., 1997. Carbon export during the Spring Bloom at the Antarctic Polar Front, determined with the natural tracer ^{234}Th. Deep-Sea Research II 44, 457-478.

Tans, P.P., Fung, I.Y., Takahashi, T., 1990. Observational Constraints on the Global Atmospheric CO_2 Budget. Science 247, 1431-1438.

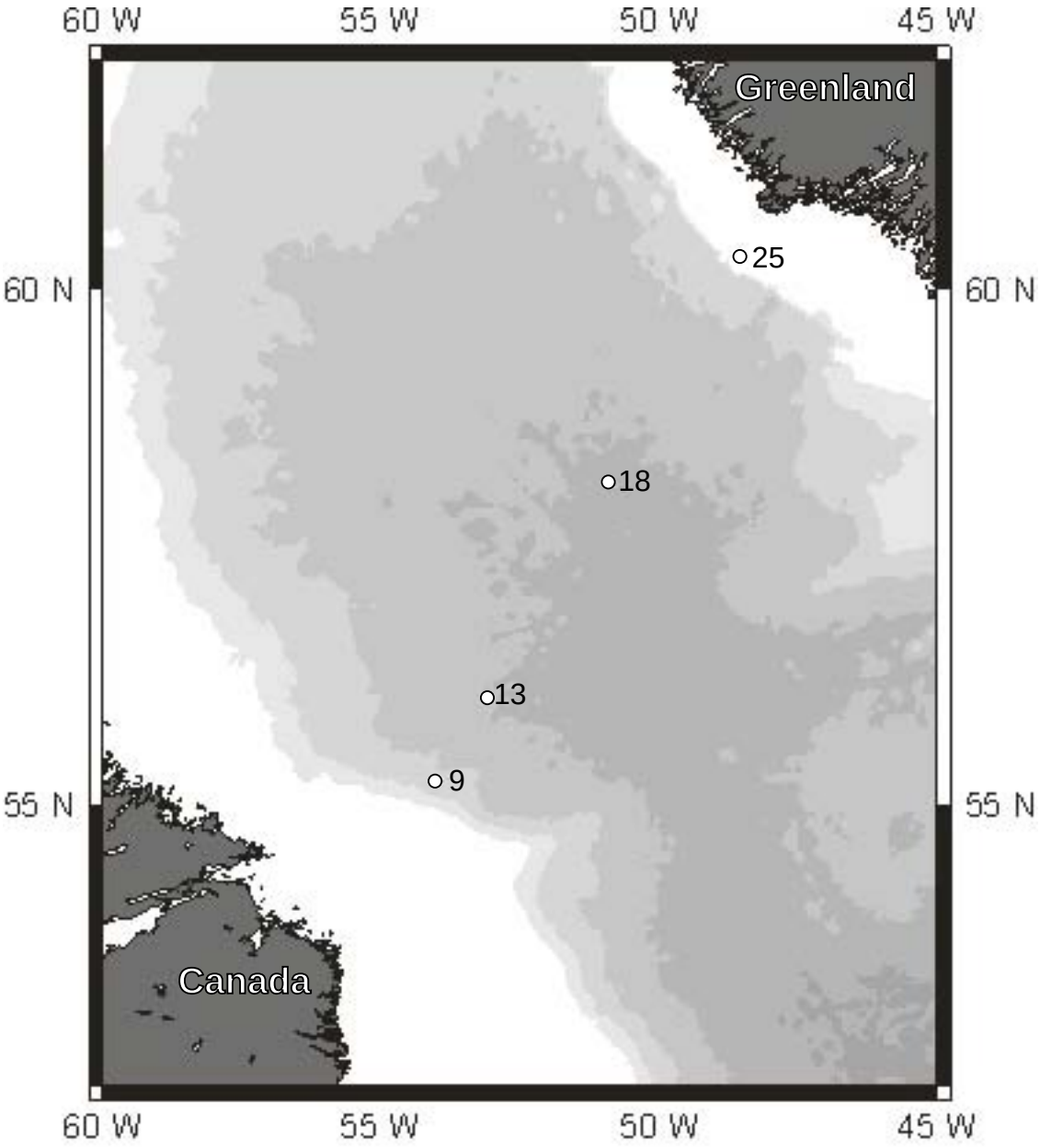

Figure 1. Map of the sampling stations investigated in the Labrador Sea, July 1999.

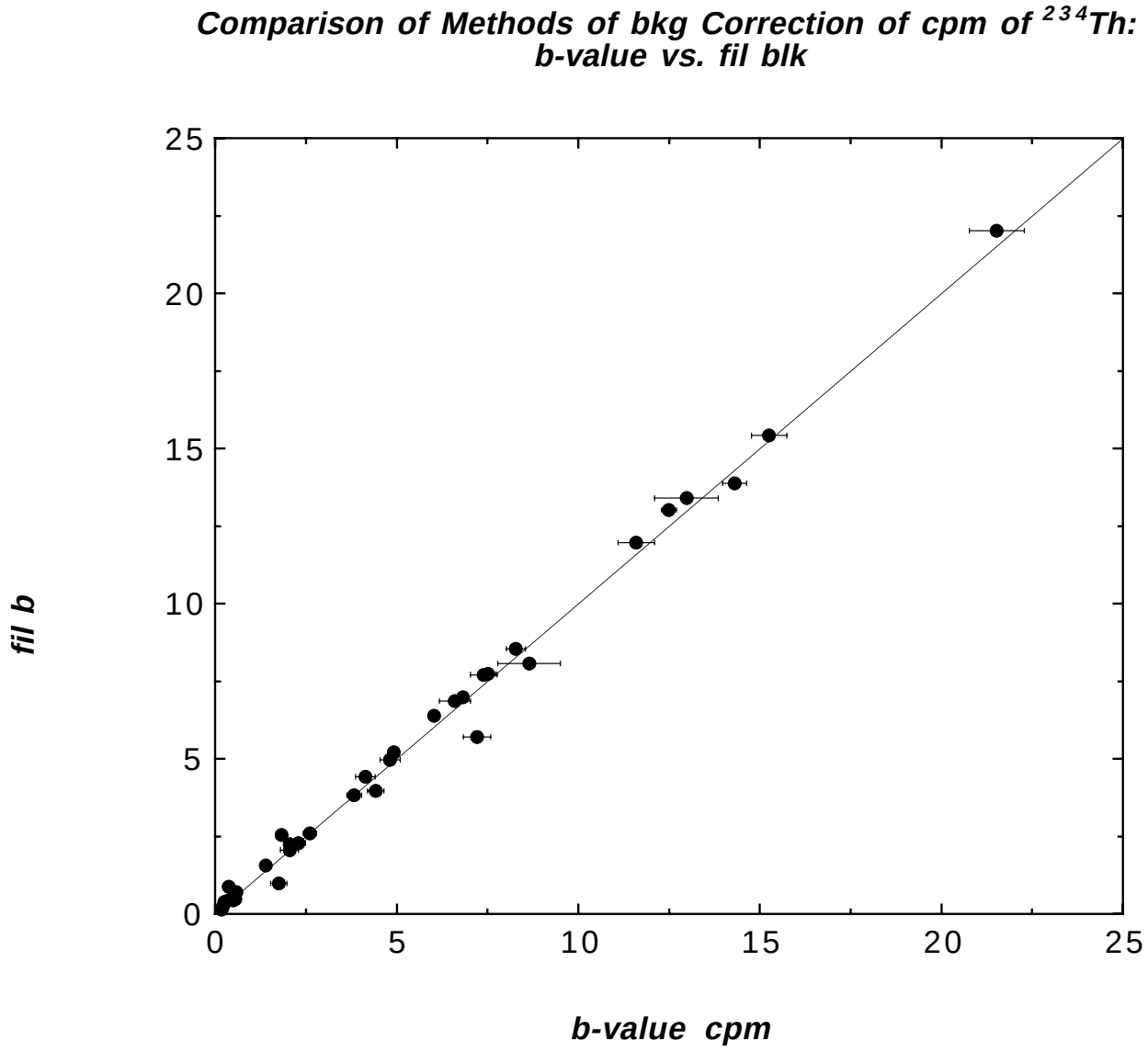

Figure 2. Comparison of Sigma Plot generated "b" values with low-level-beta-counted filter blank values.

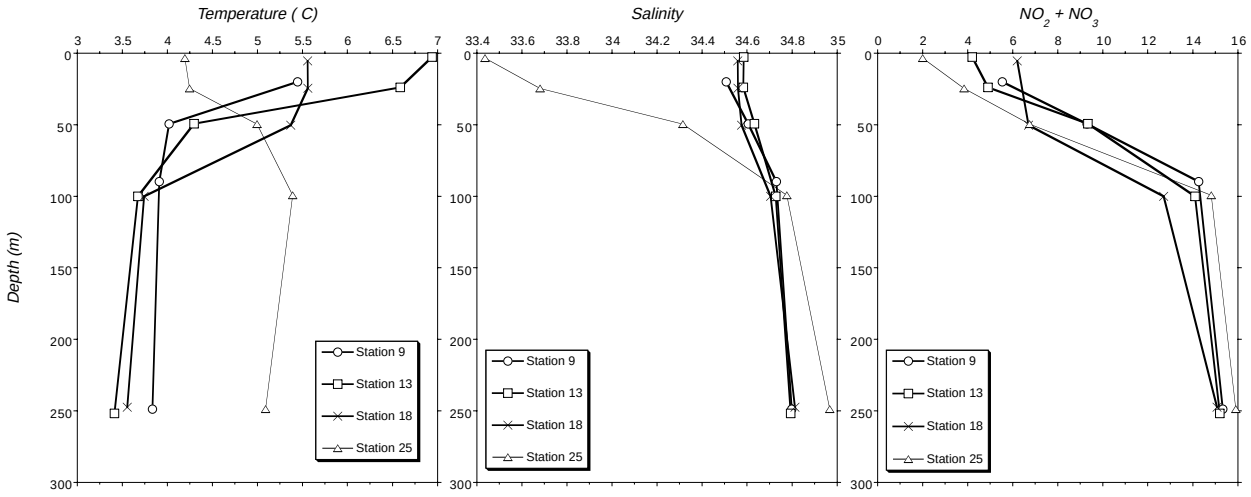

Figure 3. Depth profiles of (a) temperature (˚C), (b) salinity (PSU), and (c) nutrients, $NO_2 + NO_3$ ($\mu mol\ L^{-1}$) in the Labrador Sea.

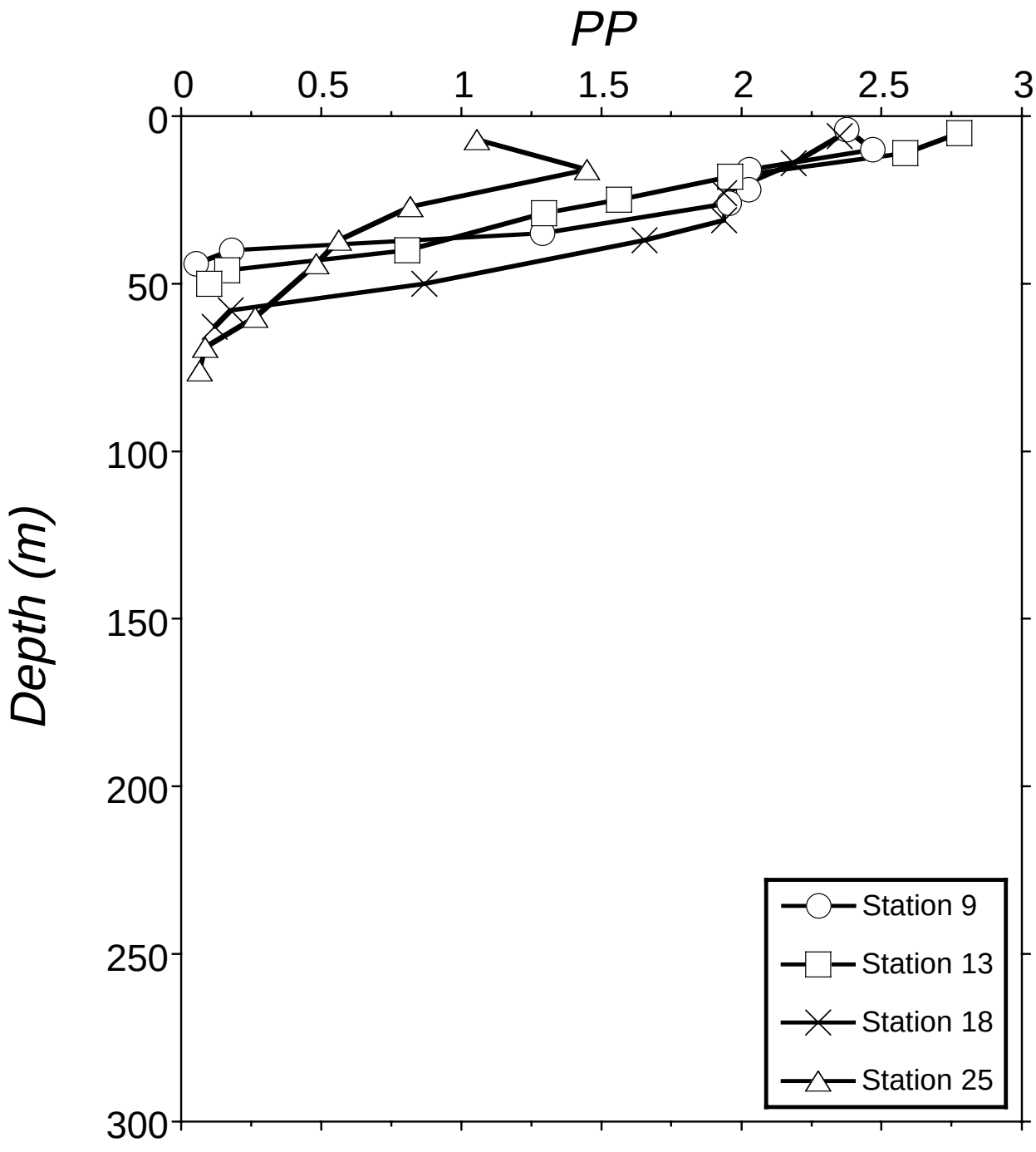

Figure 4. Profiles of primary productivity (PP) in mmol C m^{-3} d^{-1} for stations 9, 13, 18, and 25 in the Labrador Sea, July 1999.

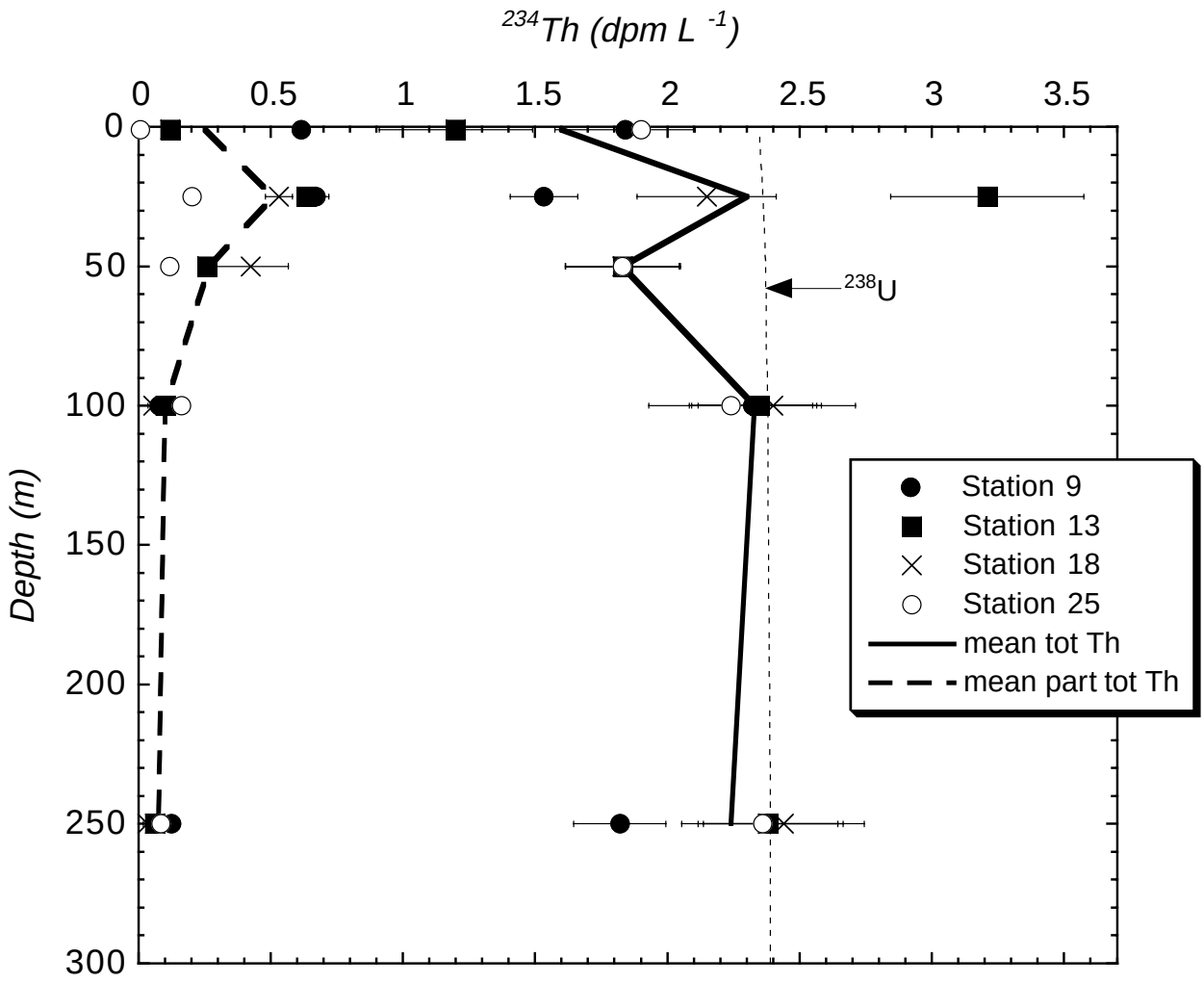

Figure 5. Depth profiles of the station mean ^{238}U activities, total particulate and total ^{234}Th activities of individual stations and the station mean values.

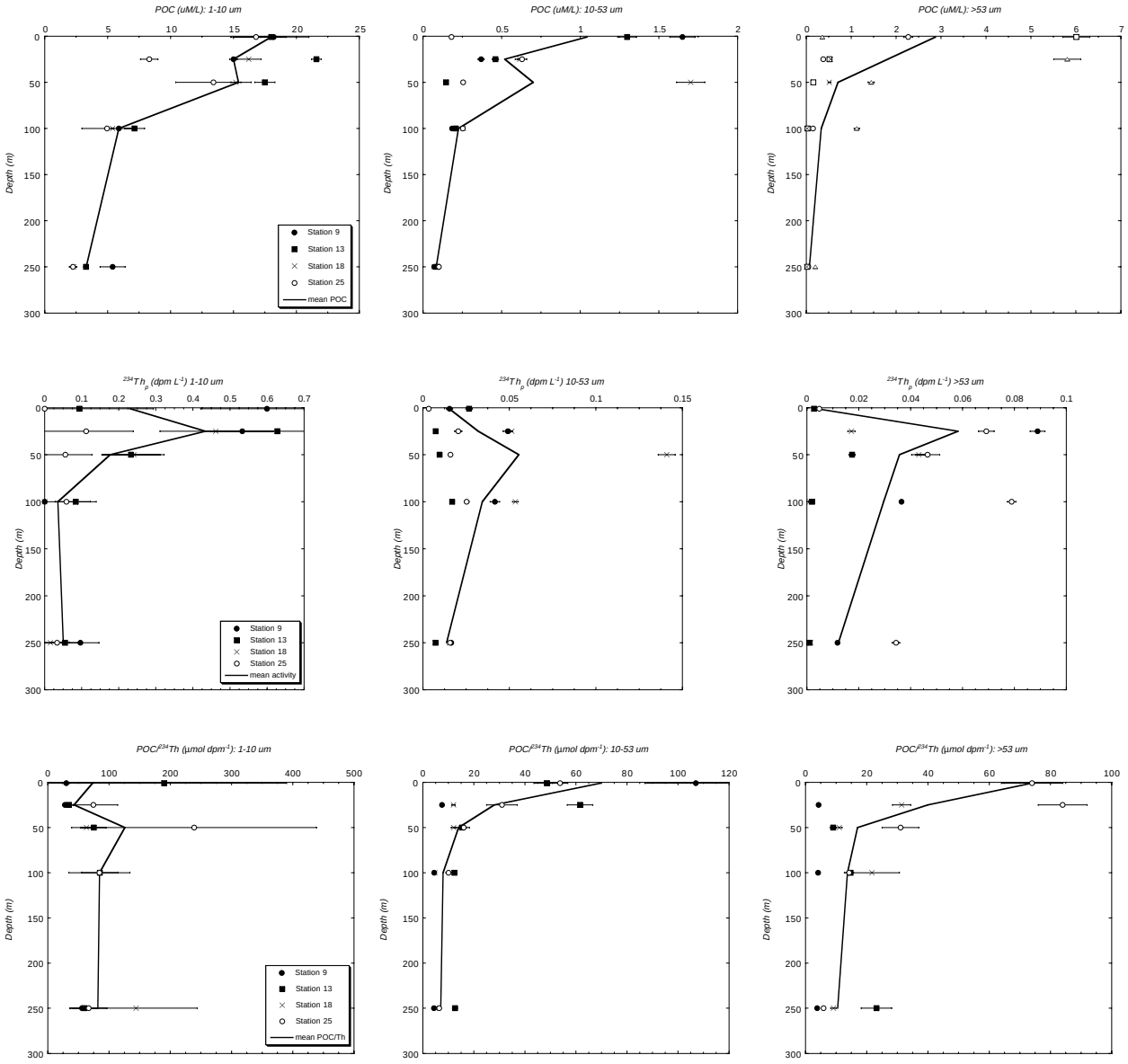

Figure 6. Water column measurements of (top row) Particulate Organic Carbon POC concentration (µmol L^{-1}), (middle row) ^{234}Th activity (dpm L^{-1}), and (bottom row) POC/^{234}Th ratios of 3 size fractions in the Labrador Sea. The solid line represents the mean value of the four stations.

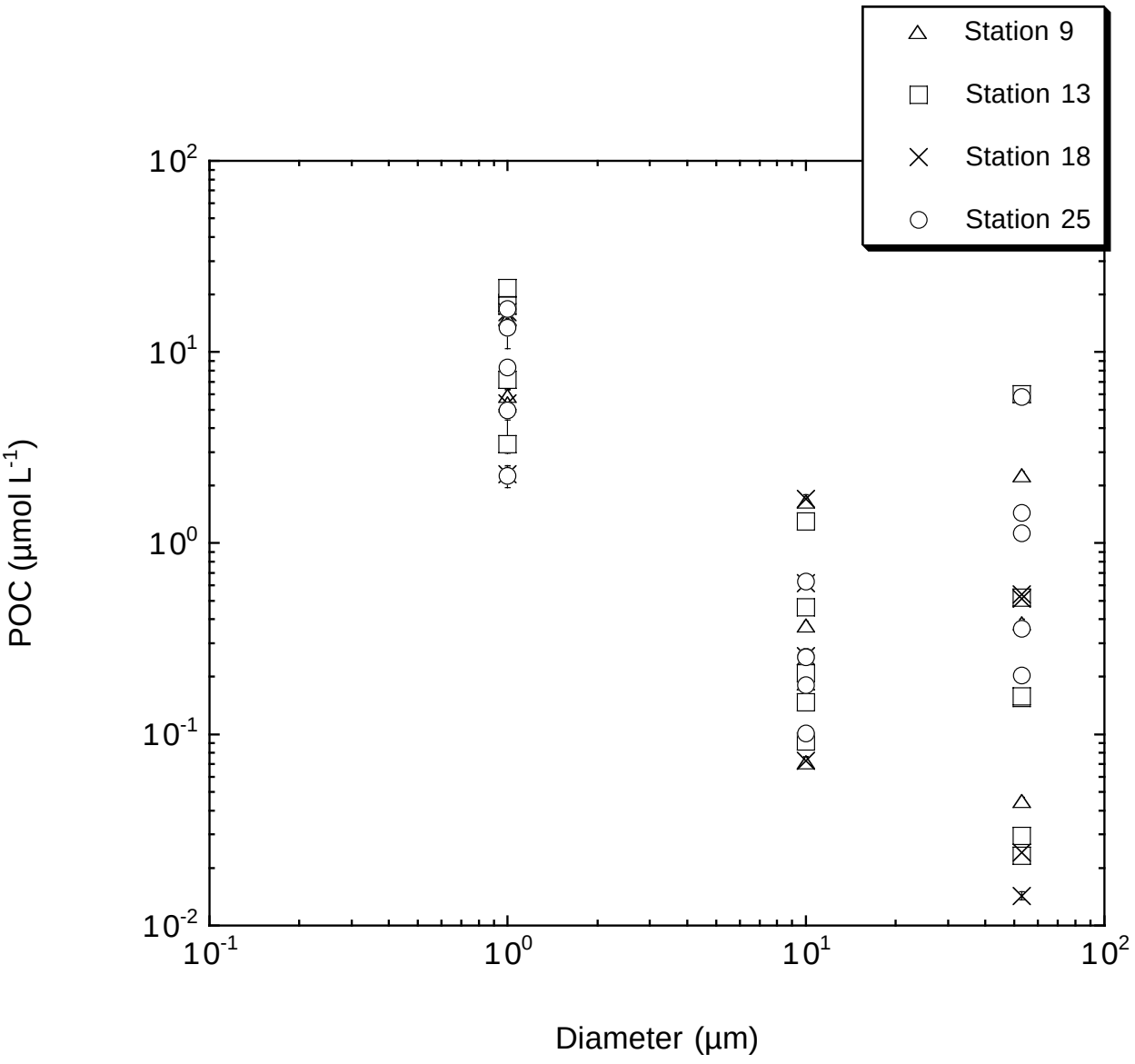

Figure 7. A log-log plot of POC/^{234}Th ratios versus diameter size with 3 size fractions centered at 1 µm, 10 µm, and 53 µm.

Table 1. Depth, salinity, temperature and ^{234}Th activities (dpm L^{-1}) in the Labrador Sea.

Depth (m)	Salinity	Temp. (°C)	$^{234}Th_d$	±	$^{234}Th_{tot-p}$	±	$^{234}Th_{tot}$	±	$^{234}Th/^{238}U$	±
Station 9										
1	34.508	5.45	1.221	0.197	0.615	0.016	1.840	0.266	0.777	0.266
25	34.606	4.02	0.862	0.096	0.671	0.049	1.533	0.127	0.646	0.127
100	34.730	3.91	2.245	0.242	0.078	0.042	2.323	0.242	0.975	0.242
250	34.799	3.84	1.691	0.166	0.125	0.016	1.820	0.174	0.762	0.174
Station 13										
1	34.585	6.94	1.103	0.208	0.120	0.027	1.200	0.290	0.506	0.290
25	34.584	6.59	2.576	0.304	0.635	0.007	3.210	0.365	1.353	0.365
50	34.633	4.30	1.571	0.203	0.260	0.010	1.832	0.218	0.772	0.218
100	34.728	3.67	2.247	0.227	0.103	0.017	2.350	0.233	0.989	0.233
250	34.793	3.41	2.317	0.262	0.063	0.007	2.380	0.264	0.999	0.264
Station 18										
25	34.559	5.56	1.617	0.215	0.531	0.051	2.148	0.263	0.906	0.263
50	34.576	5.37	1.402	0.198	0.425	0.141	1.830	0.215	0.772	0.215
100	34.705	3.74	2.347	0.310	0.055	0.054	2.401	0.310	1.009	0.310
250	34.813	3.55	2.411	0.304	0.033	0.015	2.440	0.305	1.029	0.305
Station 25										
1	33.436	4.20	1.852	0.183	0.008	0.003	1.900	0.180	0.798	0.180
25	33.681	4.25	5.342	0.744	0.202	0.021	5.540	0.754	2.320	0.754
50	34.314	5.00	1.709	0.195	0.119	0.017	1.830	0.208	0.777	0.208
100	34.777	5.39	2.074	0.273	0.163	0.025	2.240	0.281	0.939	0.281
250	34.968	5.09	2.279	0.279	0.084	0.016	2.360	0.281	1.029	0.281

Table 2 Size-fractionated particulate organic carbon (μmol L^{-1}) and particulate ^{234}Th (dpm L^{-1}) in the Labrador Sea, July 1999

Depth (m)	1-10 μm*					10-53 μm					> 53 μm				
	POC	Th	±	POC/Th	±	POC	Th	±	POC/Th	±	POC	Th	±	POC/Th	±
Station 9															
1	18	0.60	0.18	30	6	1.7	0.0154	0.0018	107	20	2.3				
25	15	0.53	0.08	28	3	0.37	0.0491	0.0027	7.5	0.8	0.38	0.0889	0.0029	4.3	0.3
100	5.9	n.d.	-	-	-	0.19	0.0416	0.0028	4.5	0.4	0.15	0.0365	0.0006	4.1	0.3
250	5.4	0.10	0.05	56	20	0.07	0.0164	0.0005	4.4	0.3	0.045	0.0118	0.0003	3.8	0.3
Station 13															
1	18	0.09	0.20	190	200	1.3	0.0267	0.0019	49	5	6.0	0.0028	0.0001	[2100]	100
25	22	0.63	0.20	34	7	0.46	0.0075	0.0002	62	5	0.52				
50	18	0.23	0.08	75	20	0.15	0.0096	0.0011	15	3	0.16	0.0175	0.0012	9	0.9
100	7.2	0.08	0.06	85	30	0.21	0.0169	0.0011	12	1	0.03	0.0020	0.0001	15	1
250	3.3	0.06	0.04	60	20	0.09	0.0073	0.0006	13	1	0.02	0.0010	0.0002	23	5
Station 18															
25	16	0.46	0.15	35	7	0.62	0.0514	0.0005	12	0.7	0.54	0.0172	0.0015	31	3
50	15	0.24	0.08	63	10	1.7	0.1409	0.0049	12	1	0.51	0.0432	0.0028	12	1
100	5.4	n.d.	-	-	-	0.26	0.0535	0.0017	4.8	0.4	0.02	0.0011	0.0004	22	9
250	2.3	0.02	0.03	140	100	0.07	0.0153	0.0009	4.8	0.5	0.01	0.0016	0.0001	9.1	0.9
Station 25															
1	17	n.d.	-	-	-	0.18	0.0034	0.0001	54	3	0.36	0.0048	0.0007	74	10
25	8.3	0.11	0.13	74	40	0.63	0.0204	0.0021	31	6	5.8	0.0692	0.0030	84	8
50	13	0.06	0.07	240	200	0.26	0.0160	0.0006	16	1	1.4	0.0466	0.0047	31	6
100	5.0	0.06	0.06	84	50	0.25	0.0253	0.0014	10	1	1.1	0.0789	0.0017	14	1
250	2.3	0.03	0.03	67	30	0.10	0.0157	0.0001	6	0.3	0.20	0.0344	0.0015	6	0.5

*0.7-10 μm for POC; 1-10 μm for ^{234}Th

n.d. – not determined; "-" not able to be calculated

Table 3. Integrated primary productivity, particulate ^{234}Th export flux, POC/^{234}Th ratios at 250 m, POC export flux, and e-ratios calculated for 10-53 μm and >53 μm particle size classes.

Stn.	Depth Range (m)	∫ PP (mmol m^{-3} d^{-1})	P_{Th} (dpm m^{-2} d^{-1})	POC/^{234}Th$_{250\ m}$ (μmol dpm^{-1})		P_{POC} (mmol m^{-2} d^{-1})		e-ratio	
				10-53 μm	>53 μm	10-53 μm	>53 μm	10-53 μm	>53 μm
9	0-44	66.9	762.1	4.4	3.8	3.3	2.9	0.05	0.04
13	0-50	65.1	10.02	12.6	23.2	0.1	0.2	0.002	0.004
18	0-63	84.3	2211	4.8	9.1	10.5	20.2	0.12	0.24
25	0-76	42.4	1413	6.4	5.9	9.1	8.4	0.21	0.20

A seasonal invasion: changing population dynamics of the ctenophore *Mnemiopsis leidyi* in Narragansett Bay

Casey D. Twanow
Illinois Wesleyan University

Prepared for:
The Summer Undergraduate Research Fellowship in Oceanography

Advisor:
Dr. Barbara Sullivan-Watts

Graduate School of Oceanography
University of Rhode Island

August 2000

Abstract

The ctenophore *Mnemiopsis leidyi* is a dominant predator of zooplankton in Narragansett Bay. The population dynamics of *M. leidyi* in Narragansett Bay have been shifting over the past two decades. The dramatic population peak observed annually in the Bay population is increasingly abundant, and early in the season. Changes in the population dynamics of *M. leidyi* could impact ecosystem densities of zooplankton and phytoplankton significantly. The advancing ctenophore peak intensifies predation and competition of *M. leidyi* with fish eggs and larvae, potentially impacting their recruitment and survival.

The changing seasonality and abundance of *M. leidyi* in Narragansett Bay can be correlated with a significant long-term temperature increase of 2°C in Bay water temperatures over 50 years (Sullivan et al in press). This study investigates the relationship of temperature and *M. leidyi* reproduction. Reproduction was measured at two salinities for 8-13ºC. Results support the presence of a critical temperature below which reproduction is suppressed. Reproduction began at 9ºC in high salinity trials, and at 13ºC at lower salinity. The number of eggs produced and percent of animals that were reproductive increased with temperature. A deeper understanding of *M. leidyi* reproduction will enable researchers to explain and predict bloom events and their effect on the Narragansett Bay ecosystem.

Introduction

Mnemiopsis leidyi and its close congener *Mnemiopsis mccradyi* are carnivorous ctenophores common to estuaries along the Atlantic and Gulf Coasts (Mayer 1912). In Narragansett Bay, *M. leidyi* is a dominant predator of standing zooplankton stock. The Bay population, which is near the northern edge of the species' range, exhibits an annual, rapid increase spanning five orders of magnitude during a one or two month period, followed by a similarly rapid decline (Kremer 1975). This dramatic peak is rare for a carnivore, but is enabled by the species' high fecundity, short generation time, and ability to self-fertilize. Maximum reproductive rates up to 9990 and 14000 eggs released per day have been recorded from *Mnemiopsis* spp. collected in the field (Baker 1973, Kremer 1975). Due to the rapid proliferation and high filtering rates of the ctenophores, *M. leidyi* can significantly affect densities of its zooplankton prey in Narragansett Bay. Filtering rates of 0.36 l mg^{-1} dry wt day^{-1} for tentaculate larvae and 0.052 l mg^{-1} dry wt d^{-1} for lobate adults have been recorded (Deason 1982, Kremer 1975). Kremer suggests that a large animal could reasonably filter 20 l day^{-1} (personal comm).

Studies quantifying ctenophore, zooplankton, and phytoplankton population dynamics in Narragansett Bay were conducted in the 1970's. Results suggested that in several years maximum abundance of *M. leidyi* was related to decreased zooplankton levels and a following phytoplankton bloom (Deason and Smayda 1982). The trophic impact *of M. leidyi* as consumers is further supported by predation estimates. Data from 1970-1974 suggested that *M. leidyi* cleared 5-10% of the Bay's standing stock of *Acartia tonsa*, the dominant copepod species, per day and as much as 30% removal per day was calculated at maximum ctenophore abundance (Kremer 1975). These calculations excluded *M. leidyi* <1cm, which were found to be responsible for a mean 69.8% of the species' zooplankton removal from 1975-1979 (Deason 1982). Deason observed a maximum removal of 91% day-1 of the zooplankton crop in Narragansett Bay, and mean rates of 1.0-6.8% removal during seasons of ctenophore abundance, and 0.04-12.3% in August from 1975-1979. Ctenophores are also significant as a predator and competitor of fish eggs and larvae. They have been identified as competitors of fish and larvae in areas such as the North Sea and Chesapeake Bay (Burrell, 1968). In laboratory studies, significant predation by *M. leidyi* on early stages of *Anchoa mitchilli* has been

documented with clearance rates of 18.01 liters day^{-1} on eggs, 31.90 l d^{-1} for yolk-sac larvae, and 13.93 l d^{-1} on older larvae (Monteleone and Duguay 1988). Cowan and Houde (1983) quantified clearance rates on *A. mitchilli* eggs as 21.17± 3.16 l d^{-1} ml^{-1} and on *Gobiosoma bosci* larvae as 5.16± 4.18 l d^{-1} ml^{-1}. This study also found *M. leidyi* to prey more efficiently on the smallest larvae than eggs or larger larvae. Although fish egg and larvae field removal rates have not been published for Narragansett Bay, unpublished data from Sullivan et al shows filtering rates ranging from 7.9-20.0 l d^{-1} $ctenophore^{-1}$. On June 27, 2000, a filtering rate of 20.0 l d^{-1} was recorded at a concentration of 94.6 ctenophores m^{-3}. This suggests that with random distribution of predators and prey, peak *M. leidyi* populations could potentially filter up to 190% of the fish eggs in the Bay water column.

Narragansett Bay experiences seasonal ctenophore blooms of the highest densities recorded. Historically, this *M. leidyi* population maximum has been observed in late summer or fall. Data from 1950 through the early 1980's shows density peaks for ctenophores >1cm ranging from August to early October. In the past two decades, a trend of increased abundance and earlier maxima in mid-June and early July has been recorded (Sullivan et al in press). In samples collected from the GSO Dock in Narragansett Bay in 2000, *M. leidyi* <1cm reached a peak density of 2146 m^{-3} on June 19. Ctenophores >1cm peaked on July 3 with 127 m^{-3}. Changes in the population dynamics of *M. leidyi* could impact the Narragansett Bay ecosystem extensively. Increased ctenophore abundance could augment the zooplankton removal rates in the Bay, leading to lower standing crops of species central to the ecosystem. Earlier peak densities of ctenophores facilitate a temporal introduction of the species into the spring community. The advancing annual bloom potentially coincides with peak numbers of fish eggs and larvae, as occurred in July 1999 (Sullivan et al in press). Given the substantial clearance rates observed in laboratory studies, predation on fish eggs and young larvae by maximum populations of *M. leidyi* could severely degrade survival and recruitment of species commercially important to Narragansett Bay.

The seasonal pattern of a striking increase and decline of northern populations of *M. leidyi* differs from the species' dynamics in southern estuaries. Southern populations are more stable, maintaining significant levels throughout the year. It can be theorized from

this difference that northern habitats of *M. leidyi* reach certain conditions each year that trigger high fecundity and the following dramatic blooms. The Narragansett Bay bloom is fueled by reproduction of the local population, as math simulation models have shown, not offshore immigration (Kremer 1975). A surprisingly low over-wintering population of 1^{-2} 10^{-4} m^{-3} therefore fuels the summertime peak. Proliferation of this small stock could be controlled by a threshold temperature below which reproduction does not occur. Further support for the presence of this critical temperature is found in documentation of climate change in Narragansett Bay. An increase of 1.73°C in Bay water temperatures since 1950 has been recorded (Hawk 1998). This warming trend has been correlated with the advancing seasonal abundance of *M. leidyi* in recent years (Sullivan et al in press).

Due to the extensive top-down control that *M. leidyi* can exert on zooplankton, attempts to understand and predict the species' changing population dynamics are important to the Narragansett Bay ecosystem. The persistent decline of many regional fish species and their eggs and larvae (Hermsen et al, Keller et al 1999) presses the need for attention to shifts in seasonal community structure. This study explores the relationship of temperature and *M. leidyi* egg production at two salinities. Experimental design focuses on low-end temperatures characteristic of late winter and early spring to investigate the presence of a threshold temperature. Previous unpublished work by Kremer showed a possible critical value between 8°C and 13°C, so temperature experiments within these bounds provide valuable data. Laboratory reproduction rates are known to be greatly dependent on nutritional state of the ctenophores (Kremer unpub, Baker 1973). This introduces the problem of food availability in the laboratory altering results that would be obtained from the field. Since it is difficult to collect *M. leidyi* from the field in winter and spring, however, laboratory studies of reproduction under these conditions will provide valuable knowledge for commercial and environmental use.

Methods

Mnemiopsis leidyi specimens were collected from Wickford Marina on June 8, 2000. Ambient water conditions were 26-27ppt salinity and 23°C. The ctenophores were adjusted to desired experimental conditions by daily changes of 3°C or less, and 5ppt salinity or less. Egg production was measured on the nights of June 28, July 11, July 20,

July 26, Aug. 1, and Aug.9, 2000. Before each of these dates the animals were maintained at experimental conditions for at least 48h. During this acclimation period, ctenophores were fed once daily to a concentration of 100 prey l^{-1}. Prey was natural zooplankton >100μm (?check) from Narragansett Bay for the first four trials. This food was dominantly copepods and copepod nauplii. Cultured *Acartia tonsa* copepods and nauplii were used as prey for the final two trials. Copepods are the main food source for *M. leidyi*, so we attempted to approximate nutrients received in nature since food supply is so closely linked to reproduction. The concentration was chosen based on information that ctenophore growth occurs in the laboratory at concentrations >100 l^{-1} (Kremer 1975). Also, maximum digestive efficiency of M. leidyi on A. tonsa has been documented at 100 prey l^{-1} (Reeve and Walter 1978). Ctenophores were supplemented once daily with *Artemia* nauplii to maintain abundant food. Although growth is reduced on a diet of only *Artemia* (Baker, 1973), the availability of natural zooplankton for a second feeding was limited by low levels in Narragansett Bay from June to August (Sullivan unpub). Five ctenophores were kept in each of four 15 l containers for temperature experiments. A trial at 10°C was repeated with individual ctenophores in 6 l containers to determine containment effects. The animals were maintained on a 12:12 light:dark cycle for the duration of the experiment since *M. leidyi* spawning occurs four to eight hours after dark is initiated (Kremer unpub, Pianka 1974, Freeman and Reynolds 1973) After the two days at experimental temperature, salinity, and prey conditions, ctenophores were isolated overnight in individual 100ml containers of filtered seawater. The number of eggs produced by each individual was counted the following morning. Total length of each animal when suspended in seawater was also measured at the start of each trial to monitor overall growth patterns.

Results

The mean number of eggs produced by ctenophores showed a substantial increase with temperature at both salinities (Figure 1). Animals at 28ppt salinity began to produce limited numbers of eggs at 9ºC, and at 14ppt salinity reproduction did not occur until 13ºC (although in the container control experiment, 1/5 animals at 10ºC, 14ppt salinity produced 29 eggs). Regression equations for the relationship between temperature and

egg production (Figure 2) are y=24.002T-198.20 (R^2=0.50) for animals at 28ppt salinity and y=6.543T-56.193 (R^2=0.1244) for animals at 14ppt salinity. The percent of ctenophores producing eggs also increased with temperature, as did the range in number of eggs produced (Table 1). Differences in size account for very little of the individual variation in range (R^2=0.0441 at 13ºC, 28ppt); individual filtering rates could contribute. Table 1 includes respiration, filtering, and growth rates for temperature effects on physiologic functions.

The control experiment for effects of container size conducted at 10ºC showed that there was no significant difference in egg production under conditions of 5 ctenophores 15 l^{-1} versus 1 ctenophore 6 l^{-1}. There was no significant change in the size distribution of *M. leidyi* through the course of experiments at either salinity (Figures 3&4). Statistical data is reported in Table 2.

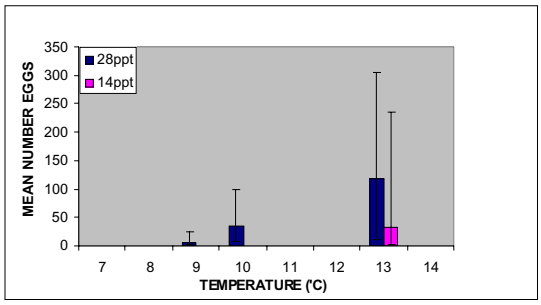

Fig. 1. Mean number eggs produced (columns) and range of eggs produced (error bars) at experimental temperatures. No data was collected for 11 or 12ºC.

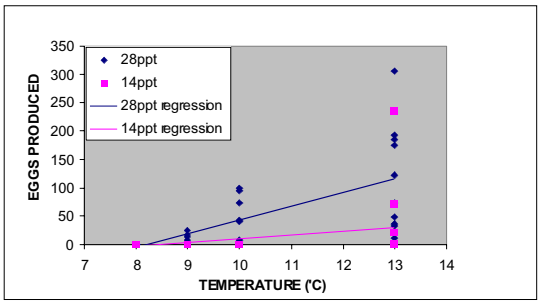

Fig. 2. Regression lines relating temperature and number of eggs produced by experimental *M. leidyi*.

Table 1. Data for the effects of temperature on *M. leidyi* reproduction. Respiration, filtering and growth rates for 5ml *M. leidyi* from Miller 1970.

Temp (ºC)	Salinity (ppt)	# animals in trials	% repro-ductive	Range eggs produced	Respiration (ml O_2 d^{-1})	Filtering rate (l d^{-1})	Growth constant
8	28	20	0	0	0.25 @7ºC	2.85	0.098@7.5ºC
	14	20	0	0			
9	28	10	60	0-26		3.4	
	14	10	0	0			
10	28	10	60	0-100		4.0	
	14	10	0	0			
13	28	10	100	11-306	0.29 @12ºC	6.5	0.179@14ºC
	14	10	40	0-236			

Table 2. Results for statistical analysis of the effects of container size on *M. leidyi* reproduction and of the difference between initial and final size distribution of experimental animals. Parametric tests are t-tests. Non-parametric Mann-Whitney rank sum tests were done for comparisons with unequal variances.

	Salinity (ppt)	Parametric tests	Non-para-metric tests	Significant difference
container effects	28	P=0.3076		no
	14	P=0.1648 unequal variance	P=0.5716	no
size distribution	28	P=0.7573 unequal variance	P=0.6231	no
	14	P=0.0524		no

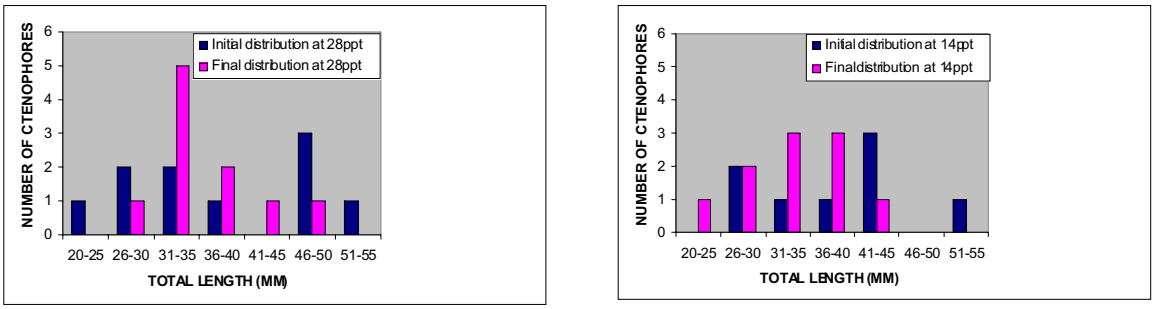

Figs. 3&4. Initial and Final size distributions of *M. leidyi* at 28ppt and 14ppt through the course of the study.

Discussion

The clear relationship of temperature and egg production replicates results in unpublished work by Kremer. Both studies yield compelling evidence that reproduction is suppressed below a certain temperature. This study shows 9°C to be the critical temperature for reproduction at 28ppt salinity, and suggests 10-13°C at 14ppt. Physiologic functions usually increase with temperature, so it is possible that metabolism suppression at low temperatures is accompanied by inhibited reproduction. There is a strong seasonal decline shown in *M. leidyi* production in the field starting in mid-August, with no eggs produced by the end of October (Kremer 1975). This decline can be viewed as further support for a critical reproductive temperature, though it may be related to decreasing prey abundance as well as temperature. The higher critical temperature apparent at lower salinity trials is concurrent with previous evidence that ctenophores are

intolerant of low salinities at low temperatures. In a study by Miller (1970), *M. leidyi* occurred at a minimum salinity of 3.4ppt in summer and of 8.0ppt in winter, while the species extended to the highest salinities in the sampling area in both seasons. Low salinity may increase energy expenditure (Reeve and Walter 1978), and ctenophores could consequently allot less energy to reproduction at lower salinities. This would explain the heightened threshold temperature for reproduction at 14ppt salinity. The trend of the annual *M. leidyi* bloom progressing from the less saline upper Narragansett Bay to the mouth (Kremer 1975) conflicts, however, with expectations based on salinity tolerance.

It is well documented that egg production is highly dependent on the nutritional state of the animals. The filtering rate of *M. leidyi* makes food limitation a constant challenge to overcome in the laboratory to attain high levels of reproduction. At 13°C and 28ppt salinity, ctenophores in Kremer's trials produced a range of 0-250 eggs ctenophore^{-1}, and in this study 11-306 eggs ctenophore^{-1}. This suggests similar effects of food limitation in the two studies. Although no reduction in size occurred in experimental animals, the fact that ctenophores in this study did not experience significant growth could indicate nutritional limits. Conversely, these results may only demonstrate low growth rates characteristic of ctenophores at low temperature.

Reproduction in the field may not always duplicate the temperature trend observed in laboratory. The effects of temperature on reproduction could be amplified in nature by indirect means through impact on feeding behaviors. Studies of food selection on *Mnemiopsis leidyi* using *Acartia tonsa* show that ctenophores apply two main capture mechanisms (Waggett and Costello 1999). Ctenophores often feed with open lobes, catching by response to swimming prey and selecting large copepods. The animals also practice closed-lobe, 'sieving' behaviors, entraining smaller, less nutritious nauplii in auricular flow fields. Based on observations of feeding, it is possible that *M. leidyi* shifts to closed-lobe filter feeding in turbulent waters such as spring and fall mixing (Costello personal comm.). Earlier warming would result in early stratification of the water column. This stable water column would select for an increased frequency of feeding on larger prey, and lead to high reproduction earlier than has been historically observed.

It is conceivable that egg production occurs in nature at lower temperatures than this

study showed. Experimental animals could have been affected by the duration of their containment, or seasonal cycles could have caused a natural decrease in reproduction during the course of the trials. Equipment and food limitations prevented all trials from being run simultaneously, but the acclimation of the ctenophores to low temperatures does not necessarily diminish the application of the study to the field. Since the event of interest is the Bay's increase from winter temperatures, ctenophores that are somewhat adjusted to low temperatures may more closely approximate actual conditions. Under microscope examination, experimental *M. leidyi* appeared to have some damaged auricles and tentillae, but feeding behavior did not seem impaired. Due to weather and the limited availability of mature ctenophores in the field by August, a control experiment for acclimation and containment effects was not conducted.

The application of lab results to field populations of ctenophores is hampered by the common difference between lab and field data. The value of fieldwork, however, is restricted by interpretive difficulties associated with water column inhabitants. Researchers cannot be sure they are sampling the same population at each collection time because of the shifting distribution of cohorts. In addition, continuous breeding and rapid growth inhibit the assessment of factors such as growth and mortality of cohorts (Reeve and Walter 1976). These characteristics of Narragansett Bay and other *M. leidyi* populations necessitate the continued use of laboratory results to analyze trends in nature.

The warming of Bay waters described by Hawk, provides evidence of a temperature-reproduction relationship that is important to Narragansett Bay dynamics. The correlation of the advancing ctenophore peak with the Bay's warming trend can serve as an environmental indicator of other changes occurring in Narragansett Bay. The correlation suggests that the seasonal invasion and abundance will continue, and impacts on other populations will intensify. Anecdotal reports of a long-term reduction in *A. tonsa* populations could be related to increased abundance of ctenophore predators. The reduction of this dominant zooplankton would alter trophic interactions. Another cause for concern is the recent coincidence of the *M. leidyi* bloom with fish egg and larvae peaks. The spawning period of fish species significant to the Bay does not appear to be shifting. Increasing pressure of peak ctenophore predation on fish eggs and young larvae could contribute to declining survival and recruitment of local fish populations.

Conclusions

At the magnitude observed annually in Narragansett Bay, *M. leidyi* obviously has extensive impact as a predator and competitor of zooplankton. The species' changing population dynamics potentially effects densities of copepods, fish eggs, and larvae. The ctenophores also function as major nutrient recyclers in their season of abundance, stimulating primary production and possibly affecting oxygen levels of the water (Kremer and Nixon 1976). Temperature is probably not the only initiator of reproduction, and at field conditions, *M. leidyi* may not observe a critical reproduction temperature of exactly 9°C. The evidence of a threshold temperature, however, is important in light of long-term changes in the Bay ecosystem. The early, abundant *M. leidyi* blooms of recent years may be related to the warming of Bay waters, and a deeper understanding of the population dynamics of this key consumer will allow the blooms to be understood, predicted, and their effects quantified.

Acknowledgements

I would like to thank the SURFO program and GSO for the opportunity to conduct this research in a stimulating learning environment. The constant insight and enthusiasm of Dr. Barbara Sullivan made this study a great experience. I am also grateful to Dr. Pat Kremer for sharing previous results and advice.

References

Baker, L.D. (1973). Ecology of the ctenophore *Mnemiopsis mccradyi* Mayer in Biscayne Bay, Florida. M.S. Thesis, Rosenstiel School of Marine Science, University of Miami Tech. 131p.

Burrell, V.G. (1968). The ecological significance of a ctenophore, *Mnemiopsis leidyi* (A. Agassiz) in a fish nursery ground. M.A. These, The College of William and Mary, Virginia.

Cowan, J.H. Jr.& E.D. Houde. (1992). Size-dependent predation on marine fish larvae by Ctenophores, Scyphomedusae, and Planktivorous fish. Fisheries Oceanography 1: 113-125.

Deason, E.E. (1982). *Mnemiopsis leidyi* (Ctenophora) in Narragansett Bay, 1975-79: Abundance, Size Composition and Estimation of Grazing. Estuarine, Coastal and Shelf Science 15: 121-134.

Deason, E.E. & T.J. Smayda. (1982). Ctenophore-zooplankton-phytoplankton interactions in Narragansett Bay, Rhode Island, USA, during 1972-1977. Journalof Plankton Research 4: 203-217

Hawk, J.D. (1998). The role of the North Atlantic Oscillation in winter climate variability as it relates to the winter-spring bloom in Narragansett Bay. M.S. Thesis, University of Rhode Island, 148p.

Keller, A.A., G. Klein-MacPhee, & J. St. Onge Burns, 1999. Abundance and distribution of ichthyoplankton in Narragansett Bay, Rhode Island, 1989-1990. Estuaries 22: 149-163.

Kremer, P.M. (1975). The ecology of the ctenophore *Mnemiopsis leidyi* in Narragansett Bay. Ph.D. Thesis, University of Rhode Island, 311p.

Kremer, P. & S. Nixon. (1976) Distribution and abundance of the ctenophore *Mnemiopsis leidyi* in Narragansett Bay. Estuarine and Coastal Marine Science 4:627-639.

Mayer, A.G. (1912). Ctenophores of the Atlantic Coast of North America. Pub. 162. Carnegie Institute of Washnington, 50p.

Miller, R.J. (1970). Distribution and energetics of an estuarine population of the ctenophore *M. leidyi*. Ph.D. Thesis, North Carolina State University, Raleigh. 78p.
Monteleone, D.M.& L.E. Duguay. (1988). Laboratory studies of predation by the ctenophore *Mnemiopsis leidyi* on the early stages in the life history of the bay anchovy, *Anchoa mitchilli*. Journal of Plankton Research 10: 359-372.

Pianka, H.D. (1974). Ctenophora. *In* A.C. Giese and J.S. Pearse [eds.], Reproduction of Marine Invertebrates. Academic Press, New York, 201-265.

Reeve, M.R.& M.A. Walter. (1976). A large-scale experiment on the growth andpredation potential of ctenophore populations. *In* G. Mackie [ed.], Coelenterate Ecology and Behavior, Plenum Press, New York.

Reeve, M.R. & M.A. Walter. (1978). Nutritional ecology of ctenophores – a review of recent research. *In* F.S. Russell and M. Yonge [eds.], Advances in Marine Biology, 15, Academic Press, London, 249-287.

Sullivan, B.K., D. Van Keuren & M. Clancy. (1999). Duration and Size of Blooms of the Ctenophore *Mnemiopsis leidyi* in Relation to Temperature in Narragansett Bay, RI.

Waggett, R. & J.H. Costello. (1999). Capture mechanisms used by the lobate ctenophore, *Mnemiopsis leidyi*, preying on the copepod *Acartia tonsa*. Journal of Plankton Research 21: 2037-2052.

The Effect of Barium Sulfate, Iron Oxide and Lead on Acoustic Reflectivity

Hillary Welch
University of Rhode Island

Prepared for:
The Summer Undergraduate Research Fellowship in Oceanography

Advisor:
Dr. Jim Miller

Graduate School of Oceanography
University of Rhode Island

August 2000

Abstract

Gillnet fishing, used by the commercial fishing industry, provides a relatively inexpensive way to catch and haul in large amounts of fish. Unfortunately, it has also been identified as a cause of harbor porpoise (Phocoena phocoena) subpopulation depletion in the areas where it is used. The fishermen are not only catching fish, they are also catching marine mammals, primarily harbor porpoise. The United States government established the Marine Mammal Protection Act of 1972 in order to protect marine mammals. As a result, various restrictions and equipment modifications and additions have been placed on the fishing industry to reduce bycatch of these animals.

Previously, devices emitting an acoustic ping have been employed. These devices, theoretically acting as a warning to harbor porpoise, are heavy and expensive, thereby making them unpopular with the industry. A new idea is to make the nets more acoustically visible to the harbor porpoise by doping the netting with certain chemical compounds. Though little testing has been done, this new method seems to be quite effective. The materials are fairly inexpensive, cause only a slight loss in net strength and require few to no changes in the traditional gillnet fishing process.

This report describes the testing of the effect on acoustic reflectivity of various chemicals, such as Blanc fixe F (precipitated barium sulfate), Iron (II, III) oxide and Lead, all in powdered form. Also described are the methods and materials used in target preparation and data acquisition and analysis methods.

Introduction

The incidental killing of marine mammals by commercial fishing has been a matter of public concern since the late 1960s. The term "bycatch" was coined to describe the inadvertent taking of any species not targeted by the fishery. In 1972, Congress passed the Marine Mammal Protection Act of 1972. The main purpose of the act is to to reduce the killing and serious injury of marine mammals that are being depleted by human interaction.

In recent years, it has been determined that the harbor porpoise population in the Gulf of Maine and Bay of Fundy area is in danger of depletion mainly due to commercial bottom-set gill net fishing practices. Several actions have been taken in an effort to reduce the bycatch levels. Time constraints were placed on the fishing industry, limiting the industry to certain seasons. Attempts to make the net more visible to the mammals have been a big part of the effort to reduce bycatch. Most of the modifications involved acoustical devices. Some are active, such as "pingers", others are passive, such as objects attached to the net or modifications to the net filaments.

This experiment focuses on net filament modifications. Theoretically, adding various chemicals to the net filament will increase the acoustic reflectivity and make the net more visible to the porpoise. In this study, target disks were prepared, one control group and three groups with the following chemicals added: Blanc Fixe F, Iron Oxide and Lead. An acoustic ping was bounced off these targets and each of their target strengths was measured to determine whether or not these chemicals have an effect on acoustic reflectivity.

Background

Harbor Porpoise

The harbor porpoise (*Phocoena phocoena*) is not only one of the smallest Cetaceans, but is also one of the shortest-lived, with a maximum longevity of 17 years. The animal usually has gray to black coloring on the back and a white belly. An adult harbor porpoise reaches lengths from 140-190 cm and weights from 55-65 kilograms. The main diet of the porpoise consists of groundfish, such as herring and mackerel, the same fish targeted by commercial gill-netters. Occasionally, mollusks or crustaceans may also be included in the diet.

Harbor porpoises, like most cetaceans, use echolocation to locate objects underwater. The biosonar of these animals is not fully understood yet. Through many experiments over many

years it has been determined that the harbor porpoise emits bimodal clicks, with the low being between 4-40 kHz and the high between 100-140kHz. Most juveniles dominantly use higher frequencies than adults, comparable to the pitch of a human child's voice versus an adult's voice.

Gill Netting

Gill net fishing targets groundfish in the Gulf of Maine/Bay of Fundy region. The nets are dropped to the ocean floor and left for periods of at least 24 hours. Floats are attached to the net to keep the nets open and upright. The entanglement process incurred by harbor porpoise is poorly understood. Many tests have been conducted and some researchers, such as Au and Jones, have concluded that an echo-locating porpoise has the ability to detect the net at distances large enough to avoid entanglement. These experiments have been conducted in both tanks and open water. This has led some to believe that the animals do not perceive the nets as a danger. In most tank tests, harbor porpoises could detect the net, but once they grew accustomed to it, they grew careless and became entangled (Hatakeyama and Soeda, 1990).

There are several aspects to be considered in order for a net modification to be practical, including; (1) the modifications should have reasonable longevity under commercial fishing conditions, (2) they must be safe to handle, (3) they should be lightweight and inexpensive, and (4) they cannot decrease the catch of target fish species below an economic level (Dawson, 1994). Modifying net filaments seems to fit all these parameters. At the right composition, the nets only lose minimal strength and are slightly heavier. There is no danger in handling the nets, as the chemicals are not soluble. Recent tests have shown that the nets have little to no affect on the target fish species, but are avoided by harbor porpoise (Holy 2000).

Methodology

Materials:

Candle wax (Ordinary candle wax was used due to its low cost and availability.)
Powdered $BaSO_4$, Fe_3O_4 and Pb
Hot plate
Large glass beaker
Digital scale

Monofilament line

Vacuum chamber

Aluminum mold

An ideal target would be a perfect sphere, as orientation would then play no part in reflection. Unfortunately, that proved to be impossible without trapping large amounts of air inside the sphere. Air bubbles would have great target strength and therefore render any results inconclusive.

An aluminum mold of a disk with a radius of 4.5 cm was used to construct the acoustic targets. A disk lacks sharp corners, such as those encountered with a square plate, which helps simplify the orientation of the target while collecting data.

All samples were prepared by percent weight. Targets were made of each of the following chemicals at the following concentrations: 20% $BaSO_4$; 30% Fe_3O_4; 40% Pb. All materials were weighed and set aside. The portion of wax was melted in a large glass beaker over a hot plate. The correct amount of chemical was then added and thoroughly mixed into the wax. Mixing continued until the solution cooled enough to reach a desirable consistency. The solution was then transferred into the pre-greased (with petroleum jelly) aluminum mold and immediately placed in the vacuum chamber. After a 5-10 minute evacuation period, the mold was set aside to cool. When the mold no longer felt warm to the touch, the wax disk was removed and placed on a flat surface to finish cooling. The same procedure was used for the plain disks, omitting the addition of any chemical.

The cooled disk was then placed in a metal ring and the top was shaved to achieve a smooth surface. Three holes were made in the disk as shown in Figure 1, where monofilament line was tied to the disk. Two lines were used to hold the disk from the surface and one was used to weight the disk. Though some of the disks did not require weighting, having density greater than one, all were weighted to stabilize them under water.

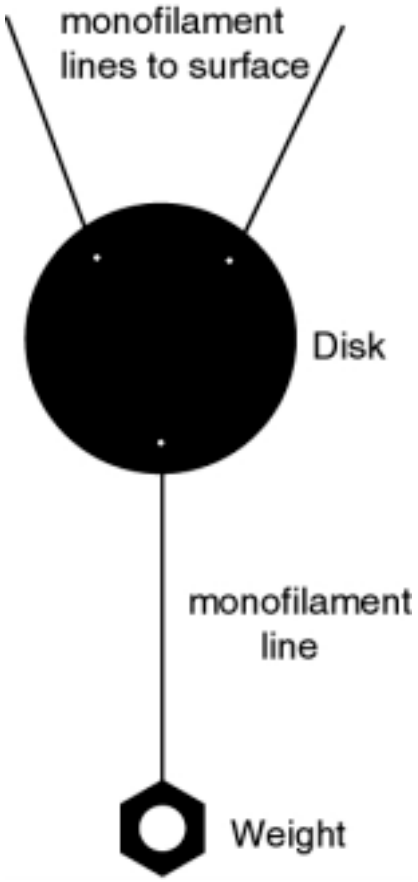

Figure 1: Completed Target

Table 1. Target Data Information

Wax	Radius (r)	Height (h)	Volume (V) $V = \pi r^2 h$	Weight (m)	Density (ρ) $\rho = m/V$
Plain	4.45 cm	.35 cm	21.77 cm^3	19.68 g	.904 g/cm^3
20% $BaSO_4$	4.43 cm	.34 cm	20.96 cm^3	22.12 g	1.06 g/cm^3
30% Fe_3O_4	4.41 cm	.39 cm	23.83 cm^3	27.34 g	1.15 g/cm^3
40% Pb	4.44 cm	.33 cm	20.44 cm^3	31.27 g	1.53 g/cm^3

Experiment

Equipment used in the experiment

- Hewlett Packard 54601A Oscilloscope
- Stanford Research Systems Model DS345 30 MHz Synthesized Function Generator
- Krohn-Hite Model 7500 Amplifier
- Krohn-Hite Model 3550R Filter
- ITC-1001 (reciprocal transducer used as projector)
- ITC-1089 (reciprocal transducer used as hydrophone)
- Wax targets

Experimental Setup

The experiment was run at the University of Rhode Island's Narragansett Bay Campus in the acoustic tank located in the Middleton Building. The tank is 4 m wide, 7.6 m long and 3.6 m deep. To minimize unwanted reflections off of other surfaces, i.e. tank walls, tank bottom or water surface, the whole experimental layout was placed in the middle of the tank.

The experiment was set up as shown in Figures 1-3 and Table 1. The source (ITC-1001) emitted a signal that first passed by the hydrophone (ITC-1089), producing a voltage (V_{in}). It then reflected off the target wax disk and passed by the hydrophone a second time, producing a second voltage (V_{back}). This setup eliminates the need for calibrating the source, as the first pass supplies a reference. This reference signal eliminates the need for correction calculations at each frequency, which could be very time consuming.

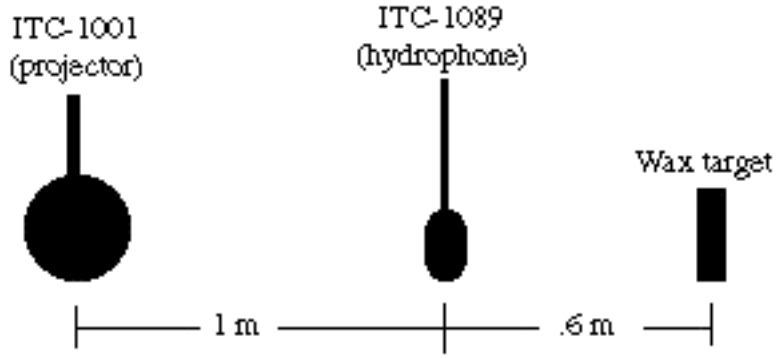

Figure 2: Schematic of Experimental layout (side view)

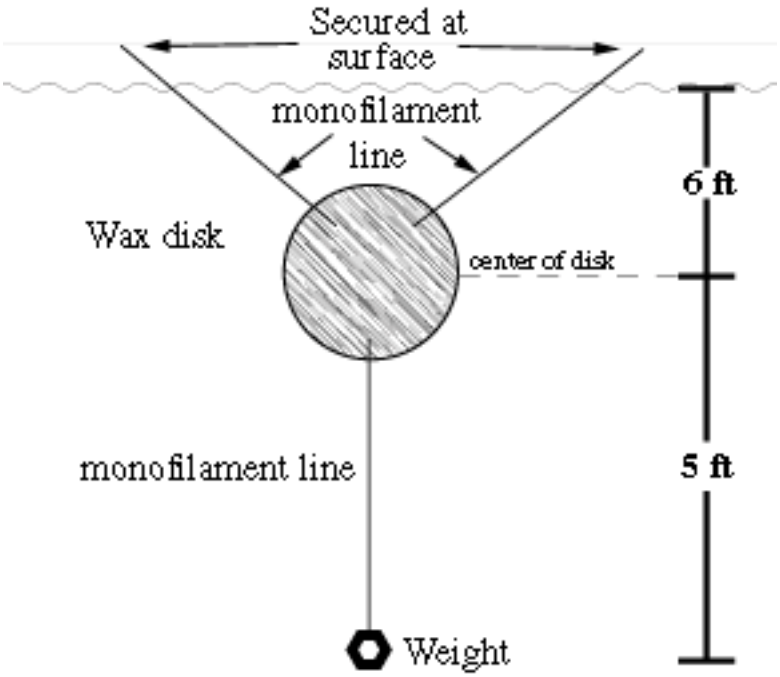

Figure 3: Schematic of disk suspension in tank during experiment

Results

Table 2. Measured output and received signal strength (in volts) for various frequencies and materials used.

Fe_3O_4 (30%) **Distance to phone: .63 m (for f = 10 – 100 kHz) .62 m (for f = 110-150 kHz)** **Depth: 1.8 m**									
Frequency f (kHz)	**V_{in} (V)**	**V_{back} (V)**	**Frequency f (kHz)**	**V_{in} (V)**	**V_{back} (V)**	**Frequency f (kHz)**	**V_{in} (V)**	**V_{back} (V)**
10			60	7.075	0.4031	110	3.563	0.3438
20	90.5	1.094	70	15.5	0.8219	120	3	0.3531
30	46.53	0.8875	80	20.19	1.131	130	1.969	0.3156
40	13.47	0.3625	90	14.69	0.9438	140	1.094	0.1687
50	5.75	0.3	100	6.875	0.475	150	0.7969	0.1094

Plain Wax **Distance to phone: .62 m** **Depth: 1.8 m**								
Frequency f (kHz)	**V_{in} (V)**	**V_{back} (V)**	**Frequency f (kHz)**	**V_{in} (V)**	**V_{back} (V)**	**Frequency f (kHz)**	**V_{in} (V)**	**V_{back} (V)**
10	10.44	0.07812	60	27.19	0.4281	110	9.188	0.1469
20	96.88	0.6687	70	48.13	0.8406	120	26.25	0.3781
30	46.88	0.3344	80	24.84	0.3719	130	24.53	0.3813
40	14.22	0.1344	90	14.69	0.2094	140	17.81	0.3
50	42.5	0.4656	100	11.88	0.1969	150	15.47	0.2312

$BaSO_4$ (20%) **Distance to phone: .61 m** **Depth: 1.8 m**								
Frequency f (kHz)	**V_{in} (V)**	**V_{back} (V)**	**Frequency f (kHz)**	**V_{in} (V)**	**V_{back} (V)**	**Frequency f (kHz)**	**V_{in} (V)**	**V_{back} (V)**
10	10.63	0.1125	60	7.031	0.2625	110	3.75	0.2469
20	96.88	1.2160	70	15.31	0.6312	120	2.813	0.2344
30	46.88	0.7781	80	20.31	0.8188	130	1.906	0.1375
40	14.38	0.2969	90	14.84	0.6469	140	1.094	0.1031
50	5.625	0.1969	100	7.187	0.3281	150	0.7812	0.08125

Lead **Distance to phone: .61 m** **Depth: 1.8 m**								
Frequency f (kHz)	**V_{in} (V)**	**V_{back} (V)**	**Frequency f (kHz)**	**V_{in} (V)**	**V_{back} (V)**	**Frequency f (kHz)**	**V_{in} (V)**	**V_{back} (V)**
10	10.63	0.125	60	6.25	0.4	110	3.563	0.375
20	98.44	1.5	70	15	0.9781	120	2.875	0.4312
30	48.44	1.016	80	18.91	1.197	130	1.812	0.2438
40	14.84	0.475	90	14.22	0.9625	140	1.141	0.1438
50	5.781	0.3188	100	7	0.525	150	0.7031	0.09688

Calculations

Calculated target strengths

The theoretical target strength of a perfect disk is given by, $TS = 20\log(\pi a^2 f/c)$. The target strength for each disk in this experiment was calculated using the equation, $TS = \log (V_{back}/V_{in})$, derived by Dr. James H. Miller. When TS = 0, a perfect reflection has occurred. The closer to zero the TS value, the stronger the target strength. An object with strong target strength would reflect more sound. The calculated target strengths for various frequencies and materials are shown in Table 3.

Table 3 Calculated target strengths for each material at various frequencies. See Figure 4 for a graphical representation.

plain wax frequency	V_{in} (V)	V_{back} (V)	TS
10 kHz	10.44	0.07812	-42.5
20 kHz	96.88	0.6687	-43.2
30 kHz	46.88	0.3344	-42.9
40 kHz	14.22	0.1344	-40.5
50 kHz	42.50	0.4656	-39.2
60 kHz	27.19	0.4281	-36.1
70 kHz	48.13	0.8406	-35.2
80 kHz	24.84	0.3719	-36.5
90 kHz	14.69	0.2094	-36.9
100 kHz	11.88	0.1969	-35.6
110 kHz	9.188	0.1469	-35.9
120 kHz	26.25	0.3781	-36.8
130 kHz	24.53	0.3813	-36.2
140 kHz	17.81	0.3	-35.5
150 kHz	15.47	0.2312	-36.5

$BaSO_4$ frequency	V_{in} (V)	V_{back} (V)	TS
10 kHz	10.63	0.1125	-39.5
20 kHz	96.88	1.216	-38.0
30 kHz	46.88	0.7781	-35.6
40 kHz	14.38	0.2969	-33.7
50 kHz	5.625	0.1969	-29.1
60 kHz	7.031	0.2625	-28.6
70 kHz	15.31	0.6312	-27.7
80 kHz	20.31	0.8188	-27.9
90 kHz	14.84	0.6469	-27.2
100 kHz	7.187	0.3281	-26.8
110 kHz	3.750	0.2469	-23.6
120 kHz	2.813	0.2344	-21.6
130 kHz	1.906	0.1375	-22.8
140 kHz	1.094	0.1031	-20.5
150 kHz	0.7812	0.08125	-19.7

Fe_3O_4 frequency	V_{in} (V)	V_{back} (V)	TS
10 kHz	—	—	—
20 kHz	90.5	1.094	-38.4
30 kHz	46.53	0.8875	-34.4
40 kHz	13.47	0.3625	-31.4
50 kHz	5.75	0.3	-25.7
60 kHz	7.075	0.4031	-24.9
70 kHz	15.50	0.8219	-25.5
80 kHz	20.19	1.131	-25.0
90 kHz	14.69	0.9438	-23.8
100 kHz	6.875	0.475	-23.2
110 kHz	3.563	0.3438	-20.3
120 kHz	3.00	0.3531	-18.6
130 kHz	1.969	0.3156	-15.9
140 kHz	1.094	0.1687	-16.2
150 kHz	0.7969	0.1094	-17.2

Pb frequency	V_{in} (V)	V_{back} (V)	TS
10 kHz	10.63	0.125	-38.6
20 kHz	98.44	1.5	-36.3
30 kHz	48.44	1.016	-33.6
40 kHz	14.84	0.475	-29.9
50 kHz	5.781	0.3188	-25.2
60 kHz	6.25	0.4	-23.9
70 kHz	15.00	0.9781	-23.7
80 kHz	18.91	1.197	-23.9
90 kHz	14.22	0.9625	-23.4
100 kHz	7.00	0.525	-22.5
110 kHz	3.563	0.375	-19.6
120 kHz	2.875	0.4312	-16.5
130 kHz	1.812	0.2438	-17.4
140 kHz	1.141	0.1438	-17.9
150 kHz	0.7031	0.09688	-17.2

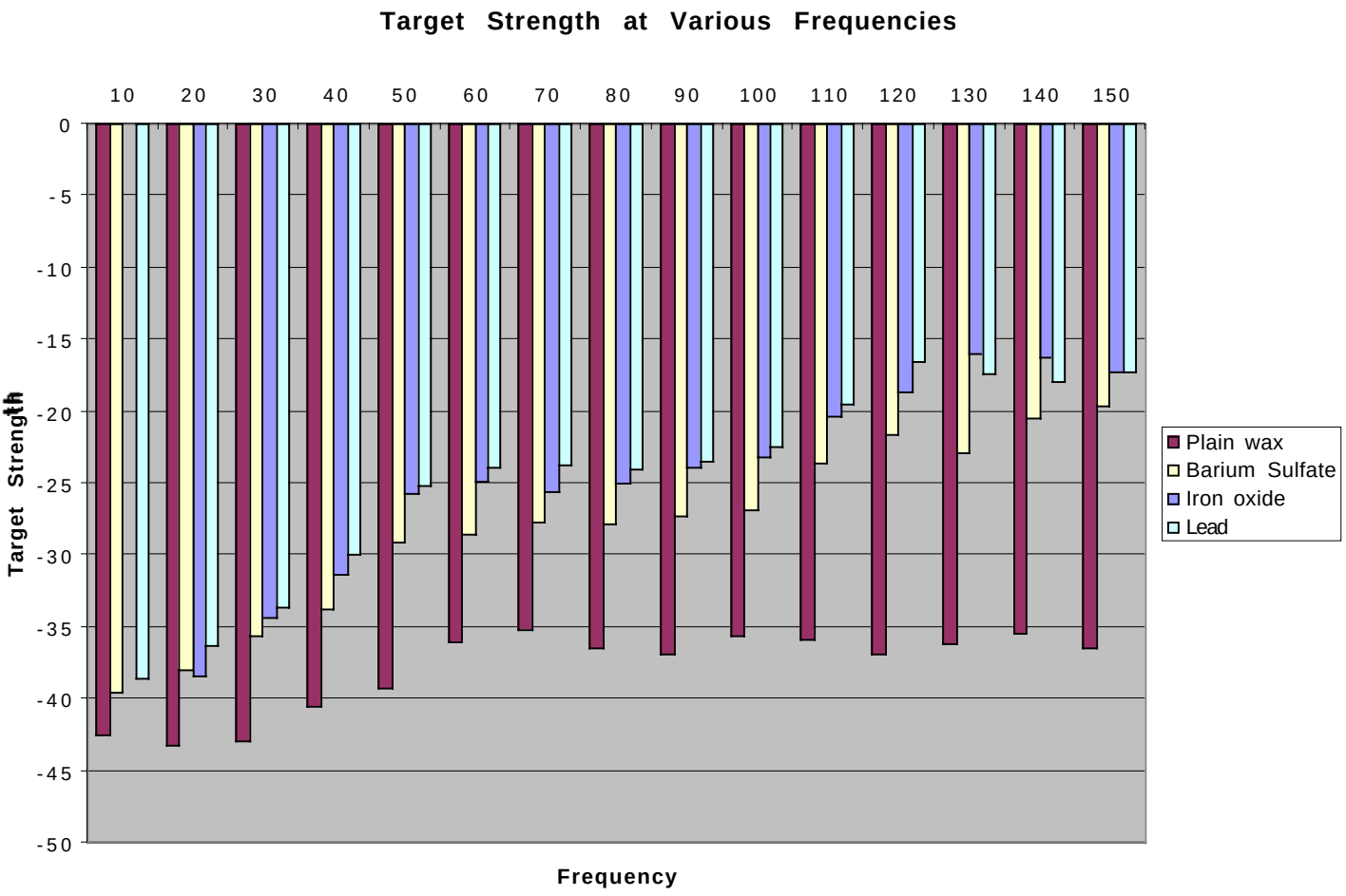

Figure 4. Graphical representation of target strengths calculated for the various materials used and at the various frequencies. These results indicate that greater target strengths are observed for the denser targets and target strengths increase as the frequency increases.

Conclusions and Recommendations

The results of the tests were consistent with what was expected. The disks with chemicals had stronger target strengths and the denser the chemical, the greater the increase in the target strength. Theoretically, adding these chemicals to the net would make it more visible to the harbor porpoise. However, more tests would need to be conducted before a strong conclusion could be made. Also, disks with different concentrations of each chemical should be made and tested.

Bibliography

Au, Whitlow W.L., The Sonar of Dolphins, Springer-Verlag, New York (1993).

Hatakeyama, Y. and Soeda, H., "Studies on Echolocation of Porpoises Taken in Salmon Gillnet Fisheries," in Sensory Abilities of Cetaceans: Laboratory and Field Evidence (eds. Thomas, J.A. and Kastelein, R.A.), NATO ASI Series, Series A: Life Sciences Vol. 196, Plenum Press, New York, 269-281 (1990).

Holy, Norman, personal communication (2000).

Kinsler, L. Frey, A., Coppens, A., and Sanders, J., Fundamentals of Acoustics, Wiley, New York (1982).

Miller, J.H., personal communication (2000).

Urick, R.J., Principles of Underwater Sound, 3rd Ed. McGraw-Hill (1983).

Temporal Occurrence of Thin Phytoplankton Layers in Relation to Physical Processes

Lauren N. Wilkinson
Brown University

Prepared for:
The Summer Undergraduate Research Fellowship in Oceanography

Advisors:
Margaret M. Dekshenieks
Percy L. Donaghay
James M. Sullivan

Graduate School of Oceanography
University of Rhode Island

August 2000

ABSTRACT

In 1998 a cruise was conducted in East Sound, Washington to obtain profiles of the fine-scale optical and physical structure of the water column. The field experiment was designed to study the temporal distributions of thin phytoplankton layers in relation to physical conditions, such as circulation patterns and density gradients.

The results demonstrate that thin layers of phytoplankton are recurrent features in coastal waters. Layers were identified in 34% of the profiles taken from shipboard, with each profile containing from one to five layers. Thin layers were observed at an average depth of 8.09 m. The average layer thickness was 1.06 m. Results from this study also show that physical processes play an important role in thin layer dynamics. The occurrence of layers was particularly affected by wind speed, Richardson number and shear. Thin layers found at high wind speeds (greater than 6 m/s) were thinner and shallower than their counterparts at lower wind speeds. Only 8% of layers occurred in an unstable water column, where the Richardson number was less than 0.25. Additionally, thin layers were concentrated in regions of the water column with highest shear. The results from 1998 are compared to results from a similar study performed in East Sound in 1996.

INTRODUCTION

Thin layers of phytoplankton, less than 5 m thick, are common features in coastal waters under the appropriate physical conditions. In 1996, three cruises were conducted to test fine-scale optical and acoustical instrumentation in East Sound, a fjord on Orcas Island, WA. The high-resolution profiles that were obtained during these cruises revealed that thin layers recurred in East Sound waters over a period of three months. Results from this study also indicated that physical conditions, such as the density gradient and current shear, play an important role in the temporal and spatial distribution of thin layers.

In the summer of 1998, a second field study was conducted in East Sound. This two-week experiment was designed to quantify the physical and biological mechanisms contributing to thin layer formation, maintenance and dispersion. This was a multidisciplinary program, with 15 principal investigators (PIs) from universities, government laboratories and private industry. PIs participating in the 1998 Thin Layers Experiment included: Drs. A. Alldredge and S. MacIntyre (University of California at Santa Barbara); Drs. T. Cowles and R. Zaneveld (Oregon State University); Drs. P. Donaghay, M. Dekshenieks, J. Rines, D. Gifford and D. Smith (University of Rhode Island); Dr. D. Van Holliday (TRACOR); Dr. T. Osborn (The Johns Hopkins University); Dr. M. Perry (University of Maine); Dr. R. Pieper (Southern California Marine Institute); and Drs. A. Weidemann and C. Davis (Naval Research Laboratory). The Office of Naval Research (ONR) funded this work.

The results presented in this paper represent a first analysis of the physical-biological data set from the 1998 experiment. The statistical relationships between thin layers and physical structure will be discussed. Documenting these relationships is the first step toward identifying the specific physical and biological mechanisms that lead to thin layer occurrence.

METHODS

Study Area

East Sound is a small fjord on Orcas Island, WA in the San Juan Archipelago (48º 39'N, 122º 53'W). The Sound is 8 km along the axis, 2 km across the axis and averages 30 m in depth (Figure 1).

Sampling Overview

During the 1998 experiment, 114 fine-scale profiles of biological and physical properties in the water column were obtained over a two-week period, from June 10 to 25. Profiles were measured throughout East Sound (Figure 2). The field experiment was designed to study temporal distributions of thin phytoplankton layers, in relation to physical trends such as wind patterns and density gradients. The sensors utilized in this study were deployed as part of a high-resolution profiling package, capable of simultaneously resolving physical and optical structures on centimeter scales. A Seabird 911+ CTD recorded temperature, salinity, oxygen, pH and depth. Two WET Labs ac-9's measured spectral absorption by particulate material, at nine wavelengths between 412 and 715 nm. Particulate absorption at a wavelength of 440 nm was used as an estimate of phytoplankton distribution.

Current velocity, tidal phase and wind velocity were measured concurrently with the high-resolution profiles. Current velocity was recorded with an RD Instruments 1200 kHz Acoustic Doppler Current Profiler (ADCP), which attached to the side of the research vessel. Tidal phase was measured with two Seabird wave tide gauges, located at the mouth and the head of the Sound, respectively. Wind velocities were recorded with a Davis weather station located on the western bank of the upper Sound. These supplementary measurements provided an appropriate context for the biological and physical profiles. As a result, the data set allowed a thorough investigation of the physical processes and their relationships to thin layer occurrence.

Criteria for Identifying Thin Layers

Four criteria were established in order to define an optical structure as a thin layer.

- First, the optical signal for a layer had to peak above the background level.
- The second criterion was coherence over time. A potential layer had to appear in two or more subsequent casts with the high-resolution profiler. To be coherent, each replicate of the layer had to correspond to the same density surface across casts. This requirement excluded any random or isolated accumulations of phytoplankton from the thin layer analysis.
- Third, an optical signal had to be 5 m or less in thickness to be considered a thin layer. The five-meter benchmark was chosen because it was below the scale routinely sampled on oceanographic cruises with bottles and nets. For consistency, the thickness measurement was taken at the midpoint of each potential layer, where the optical signal was at half its maximum intensity.
- Finally, an optical structure had to contain more than six data points to be counted as a layer. The sampling rate of the ac-9 was 6 Hz. Thus, a single particle moving through the flow cell would produce a signal with one to six data points. Such isolated particles were not indicative of phytoplankton aggregations and therefore were eliminated from thin layer classification.

The Physical-Biological Data Set

Physical and biological properties were extracted from the profiles and recorded in a master database. A comprehensive matrix of data was produced, including the following parameters for each profile:

- profile number
- date, time, and location of profile
- tidal phase
- wind speed and direction
- depth, thickness, intensity and relation to pycnocline for the location of each layer in the water column
- density, temperature, salinity, buoyancy frequency, shear and Richardson number at the location of each layer in the water column

- average density, temperature, salinity, buoyancy frequency, shear and Richardson number for the whole water column in a given profile.
- The database, once completed, was used to identify physical and biological relationships.

RESULTS

Layer Coherence

Graphical examples of layer coherence over time are provided in Figures 3 through 7. These illustrations also offer a summary of the various types of thin layers that were encountered.

Some phytoplankton layers exhibited both temporal and spatial coherence (Figure 3). For example, a layer observed on June 16 remained stable for several hours over two different locations (Figure 3a). The layer split into two separate peaks (Figure 3b), which later converged back into one peak (Figure 3f). Eventually the structure dispersed altogether (Figure 3g). The strong correlation ($r^2 = 0.8448$) in density values for each recurrence of the layer demonstrates that these layers are replicates.

The most obvious layers to identify had very large optical peaks in comparison to associated background levels (Figure 4). Results from June 19 exemplified this classical type of layer. In each replicate, the structure was directly associated with the same sharp, well-defined pycnocline. The apparently weak density correlation ($r^2 = 0.247$) between layer replicates can be explained by the dramatic change in density (roughly 0.5 sigma-theta) across the pycnocline. That, combined with inherent uncertainty in determining the exact midpoint of the layer, allowed for substantial variability.

Profiles taken later in the day on June 19 (Figure 5) revealed a layer with characteristics quite different to those typically expected. The first occurrence of the layer gave an optical signal just 1.5 times the background (Figure 5b). By the third replicate, the peak had enlarged to twice the background intensity (Figure 5d). Still, the layer was fairly small. Additionally, it did not appear to be related to a density change in the water column. However, the strong correlation ($r^2 = 0.961$) in density values across

replicates demonstrates temporal coherence. The layer, though small, was located on the same density surface over three different casts.

A similar type of structure was observed on June 20 (Figure 6). Here again, the layer of interest did not appear to correspond to a density change. However, coherence across replicates is evident in the strong correlation value ($r^2 = 0.996$) across profiles.

The set of profiles for June 23 (Figure 7) was characterized by a rapidly changing density structure. The first profile revealed a gentle density slope (Figure 7b). This slope differentiated into notably sharper stairsteps in just an hour's time (Figure 7c). Corresponding to the density change, layers were observed to shift downward until they disappeared altogether (Figure 7d). The top layer showed a strong density correlation ($r^2 = 0.984$) between replicate casts. No correlation was calculated for the lower layers, since they only appeared in two casts before dispersing. The dramatic difference in density structure from one cast to the next suggests the influence of advection. This in turn might explain why the layers shifted in the water column and ultimately were mixed away.

General Thin Layer Characteristics

Thin phytoplankton layers were detected in 34% of the 113 profiles collected (Table 1). A single profile contained from one to five layers. In total, 103 thin layers were observed.

Thin layers were measured at depths as shallow as 0.65 m and as deep as 25.07 m. The average layer depth was 8.09 m. Histograms show that most layers occurred in the upper water column, with 73% in depths shallower than 10 m (Figure 8a). Layers ranged in thickness from 6 cm to 2.77 m, with an average of 1.06 m. Roughly 53% of all layers were less than 1 m in thickness, while 85% were thinner than 2 m (Figure 8b). Layer intensity, or a_p440, ranged from 0.23 m^{-1} to 1.32 m^{-1}. Average a_p440 was 0.58 m^{-1}. About 97% of thin phytoplankton layers had absorption intensities in the range of 0.2 m^{-1} to 1 m^{-1} (Figure 8c). On average, the optical peaks for layers were 2.2 times larger than background levels. This peak-to-background intensity ratio ranged from 0.44 to 8.53 (Table 1). Histograms show that 46% of layers had optical peaks 2 or more times larger

than the background; and 19% had peaks at least 3 times greater than background. Roughly 15% of the layers had peaks smaller than 1 times the background (Figure 8d).

Buoyancy frequency, shear and Richardson number were calculated from physical measurements made at the exact location of each thin layer. Layers occurred over a broad range of buoyancy frequencies (Figure 8e). Approximately 53% of all layers occurred in regions where the buoyancy frequency was relatively high, i.e., greater than 0.0005 $(rads/s)^2$. Thin layers were also found in a broad range of shears, between 0 and 0.09 s^{-1} (Figure 8f). Relatively high shears, larger than 0.025 s^{-1}, were observed in 47% of the layers. Comparable values of high shear, greater than 0.025 s^{-1}, were observed in only 17% of the water column as a whole. Finally, Richardson number, which is the ratio of buoyant restoring force to shear, was calculated at the exact location of each layer. Results show that just 8% of the layers occurred where the Richardson number was less than 0.25 (Figure 8g). A Richardson number less than 0.25 indicates an unstable water column (Mann and Lazier 1991).

Roughly 34% of the thin layers were found in water columns with a weakly defined pycnocline. Approximately 65% of the layers corresponded to a density change of less than 0.1 sigma-theta (Figure 8h).

Thin layer attributes as a function of wind speed were also investigated (Figure 9). For this analysis, wind speeds were averaged over the hour prior to each profiler cast. Layers at very high wind speeds were located at depths generally more shallow than those at lower wind speeds (Figure 9a). No layers were detected below 7.5 m in areas where wind speeds surpassed 6 m/s. At wind speeds less than 6 m/s, layers were found as deep as 25.07 m (cf. Table 1). Similarly, layers were generally thinner at the highest wind speeds (Figure 9b). At wind speeds greater than 6 m/s, the thickest layer found was 1.81 m, compared to a maximum thickness of 2.77 m at lower wind speeds. Maximum intensity showed no clear relationship with wind (Figure 9c), while peak-to-background ratio dropped notably at high wind speeds (Figure 9d). The optical peaks for layers in high winds (greater than 6 m/s) ranged to 1.5 times the background level as an upper maximum. At wind speeds lower than 6 m/s, layers were found with optical signals up to 6 times larger than the background. In summary, layers found at high wind speeds were weaker, thinner and shallower than their counterparts at more moderate wind speeds.

The results revealed an interesting pattern in wind speed distributions where thin layers occurred. Wind speeds as a whole, over the two-week testing period, spanned a fairly broad range from 0 to 9 m/s (Figure 10b). However, thin layers only occurred at wind speeds between 1.5 and 7 m/s. Furthermore, 80% of the layers corresponded to wind speeds in the narrow range of 3 to 5 m/s (Figure 10d). This range accounted for only 34% of total wind speed distribution over the testing period.

Temporal Occurrence of Thin Phytoplankton Layers and Physical Conditions

To discern temporal patterns in thin layer attributes, layer thickness and intensity results were plotted sequentially in the order that each layer was encountered (Figure 11). No clear temporal trend was observed for layer thickness over the two-week period (Figure 11a). The values were evenly distributed in a range of 6 cm to 2.77 m over the two-week testing period. Layer intensity shifted over time to a higher and more broadly distributed range of values (Figure 11b). As previously noted, the overall average intensity was 0.58 m^{-1}, with a range of 0.23 m^{-1} to 1.32 m^{-1}. Peak-to-background intensity ratios were lowest at the end of the testing period (Figure 11c). Layers had optical peaks ranging from 0.44 to 8.53 times larger than the background, with an average peak-to-background ratio of 2.2 (cf. Table 1).

The physical attributes associated with layers were analyzed by plotting the physical parameters sequentially in the order in which each layer was encountered. Density values reflected trends in salinity and temperature ranges over time (Figure 11d,e,f). Toward the beginning of the cruise, layers associated with a relatively broad salinity range. Over the two-week period, salinity generally increased in value and narrowed in range. Average salinity was roughly 28.9 psu. Layers were observed at a consistently narrow range of temperature, with an overall average of 12.4ºC. The temperature increased by about 1ºC near the end of the testing period. These patterns in salinity and temperature produced the temporal trend in densities associated with thin layers. As salinity gently increased (starting at about the 50^{th} layer), the density increased accordingly. However, the density values began to decrease again when temperature rose by a degree (at about the 95^{th} layer). No clear temporal trend was observed in the density change across each layer (Figure 11g). Thin layers corresponded to an average density change in the water column

of 0.09 sigma-theta. In regions of the water column where thin layers were located, buoyancy frequency tended to decrease in value over time (Figure 11h). Average buoyancy frequency where layers occurred was 0.001 $(rads/s)^2$. This value is almost twice the observed buoyancy frequency for the whole water column, of 0.0006 $(rads/s)^2$. Thus thin layers were concentrated in those regions with strongest buoyant restoring force. No clear temporal trend was observed in the shear values at which thin layers occurred (Figure 11i). The Richardson number, which was calculated from buoyancy frequency and shear, slightly decreased in value over time (Figure 11j). This downward slope in value followed the decrease in buoyancy frequency. As noted earlier, only 8% of the layers were identified in regions of the water column where Richardson number was below 0.25.

DISCUSSION

Comparison With 1996 Results

The results presented in this paper were patterned after an earlier experiment in East Sound in 1996 (Dekshenieks et al. submitted b). The 1996 data set included 120 profiles from three cruises conducted in late May through early September. A comparable number of profiles (113) was obtained in 1998 over a shorter (two-week) time period (cf. Table 1). The thin phytoplankton layers found in 1998 were quite different from those in 1996. A comparison of the two studies provides insight into the question of whether thin layers are recurring phenomena over time.

In 1996, the criteria for defining thin layers included a stipulation that the optical peak for a layer be three times greater than the background level. (Dekshenieks et al. submitted b). However, only 19% of the layers found in 1998 could meet this requirement (cf. Figure 8d). Since the structures in general were smaller than those found in 1996, the defining criteria were altered for the 1998 data set. If structures, though small, showed coherence over time and could meet the other three defining criteria, then they were included as thin layers (cf. Figure 5).

In the 1996 study, a higher percentage of profiles (54%) had layers than in 1998 (34%) (Dekshenieks et al. submitted b, cf. Table 1). A total of 119 layers was observed in 1996, compared to 103 in 1998. In addition, the 1996 results revealed generally fewer (up to three) layers per profile compared to 1998, when each profile contained up to five layers. This difference might be explained by the change in criteria for defining layers. The layer count from 1996 did not include particulate aggregations with optical peaks less than three times the background level.

Layer depth and thickness were comparable over the two years. The 1996 profiles revealed 80% of layers at depths less than 10 m, while 73% were observed at the same range in 1998 (Dekshenieks et al. submitted b). Average layer depth for 1996 was 6.69 m, just slightly shallower than the average for 1998 of 8.09 m depth (cf. Table 1). Average layer thickness was 1.2 m in 1996, compared to 1.06 m in 1998.

On average, the layer absorption intensities observed in 1996 were more than twice as large as those seen in 1998. Average a_p440 was 1.33 m^{-1} in 1996, compared to 0.58 m^{-1} in 1998 (Dekshenieks et al. submitted b, cf. Table 1). This indicates that the layers in 1998 were substantially weaker than those observed in 1996. Even more compelling is the observation that the maximum layer intensity observed in 1998 was 1.32 m^{-1}, i.e., less than the average for 1996.

Buoyancy frequency, shear and Richardson number at each layer location were comparable in value for both years. In both studies, the majority (60% in 1996 and 53% in 1998) of layers occurred in regions of the water column where buoyancy frequency exceeded 0.0005 $(rads/s)^2$ (Dekshenieks et al. submitted b). Buoyancy frequency is commonly used to indicate the strength of the density gradient in the water column. It describes the frequency of oscillation that results when the pycnocline is displaced and then left to return to its rest position. High buoyancy frequencies indicate short restoration times, which in turn indicate a strong pycnocline. Shear values fell in the same range of 0 to 0.09 s^{-1} for both 1996 and 1998 (cf. Figure 8f). Shear has been cited as a possible mechanism causing the development of thin layers (Osborn 1998). The 1998 results supported this hypothesis with the finding that layers were concentrated in regions of the water column with highest shear. As noted previously, shears larger than 0.025 s^{-1} were observed in nearly half (47%) of the layers. Comparable shears were

observed in only 17% of the water column as a whole. Both 1996 and 1998 results showed that more than 90% of layers occurred at Richardson numbers above 0.25 (cf. Figure 8g). Generally, the water column is unstable in regions where the Richardson number is below a value of 0.25 (Mann and Lazier 1991). An unstable water column is less likely to support thin layer development.

In general, the 1996 profiles were characterized by stronger, more clearly defined density gradients than those seen in 1998. Roughly 71% of all 1996 layers were directly associated with a sharp pycnocline; and just 15% were sampled when the pycnocline was weakly defined (Dekshenieks et al. submitted b). In 1998, twice as many profiles (34%) revealed a weakly defined pycnocline. Additionally, 65% of the layers corresponded to a density change of less than 0.1 sigma-theta (Figure 8h). The results indicate that many of the 1998 layers were associated with small density stairsteps rather than sharp pycnoclines. This difference in density structure may explain why more layers, with higher intensities, were observed in 1996 compared to 1998.

The relationship between thin layer attributes and wind speed differed from 1996 to 1998. The 1996 profiles revealed no correlation between wind speed and layer thickness or layer depth (Dekshenieks et al. submitted b). In 1998, however, layers observed at high wind speeds were notably thinner and shallower in depth than those layers at more moderate wind speeds (cf. Figure 9). Conversely, no clear relationship between wind speed and layer intensity was observed in 1998. The 1996 results, however, showed that highest layer intensities occurred at lower wind speeds. Overall, the results from both years suggest that the strongest layers tend to develop in relatively low to moderate wind conditions.

As seen in histograms, thin phytoplankton layers observed in 1998 corresponded to a much more narrow range of wind speeds than those in 1996 (cf. Figure 10). Only the late May and June data were included in the 1996 wind histograms, for seasonal comparison with June 1998 data. Wind speeds as a whole in May/June 1996 spanned a broad range from 0 to 13.5 m/s. Where layers were found, the wind speeds were slightly lower, with a maximum 10.5 m/s (Figure 10a,c). Similarly, no layers in 1998 occurred at the highest observed wind speeds (cf. Figure 10b,d). In 1996, however, the histogram of wind speeds associated with layers was not drastically different from the distribution of wind

speeds as a whole. Conversely, the layers in 1998 corresponded to a narrowly concentrated range of wind speeds compared to overall conditions. As noted in the results, 80% of the layers were found at wind speeds between 3 and 5 m/s. This small range accounted for only 34% of total wind speed distribution over the testing period. Such a finding provides compelling evidence for a strong dependence on wind speed for thin layer development in 1998. If wind speeds are too high, then layers are likely to get mixed away. On the other hand, a moderate amount of wind is necessary to create shear, which may be an essential element to thin layer development (Osborn 1998). In 1998, no layers occurred when wind speeds were lower than 1.5 m/s. At such low winds, the water column would probably have very little, if any, wind-driven shear. Thus the results suggest that thin layer development may depend on shear.

East Sound has a predominantly two-layered flow (Dekshenieks et al. submitted a). The surface waters from 0 to 10 m deep are predominantly wind-driven. Below this surface layer, the flow is tidally forced. In both 1996 and 1998, layers were most often found at the interface of these two layers (i.e., at depths shallower than 10 m). In 1996, the surface layer was also strongly influenced by, and predominantly defined by, the Fraser River outflow. The Fraser River, which is located outside the Sound (cf. Figure 1), is the major source of freshwater for the Sound. In 1998, the Fraser River outflow was significantly lower than in 1996, and thus did not have the same stabilizing force on the surface water layer. For this reason, comparably lower wind velocities were able to mix the surface layer in 1998. This difference may explain why the 1998 layers were more strongly influenced by wind than the 1996 layers.

The 1996 and 1998 results cannot be directly compared for temporal trends in thin layer occurrence, due to the different time frames of experimentation. In 1996, temporal patterns in phytoplankton layers were assessed over a period of three months. By contrast, the 1998 data spanned a time frame of just two weeks. Consequently a temporal comparison of the two studies would necessarily be grounded in two unequal frames of reference, which by extension might lead to inaccurate conclusions.

CONCLUSIONS

The results presented in this paper support previous findings that thin phytoplankton layers exist as recurring phenomena. Thin layers were observed in East Sound in both 1996 and 1998, suggesting their importance as critical biological features in the water column. For both years, these phytoplankton layers averaged just over 1 m in thickness. Only high resolution, fine-scale profiling is capable of detecting these thin structures in the water column.

Differences in the 1996 and 1998 profiles emphasize the variability in thin layer development. Layers in 1998 were generally less in number and lower in intensity than those observed in 1996. This result may largely be explained by the different density structures observed in the two years. Density gradients were considerably greater in 1996 than in 1998. Previous data have shown that thin layer distributions are closely associated with the depth and strength of the pycnocline (Dekshenieks et al. submitted b). The development of layers is thought to rely on a number of physical processes (e.g. density gradient, shear, buoyancy frequency). Accordingly, layer attributes might understandably be drastically variable depending on the unique physical conditions of a given time period. For this reason, it was critical to redefine the criteria for identifying layers for the 1998 experiment. The 1996 criterion, that a layer must have an optical peak three times the size of its background intensity, was developed for a time when the water column had a very different physical structure.

East Sound is similar to other coastal systems in that physical conditions are known to vary greatly. Given that thin layers occur across a range of physical conditions in East Sound, they are expected to exist in other coastal systems as well. This idea is supported both by theoretical models (Donaghay and Osborn 1997) and by observations of thin layers in several different coastal systems (Ryther 1955, Bjornsen and Neilsen 1991, Carpenter et al. 1995). The 1998 results from East Sound indicate some of the physical conditions in which layers can be expected to occur. Most layers occurred in regions of the water column with high buoyancy frequencies and moderate to high current shears. Very few layers were found in unstable regions (i.e., where Richardson number exceeded 0.25). Additionally, thin phytoplankton layers did not develop at the highest observed wind speeds. Persistent layers are therefore not expected in wind-mixed regions.

Analysis of the 1998 data has produced a comprehensive set of relationships between physical structure and the temporal occurrence of thin phytoplankton layers in the water column. Identifying these relationships is a first step toward investigating the mechanisms behind thin layer dynamics.

ACKNOWLEDGEMENTS

Special thanks to Jan Rines, Malcolm McFarland and Rob Pockalny for their assistance with this research. The research was supported by the Summer Undergraduate Research Fellowship in Oceanography at the University of Rhode Island; Office of Naval Research Physical Oceanography grants # N00014-98-1-0388 and #N00014-99-1-0293 to M.M. Dekshenieks, P.L. Donaghay, T.R. Osborn and A.E. Gargett; and Office of Naval Research Biological Oceanography grant #N00014-95-1-0225 to P.L. Donaghay.

LITERATURE CITED

Bjornsen PK, Nielsen TG (1991). Decimeter scale heterogeneity in plankton during a pycnocline bloom of *Gyrodinium aureolum*. Mar Ecol Prog Ser 73:263-267.

Carpenter EJ, Janson S, Boje R, Pollehne F, Chang J (1995). The dinoflagellate *Dinophysis norvegica*: biological and ecological observations in the Baltic Sea. Eur J Phycol 30:1-9.

Dekshenieks MM, Osborn TR, Donaghay PL, Sullivan JM (submitted a). Observations of general circulation patterns in East Sound, Washington. Estuarine, Coastal and Shelf Science.

Dekshenieks MM, Donaghay PL, Sullivan JM, Rines JEB, Osborn TR, Twardowski MS (submitted b). Temporal and Spatial Occurrence of Thin Phytoplankton Layers in Relation to Physical Processes. Marine Ecology Progress Series.

Donaghay PL, Osborn TR (1997). Toward a theory of biological-physical control of harmful algal bloom dynamics and impacts. Limnol Oceanogr 42(5):1283-1296.

Mann KH, Lazier JRN (1991). Dynamics of marine ecosystems. Blackwell, Oxford.

Osborn TR (1998). Finestructure, microstructure, and thin layers. Oceanography 11(1):36-43.

Ryther JH (1955). Ecology of autotrophic marine dinoflagellates with reference to red water conditions. In: Johnson FH (ed) The luminescence of biological systems. AAAS, p 387-413.

LIST OF FIGURES.

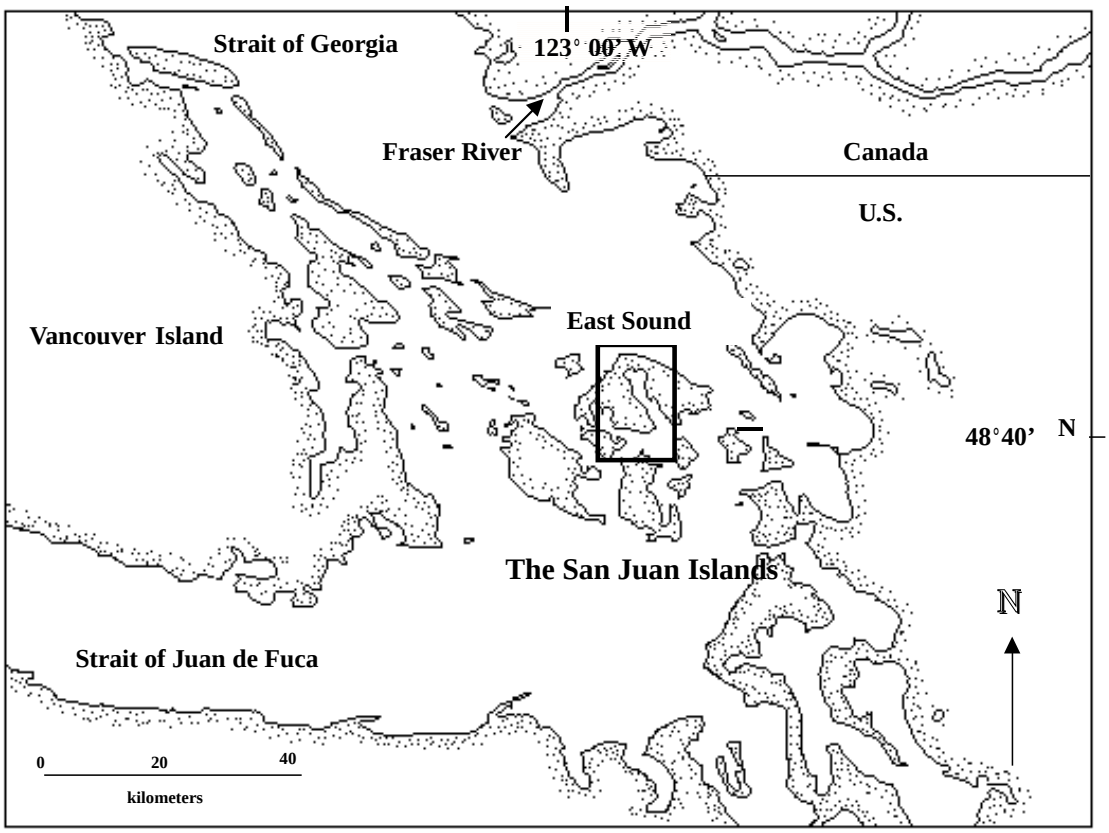

Figure 1: Map of East Sound, on Orcas Island, WA. Also shown are the Strait of Juan de Fuca, the Strait of Georgia and the Fraser River.

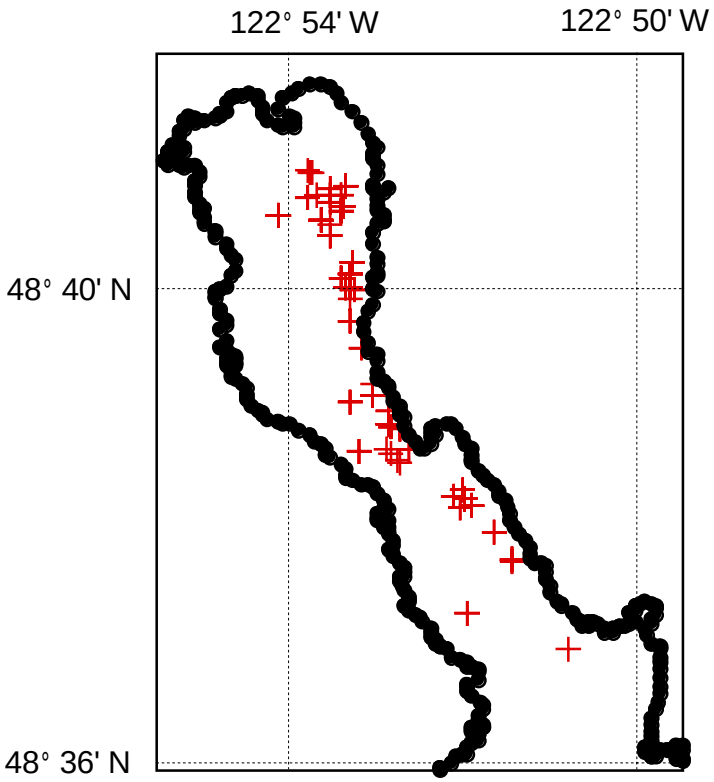

Figure 2: Map of East Sound, with sampling stations shown in red.

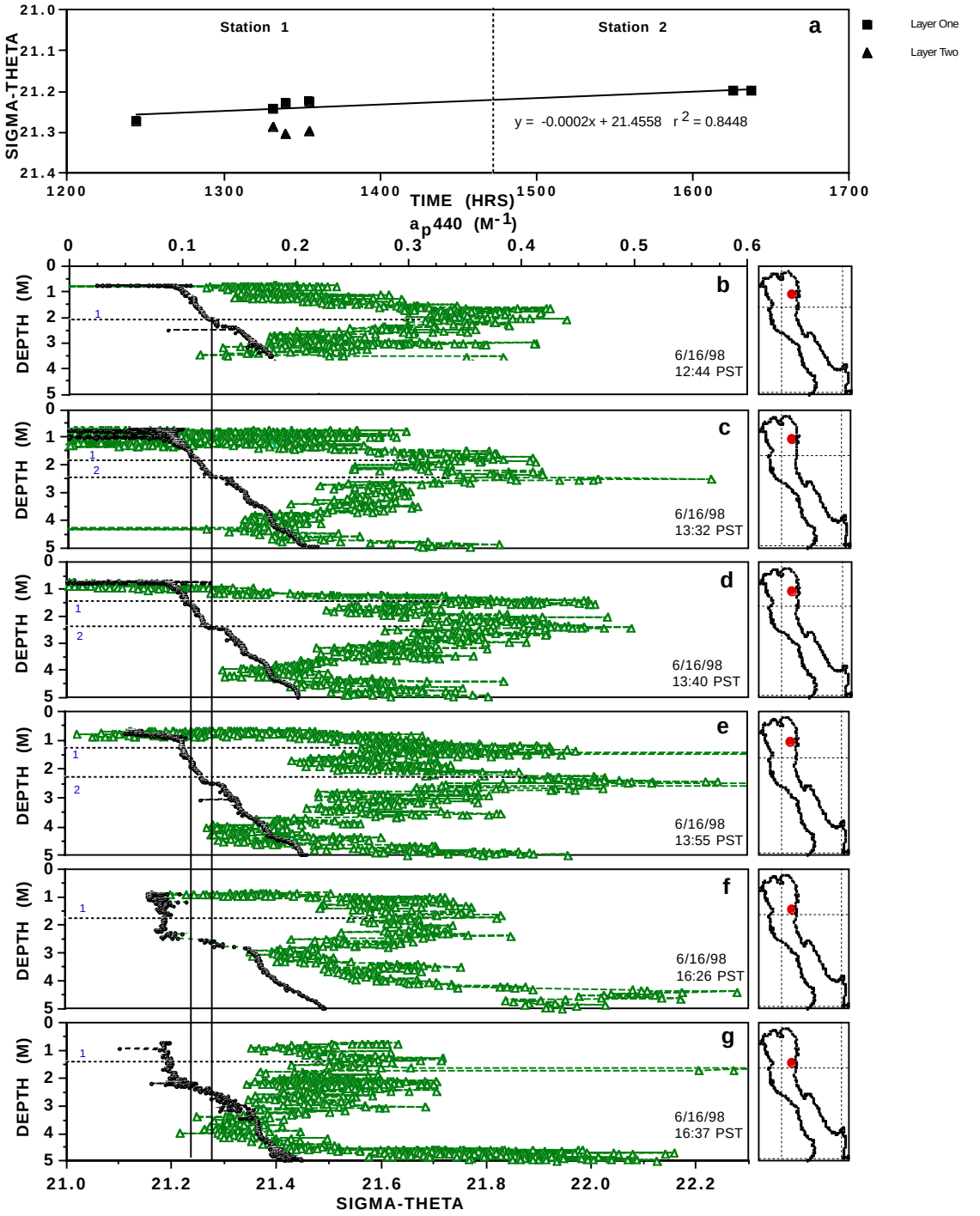

Figure 3: Sample analysis of layer coherence over time, using data obtained from two stations on June 16, 1998. Graph (a) shows the correlation between density values for a stable layer over six casts. Graphs (b) through (g) depict density structure (black circles) and layer occurrence (gray triangles) vs. depth for each individual cast. Horizontal, dashed lines indicate layers. The vertical solid lines illustrate density correlations through each layer occurrence.

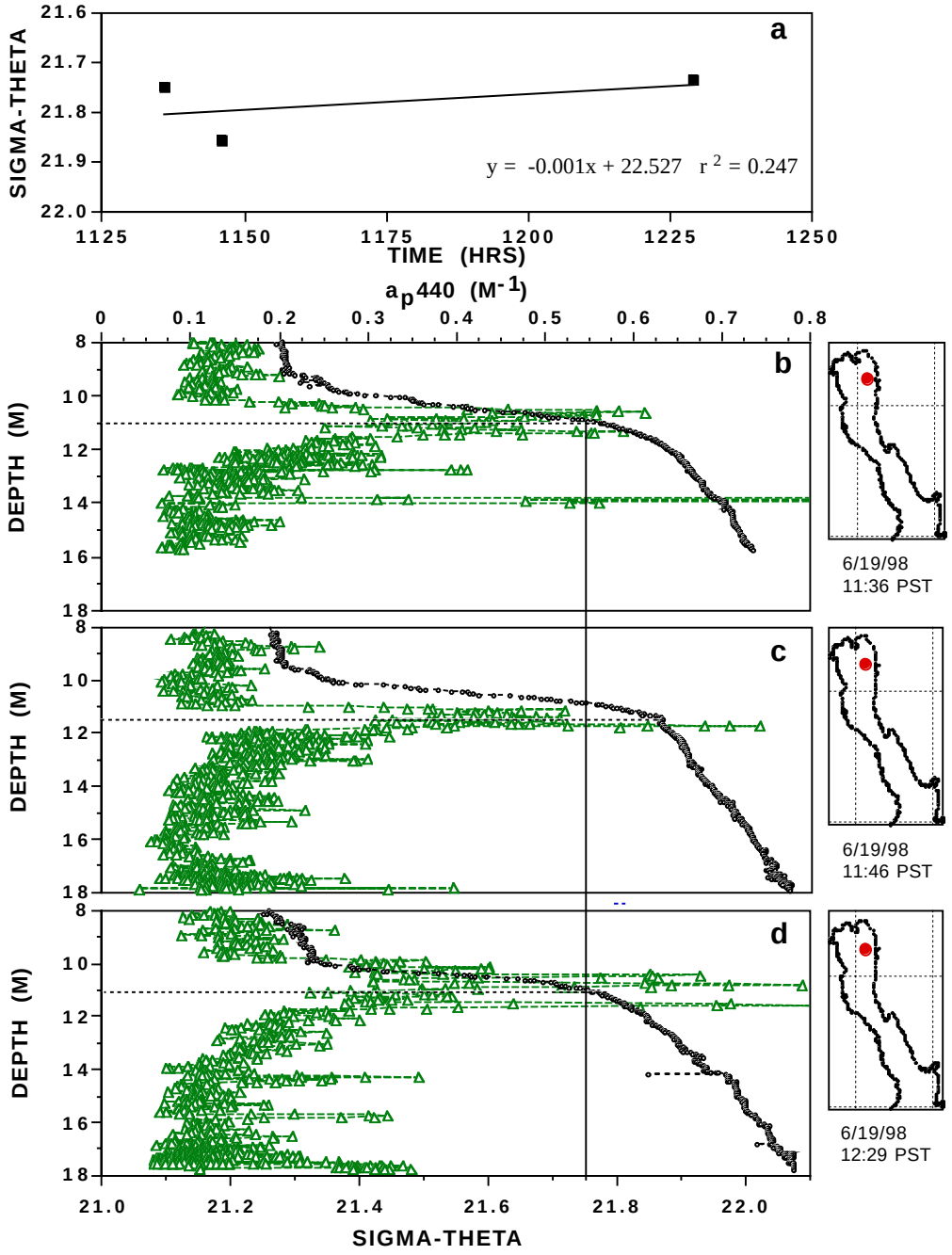

Figure 4: Sample criteria for layer coherence over time, using data obtained from a single station on June 19, 1998. Graph (a) shows the correlation between density values for a stable layer over three casts. Graphs (b) through (d) depict density structure (black circles) and layer occurrence (gray triangles) for each individual cast. Horizontal, dashed lines superimposed onto the plots indicate layers. The vertical solid line, extending between graphs, illustrates density correlation through each occurrence of the layer.

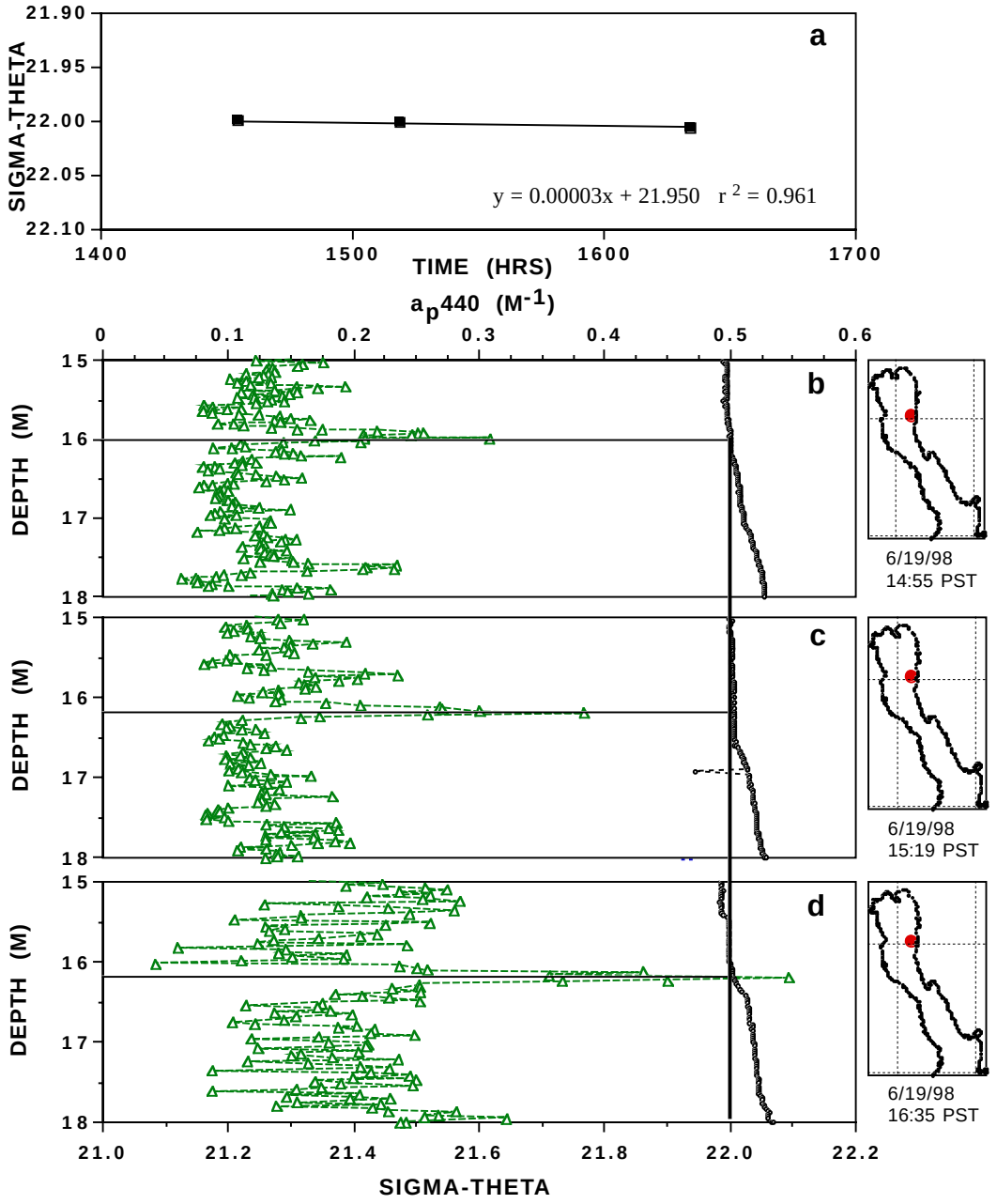

Figure 5: Sample criteria for layer coherence over time, using data obtained from a single station on June 19, 1998. Graph (a) shows the correlation between density values for a stable layer over three casts. Graphs (b) through (d) depict density structure (black circles) and layer occurrence (gray triangles) for each individual cast. Horizontal lines superimposed onto the graphs indicate layers. The vertical solid line, extending between graphs, illustrates density correlation through each occurrence of the layer.

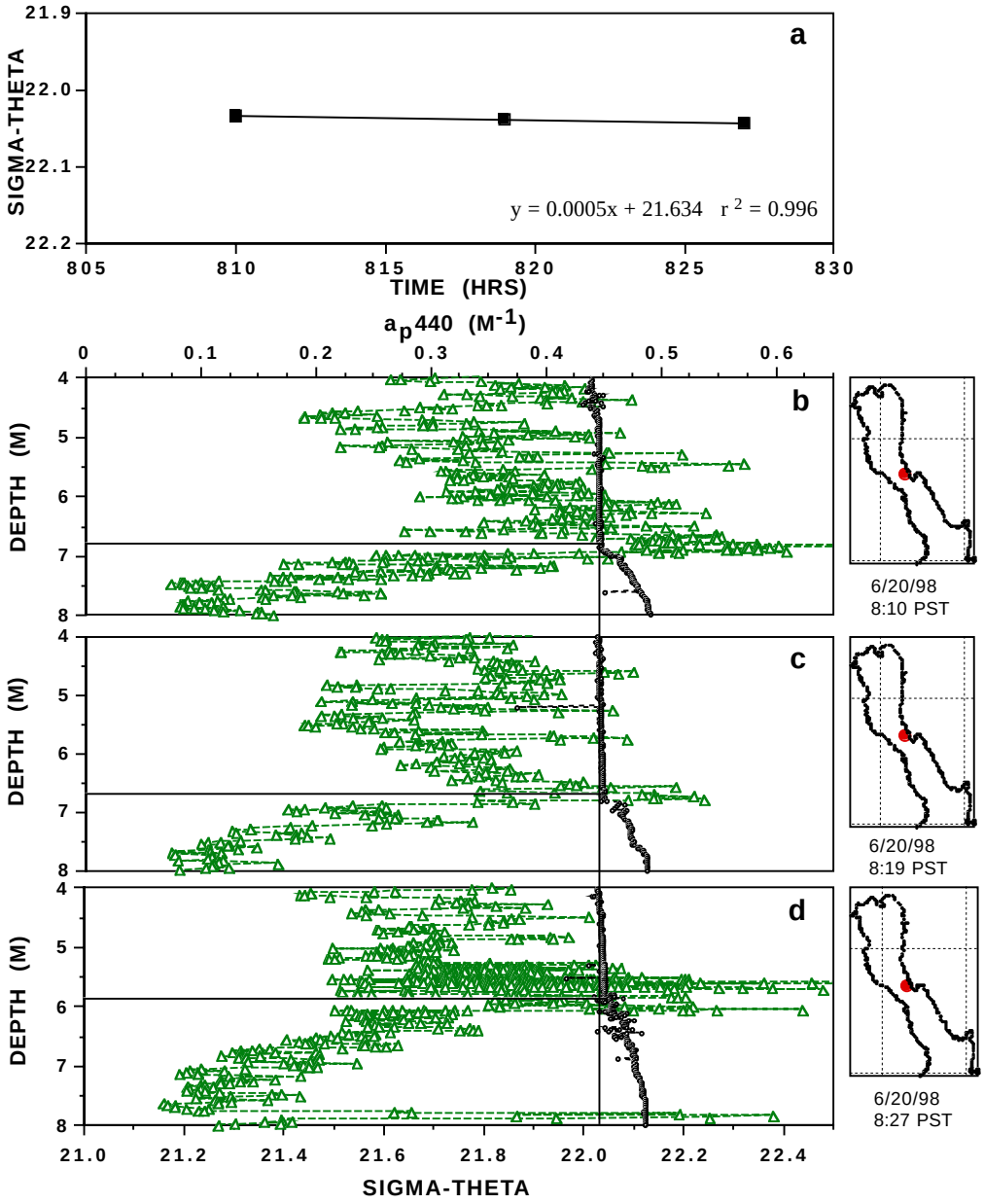

Figure 6: Sample criteria for layer coherence over time, using data obtained from a single station on June 20, 1998. Graph (a) shows the correlation between density values for a stable layer over three casts. Graphs (b) through (d) depict density structure (black circles) and layer occurrence (gray triangles) for individual casts. Horizontal lines superimposed onto the graphs indicate layers. The vertical solid line, extending between graphs, illustrates density correlation through each occurrence of the layer.

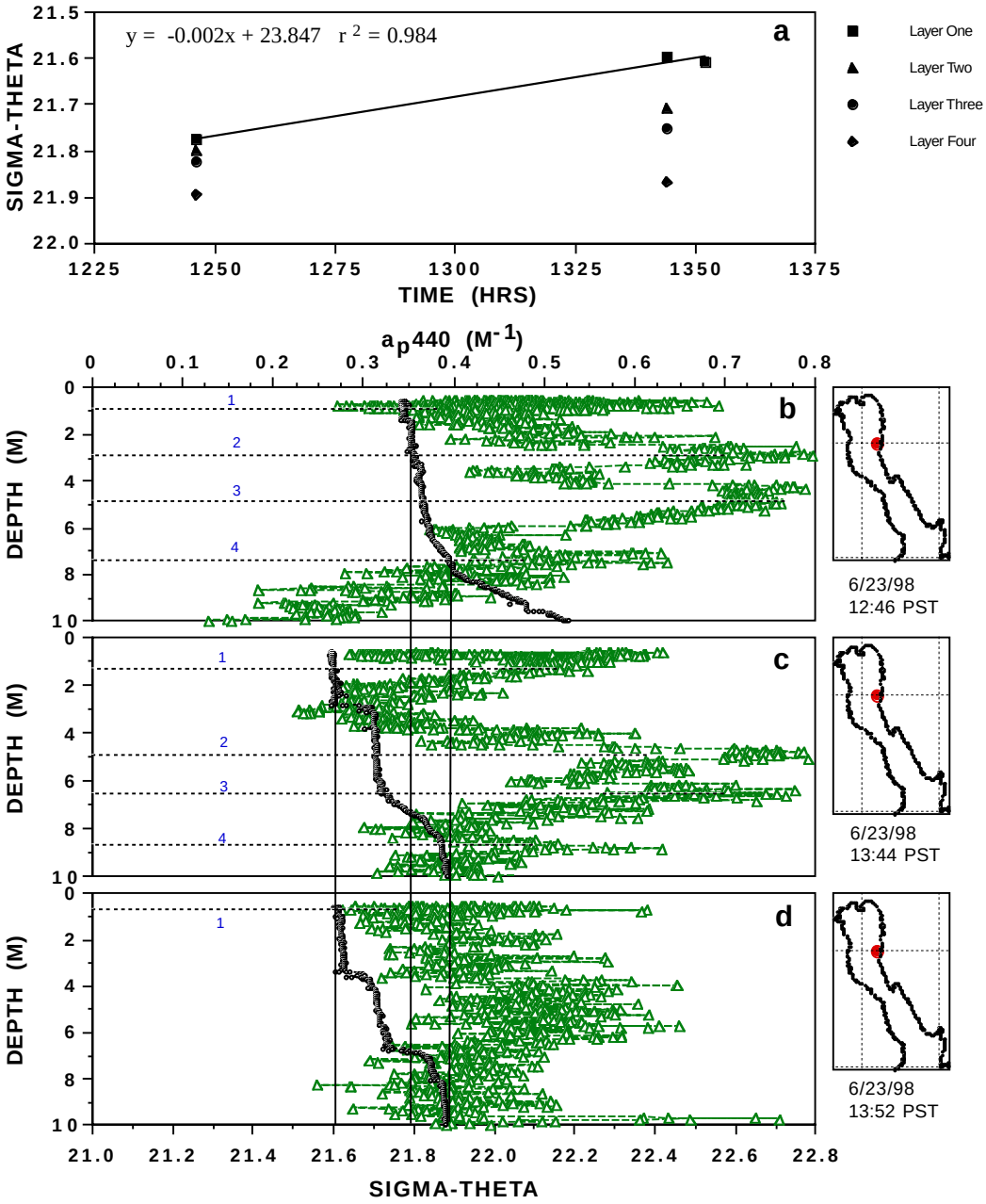

Figure 7: Sample analysis for layer coherence over time, using data obtained from a single station on June 23, 1998. Graph (a) shows the correlation between density values for four layers observed over three casts. Graphs (b) through (d) depict density structure (black circles) and layer occurrence (gray triangles) vs. depth for each cast individually. Horizontal, dashed lines superimposed onto the graphs indicate layers. The vertical solid lines, extending between graphs, illustrate density correlations through each occurrence of the layers.

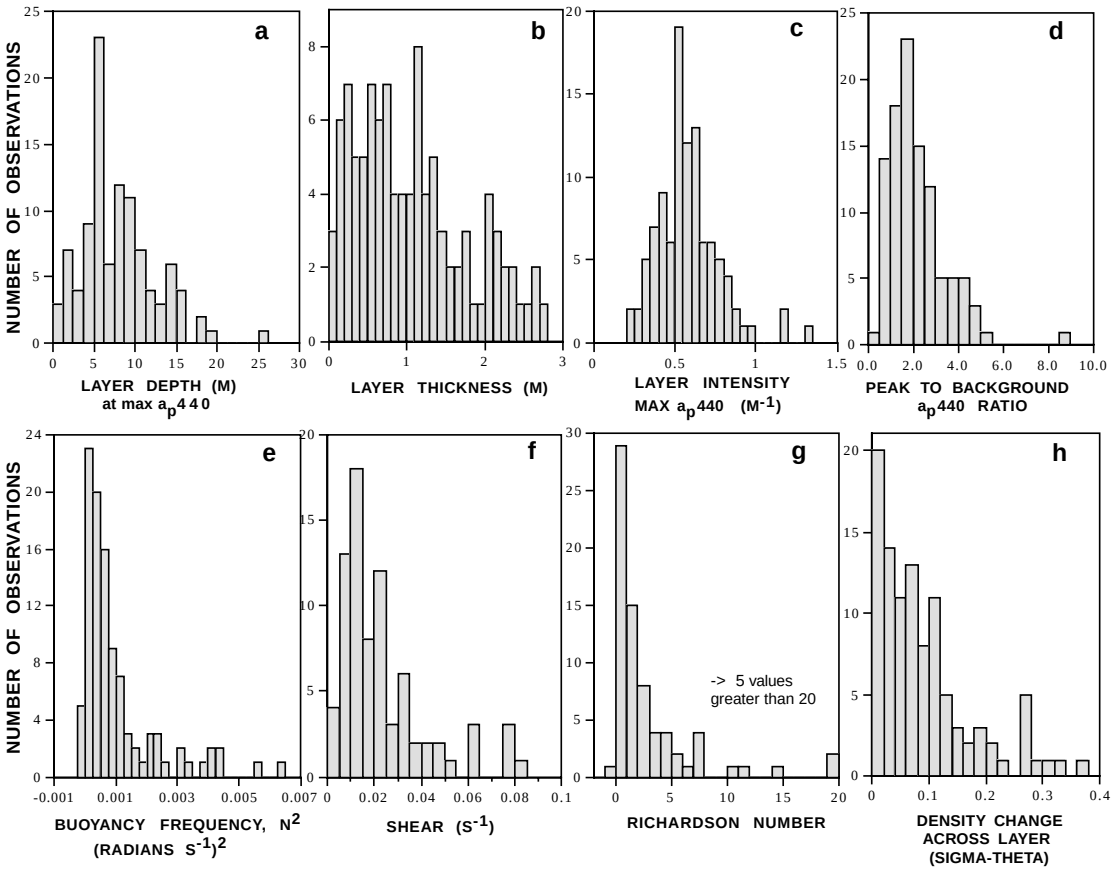

Figure 8: Histograms of layer attributes and physical attributes associated with thin layers.

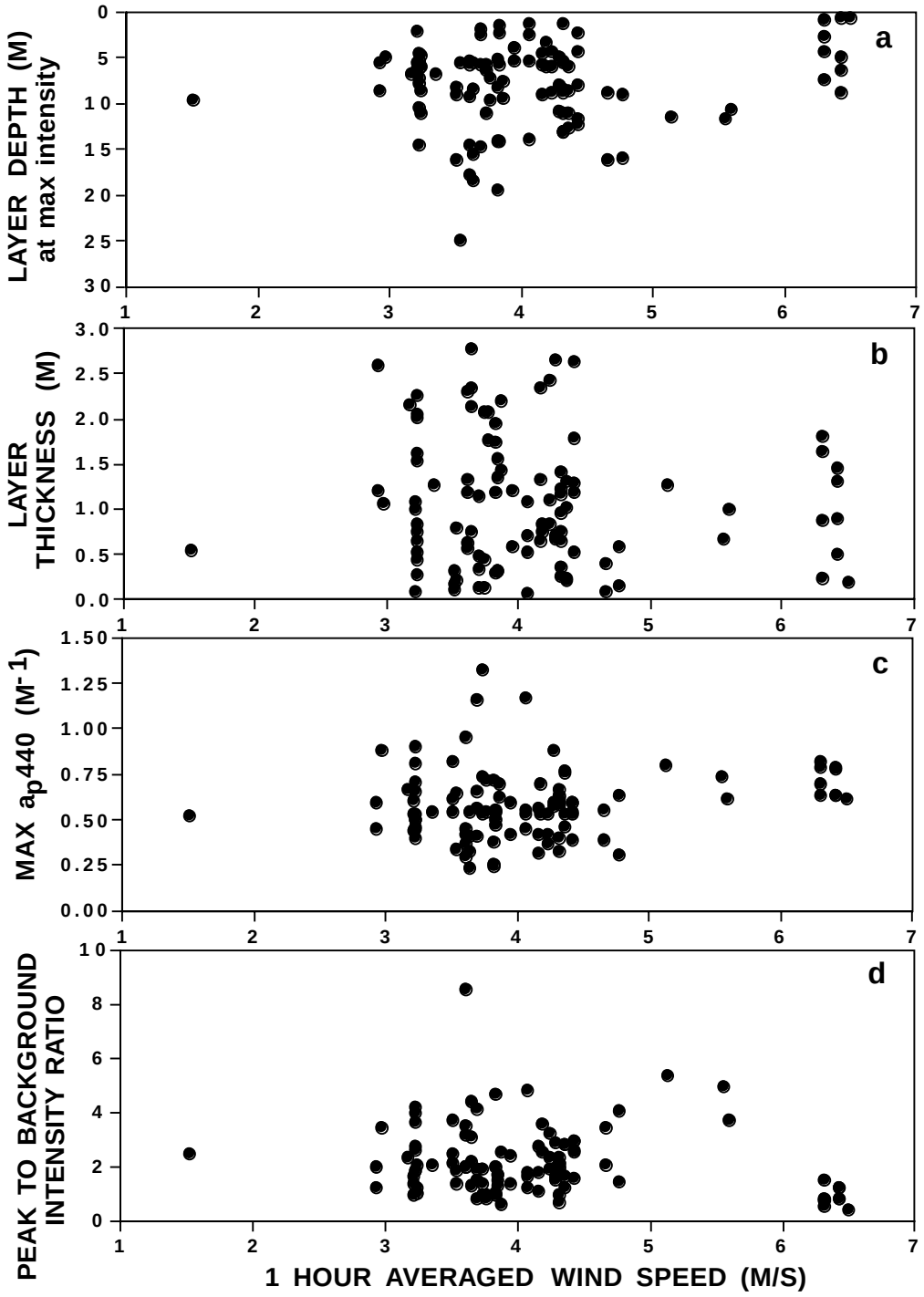

Figure 9: Thin layer attributes as a function of wind speed.

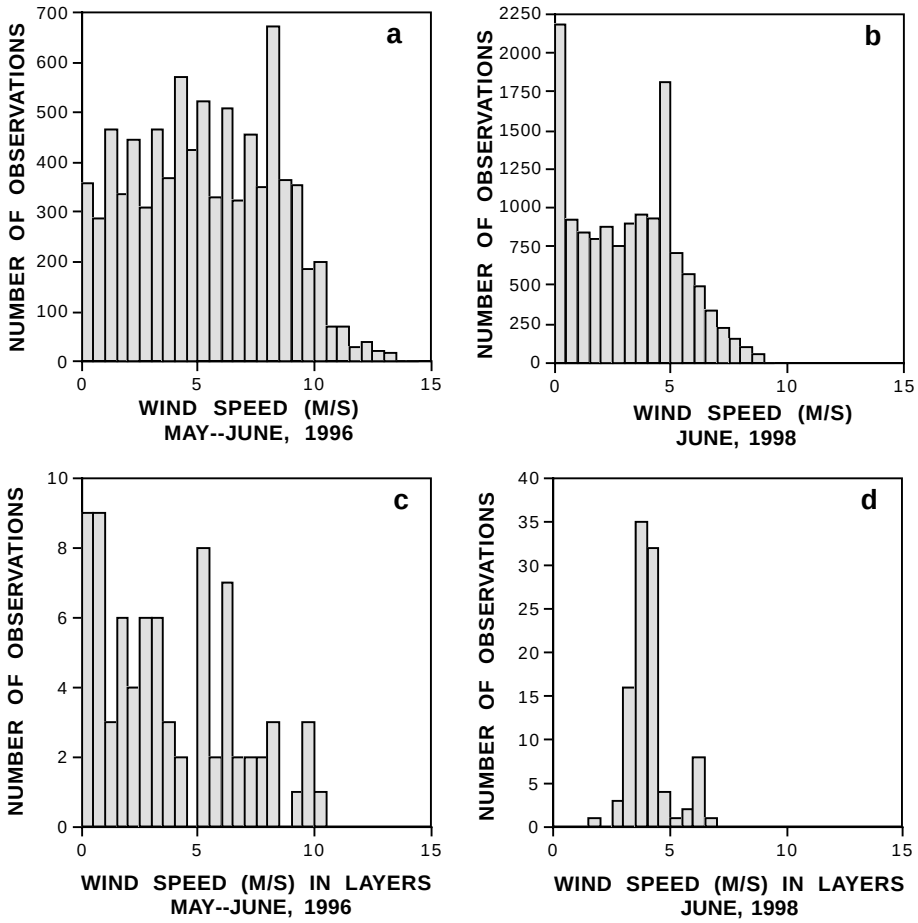

Figure 10: Comparative histograms of wind speed for 1996 and 1998 cruises in East Sound. Graphs (a) and (b) show all wind speeds observed in 1996 and 1998, respectively. Graphs (c) and (d) show wind speeds associated with thin layer occurrence during 1996 and 1998, respectively.

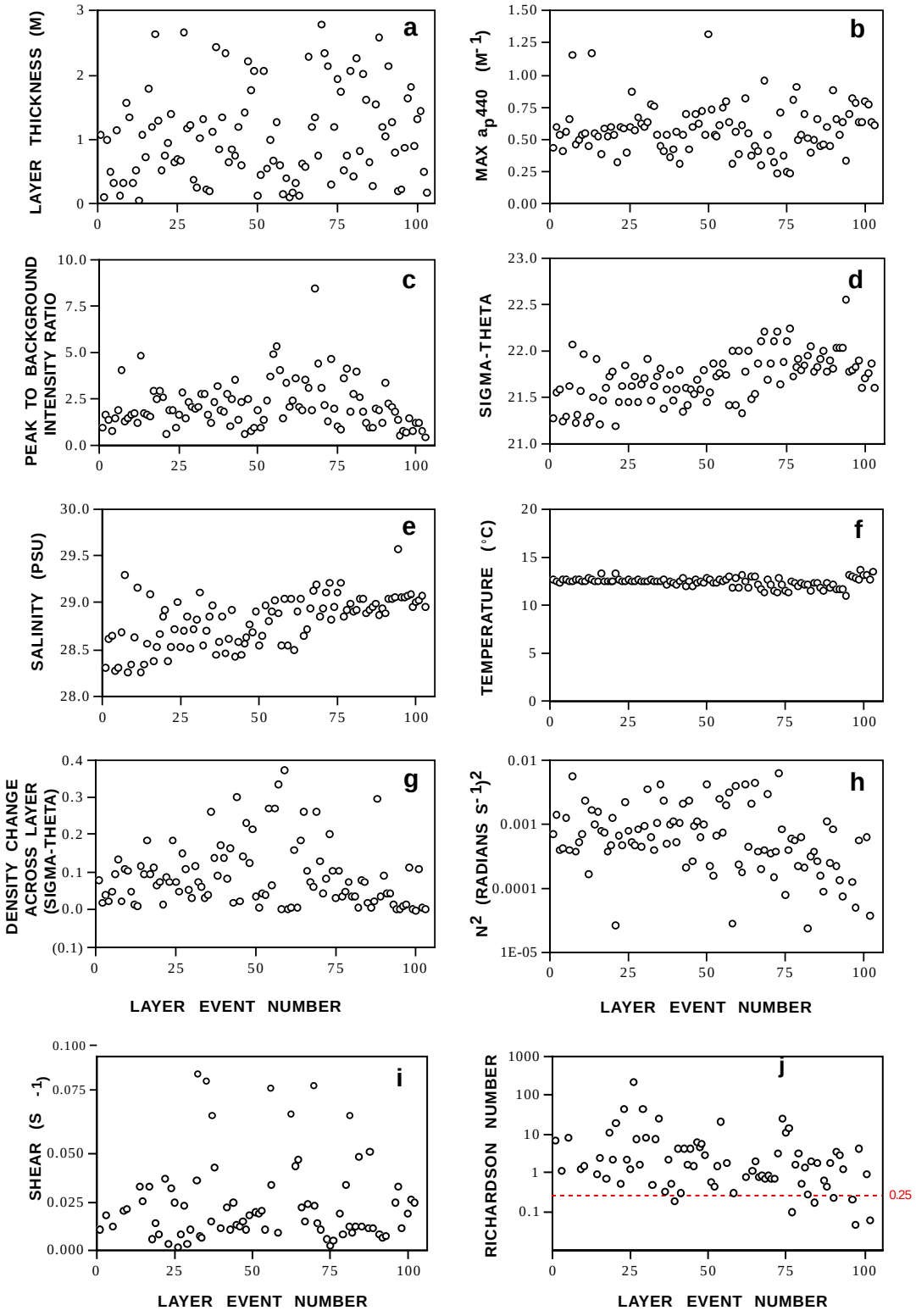

Figure 11: Thin layer attributes and physical attributes associated with thin layers, plotted sequentially in the order in which they were encountered.